

Doctoral Thesis



Université de Limoges

Sciences et Ingénierie des Matériaux, Mécanique, Energétique (SIMME)
IRCER - Institute of research for ceramics UMR CNRS 7315

Thesis to obtain the degree of
Docteur de l'Université de Limoges
IRCER, Axe 3 - organisation structurale multiéchelle des matériaux

Presented and supported by

Ravikant KUMAR

Le 22 May 2024

AB-INITIO STUDY OF THE STRUCTURAL AND ELECTRONIC PROPERTIES OF ZIRCONIA AND TIN(IV) OXIDE NANOPARTICLES

Thesis supervised by Olivier MASSON, Assil BOUZID, and Abid BERGHOUT

Jury :

Rapporteurs :

Xavier ROCQUEFELTE

Professeur des Universités, ISCR - Universités de Rennes 1

Patrick ROZIER

Maître de conférences (HDR), CIRIMAT - Université de Toulouse III Paul Sabatier

Examineurs :

Gianguido BALDINOZZI

Directeur de recherche, SPMS - Université Paris-Saclay, CentraleSupélec

Olivier MASSON

Professeur des Universités, IRCER - Université de Limoges

Assil BOUZID

Chargé de recherche CNRS, IRCER, Université de Limoges

Abid BERGHOUT

Maître de conférences, IRCER - Université de Limoges



Dédicace [à compléter]

If I have seen further, it is by standing on the shoulders of Giants.

Sir Isaac Newton

Remerciements

I would like to express my deepest gratitude to my supervisor, Olivier MASSON and Abid BERGHOUT for their unwavering support, guidance, and invaluable mentorship throughout the entire journey of this research. A special thanks to Assil BOUZID for their exceptional mentoring, assistance and contribution, which went above and beyond expectations. Their commitment to excellence and collaborative spirit have left an indelible mark on this work. Their expertise, encouragement, and constructive feedback have been instrumental in shaping this work.

I extend my sincere appreciation to the members of my thesis committee for their insightful comments, suggestions, and time dedicated to reviewing and enhancing this thesis.

I am thankful to Institut de Recherche sur les Céramiques IRCER for providing the necessary resources, facilities, and a conducive environment for conducting this research. I am very thankful to GENCI-CINES for providing their High-Performance Computing resources (HPC) Jean Zay (Grant A0120913448) for running all the simulation jobs. The collaborative and intellectually stimulating atmosphere has greatly enriched my academic experience.

Special thanks go to my colleagues and peers for their camaraderie, intellectual discussions, and shared experiences. Their support has been a source of motivation and inspiration.

I am grateful to my family for their unwavering encouragement, understanding, and patience during the demanding phases of this academic pursuit. Their support has been my pillar of strength.

Lastly, I express my gratitude to all those who have contributed in various ways, directly or indirectly, to the completion of this thesis. Your support has been invaluable, and I am truly appreciative.

Contents

0	General introduction	17
1	Literature review	21
1.1	Nanomaterials and metal oxide nanoparticles	22
1.2	Structure of the fluorite-derived zirconia polymorphs	28
1.2.1	Cubic phase of zirconia	29
1.2.2	Tetragonal phase of zirconia	30
1.2.3	Monoclinic phase of zirconia	30
1.2.4	Orthorhombic I phase of zirconia	31
1.3	Structure of cassiterite tin dioxide	31
1.4	Structure of "ultrasmall" nanoparticles	33
1.5	Surface passivation of NP models	39
1.6	The relation between band gap and nanoparticle size	46
1.7	Conclusions	50
2	Atomic scale modelling	52
2.1	A quick overview of density functional theory	54
2.1.1	Many body problem	54
2.1.2	Born-Oppenheimer approximation	56
2.1.3	Density Functional Theory	57
2.1.4	Hohenberg-Kohn theorem	57
2.1.5	Kohn-Sham formalism	58
2.1.6	Exchange-Correlation Functionals	61
2.1.6.1	Local Density Approximation	62
2.1.6.2	Generalized Gradient Approximation	62
2.1.6.3	Hybrid Functional	63
2.1.7	Electronic wave functions basis-set	63
2.1.8	Pseudopotential approximation	64
2.2	Ab-initio Molecular Dynamics	66

2.2.1	Born-Oppenheimer molecular dynamics	66
2.2.2	Temperature control	66
2.2.2.1	Temperature in the NVE ensemble	66
2.2.2.2	Temperature in the NVT ensemble	67
2.3	Ab-initio principles for calculating electronic properties	69
2.3.1	Total and projected Density of states	69
2.4	CP2K code	71
3	Structure of ZrO₂ Nanoparticle Models	73
3.1	Computational Details	74
3.2	Experimental Data	75
3.3	NP Model Generations	77
3.3.1	Methodology	77
3.3.2	Assessment of the nanocluster models	81
3.4	Results and Discussions	84
3.4.1	Structure Evolution as a Function of the NP Size	84
3.4.1.1	The overall structure of the NP models	84
3.4.1.2	Disentangling Core and Surface Contributions	85
3.4.1.3	Structural Properties of the Core and Surface Atoms	87
3.5	Conclusions	90
4	Structure of SnO₂ Nanoparticle Models	92
4.1	Computational details	93
4.2	Generation of SnO ₂ nanocluster models	93
4.2.1	Methodology	93
4.2.2	Assessment of the nanocluster models	96
4.3	Results and Discussions	98
4.3.1	Partial PDFs as a function of size of the NPs	98
4.3.2	Disentangle the core and surface of nanoclusters	100
4.3.3	Structural properties of the core and surface atoms	101
4.3.4	Comparison of local environments of core and surface atoms for ZrO ₂ and SnO ₂ nanoclusters	106
4.4	Conclusions	107
5	Electronic properties of ZrO₂ and SnO₂ NPs with their comparison	109
5.1	Electronic properties of ZrO ₂ systems	110
5.1.1	Density of states of bulk ZrO ₂	110

5.1.2	DOS of whole nanoparticle models	112
5.1.3	Core and Surface atoms contribution to the total DOS	118
5.2	Electronic properties of SnO ₂ nanoparticles	122
5.2.1	Density of states of bulk SnO ₂	122
5.2.2	DOS evolution as a function of size of the nanoclusters	125
5.2.3	Core and surface atoms contribution to the total DOS	127
5.3	Comparison of electronic properties between ZrO ₂ and SnO ₂ NPs	130
5.4	Conclusions	131
6	General conclusions	133
7	Bibliography	139
	References	140
	List of Works	150

Table of Figures

1.1	Lycurgus Cup. (a) It appears green when viewed in reflected light, such as during the day, and (b) appears red when light is shone into the cup and transmitted through the glass. Taken from Ref. [15].	22
1.2	Evolution of the number of articles and annual growth rate in nanotechnology since 2000–2019. Taken from Ref. [20].	23
1.3	Various applications of nanoparticles in nanotechnology. Taken from Ref. [21].	24
1.4	General scale of nano-materials. Taken from Ref. [22].	24
1.5	Possible dimensions of the nanoparticles. Taken from Ref. [23].	25
1.6	Schematic diagram of the bandgap variation in nanoparticles. Taken from Ref. [29].	26
1.7	Fluorescence of CdSe-CdS nanoparticles with diameters varying from 1.7 nm (blue) up to 6 nm (red). Reproduction by H. Weller, University of Hamburg. Taken from Ref. [34].	26
1.8	Unit cells of the four fluorite-derived zirconia polymorphs: (a) cubic, (b) tetragonal, (c) monoclinic, and (d) orthorhombic-I. The unconventional cell is used for the tetragonal polymorph in order to highlight its link with the fluorite parent phase.	28
1.9	Calculated (a) total and (b) partial PDFs of cubic phase zirconia.	29
1.10	Calculated (a) total and (b) partial PDFs of tetragonal phase zirconia.	30
1.11	Calculated (a) total and (b) partial PDFs of monoclinic phase zirconia.	31
1.12	Calculated (a) total and (b) partial PDFs of orthorhombic I phase zirconia.	32
1.13	(a) Structural representation, calculated (b) total and (c) partial PDF of tetragonal SnO ₂ rutile	33
1.14	TEM pictures of the monoclinic zirconia nanocrystals (a, c) together with the calculated Wulff shapes (a1, c1), oriented along [-111], [011], and [001] directions to align with the observed 2D images. Taken from Ref. [72].	34

1.15	Molecular dynamics simulation prediction of the structure (cross section) of an ~ 5 nm anatase particle in vacuum. The surface layer (A) and the near-surface layer (B) are highly distorted, but the interior of the nanoparticle (C) retains typical anatase bulk structure. Region C disappears as particle diameter decreases toward ~ 2 nm. Taken from Ref. [74].	35
1.16	Structure of a ~ 2 nm TiO_2 nanoparticle obtained from reverse Monte Carlo simulation using both experimental PDF data and EXAFS spectra. Taken from Ref [76].	36
1.17	Fit of the experimental PDF of ZrO_2 nanocrystals obtained by intensive grinding of micrometric monoclinic zirconia powder, from Ref. [77].	36
1.18	Experimental PDF of the zirconia particles produced at 210°C for 3 days in benzyl alcohol with 0.2 mol.L^{-1} NaOH with the (a) cubic model, (b) tetragonal model, (c) monoclinic model, and (d) orthorhombic I model of zirconia. Taken from Ref. [23].	37
1.19	(a) TEM micrographs of the zirconia particles synthesized at 210°C for 3 days in benzyl alcohol and (b) size dispersion analysis with 70 data points for the benzyl alcohol sample. Taken from Ref. [23].	37
1.20	(a) Experimental PDF of the zirconia particles produced at 210°C for three days in anisole with 0.2 mol.L^{-1} NaOH compared with the unrefined (a) cubic model, (b) tetragonal model, (c) monoclinic model, and (d) orthorhombic I model of zirconia. Taken from Ref. [23].	38
1.21	(a) TEM micrographs of the zirconia particles synthesized at 210°C for 3 days in anisole and (b) size dispersion analysis with 49 data points for the anisole sample. Taken from Ref. [23].	39
1.22	Surface oxygen atoms forming a (a) dimer and (b) trimer bonded together with Sn atoms. Taken from Ref. [79].	41
1.23	(a) PDOS of tin atoms and (b) PDOS of oxygen atoms. Taken from Ref. [79].	41
1.24	Models of partly truncated octahedral zirconia nanoparticles $(\text{ZrO}_2)_n$ created by removing (a) three Zr corner atoms from the $\text{Zr}_{19}\text{O}_{32}$ nanoparticle, (b) four Zr corner atoms from $\text{Zr}_{44}\text{O}_{80}$, and (c) five Zr corner atoms from $\text{Zr}_{85}\text{O}_{160}$. Zr is represented by big blue atoms and O by red small atoms. Taken from Ref. [80].	41
1.25	The Projected Density of States for nanoparticles $\text{Zr}_{16}\text{O}_{32}$, $\text{Zr}_{40}\text{O}_{80}$, and $\text{Zr}_{80}\text{O}_{160}$ are presented in (a), (b), and (c) respectively. These are obtained from PBE, PBE+U, and PBE0 calculations, arranged from top to bottom. The energy reference point corresponds to the Fermi level. Taken from Ref. [80].	42

1.26	The schematic plots of (a) an octahedral Sn ($^{4/3}\text{H}$) ₆ structure, and (b) a regular triangular O ($^{2/3}\text{H}$) ₃ structure. The yellow, red, and white balls represent Sn, O, and pseudohydrogen atoms, respectively. Taken from Ref. [82].	43
1.27	Initial cubic configuration and four configurations that are local minima of energy, for the Zr ₄₃ O ₈₆ cluster without surface impurities, found with CP heating/cooling cycles. Below each cluster, the energy loss with respect to the initial configuration is shown. Taken from Ref. [83].	44
1.28	Comparing the experimental result with the PDFs computed from the four local energy minima observed for the unpassivated cluster: direct minimization from the starting perfect cubic crystal structure (a), and heating cooling cycles up to 500 K (b), 1000 K (c), and 1500 K (d). Taken from Ref. [83].	44
1.29	Initial and optimized configurations for clusters with dissociated H ₂ O impurities on the surface. Taken from Ref. [83].	45
1.30	PDFs obtained from the optimized configurations with H ₂ O surface impurities: coverage with 4 (a), 8 (b), 12 (c), 16 (d), 20 (e), and 24 (f) water molecules. Taken from Ref. [83].	46
1.31	Comparison of the band gap variation in ZnO nanocrystals derived from the Tight-Binding (TB) approximation and its comparison with experimentally obtained data from various references. The dashed line represents the values obtained from the Effective Mass Approximation (EMA). The inset illustrates the fit to the calculated values. Taken from Ref. [84].	48
1.32	Band gap against ZnO particle sizes together with (a) expressions from the literature and, together with (b) the best fit using effective mass approximation. Taken from Ref. [87].	49
1.33	The calculated band gaps of different size SnO ₂ QWs and QDs. The solid lines are the fitted curves. Taken from Ref. [82].	49
2.1	Schematic diagram for many-body interaction between electrons and nucleus.	55
2.2	Flowchart representation of solving the Kohn-Sham equations.	61
2.3	Schematic depiction of the pseudopotential (solid lines) and all-electron potential (dashed lines), together with the corresponding wave-functions. The radius value at which both potentials exhibit identical behavior is shown by the vertical line r_c . Taken from Ref. [110].	65
3.1	Energy convergence test of the cubic polymorph as a function of energy cutoff values.	75

3.2	Experimental pair distribution function where black and red color shows Exp1 and Exp2 PDFs. Data taken from Ref. [23], [83]	76
3.3	Initial NP models with water molecules (a) $[\text{ZrO}_2]_{14}$, (b) $[\text{ZrO}_2]_{16}$, (c) $[\text{ZrO}_2]_{43}$, (d) $[\text{ZrO}_2]_{80}$, and (e) $[\text{ZrO}_2]_{141}$	78
3.4	Temperature evolution during MD simulation corresponding to three different thermal treatments: TT1 (red), TT2 (blue) and TT3 (black).	79
3.5	(a) Initial structure of $[\text{ZrO}_2]_{43}$ nanocluster covered with 24 water molecules and (b) the final structure obtained after MD thermal treatment TT3. Zirconium, oxygen and hydrogen atoms are in silver, red and white, respectively. Blue dotted line shows the hydrogen bonds.	79
3.6	Number of chemisorbed and physisorbed water at the surface of $[\text{ZrO}_2]_{43}$ nanocluster during MD thermal treatments (a) TT1, (b) TT2 and (c) TT3.	80
3.7	Evolution of the rate of chemisorbed water as a function of (a) temperature during thermal treatment TT3 applied and (b) size after quenching at $T = 300$ K to various $[\text{ZrO}_2]_n$ models. The error bars represent the fluctuation of chemisorbed water molecules.	81
3.8	PDFs computed from the resulting structure of $[\text{ZrO}_2]_{43}$ nanocluster after thermal treatments, compared to the experimental (a) Exp1 PDF, and (b) Exp2 PDF.	82
3.9	The PDFs computed from the resulting structure after thermal treatment TT3 are analyzed in relation to the amount of surface coverage. A comparison is drawn between the experimental PDFs, labeled as (a) Exp1 and (b) Exp2, for the $[\text{ZrO}_2]_{43}$ nanocluster. Likewise, the experimental PDFs (c) Exp1 and (d) Exp2 are compared for the $[\text{ZrO}_2]_{141}$ nanocluster.	83
3.10	The computed partial PDFs related to (a) Zr-O, (b) O-O, and (c) Zr-Zr distances for the ZrO_2 nanocluster models.	85
3.11	Evolution of Zr-O bond length as a function of the position of the atoms in the NP for various size of ZrO_2 models.	86
3.12	Histogram of (a) Zr-O, (b) O-O and (c) Zr-Zr distances found in nanocluster models with various sizes, compared with the calculated partial PDFs from the cubic and monoclinic polymorphs of zirconia (upper curves)	87
3.13	Fraction of the coordination number of Zr-atoms within the core and the surface of (a) $[\text{ZrO}_2]_{43}$, (b) $[\text{ZrO}_2]_{80}$ and (c) $[\text{ZrO}_2]_{141}$, nanoclusters.	89
4.1	Initial structure with water molecules of modelled NPs (a) $[\text{SnO}_2]_{15}$, (b) $[\text{SnO}_2]_{23}$, (c) $[\text{SnO}_2]_{31}$, (d) $[\text{SnO}_2]_{48}$, (e) $[\text{SnO}_2]_{69}$, and (f) $[\text{SnO}_2]_{103}$	94
4.2	Temperature evolution during MD simulation of thermal treatment TT3.	95

4.3	Representative snapshots on NP with O dimers and trimers at the surface.	95
4.4	The calculated partial PDF of O-O distances as a function of NPs size.	96
4.5	Final structure obtained after thermal treatment TT3 of modelled NPs (a) [SnO ₂] ₁₅ , (b) [SnO ₂] ₂₃ , (c) [SnO ₂] ₃₁ , (d) [SnO ₂] ₄₈ , (e) [SnO ₂] ₆₉ , and (f) [SnO ₂] ₁₀₃ , respec- tively.	97
4.6	Total Neutron PDFs calculated from the 6 NP models obtained after TT3 heat treatment and compared with the experimental PDF obtained by total neutron scattering from Ref. [131].	98
4.7	Calculated partial PDFs of (a) Sn-O, (b) O-O, and (c) Sn-Sn distances as a function of size compare with to bulk.	99
4.8	Average distances of Sn-O pairs of atoms as a function of the distance (r) from the nanoclusters center for (a) [SnO ₂] ₁₅ , [SnO ₂] ₂₃ , [SnO ₂] ₃₁ and (b) [SnO ₂] ₄₈ , [SnO ₂] ₆₉ , [SnO ₂] ₁₀₃ nanoclusters.	101
4.9	Histogram of (a) Sn-O, (b) O-O and (c) Sn-Sn distances for various sizes of nanoclusters compared with the calculated PDF of bulk SnO ₂	102
4.10	Fragment of the smallest model ([SnO ₂] ₁₅) with surface atoms. The length of the double bridges is indicated by green arrows and that of the single bridges by blue colors.	103
4.11	Fraction of coordination number of Sn-atoms within the core and the surface for (a) [SnO ₂] ₃₁ , (b) [SnO ₂] ₄₈ , (c) [SnO ₂] ₆₉ and (d) [SnO ₂] ₁₀₃ nanoclusters.	104
4.12	(a) Sn-O-Sn angle distribution from the core and surface of nanoclusters com- pared with the bulk. (b) An example of the angle distribution from a small fragment of the nanocluster core and surface.	105
4.13	Average coordination number of Zr atoms in the core and those at the surface for (a) ZrO ₂ and (b) SnO ₂ systems.	106
5.1	Evolution of band gap with the fraction of Hartree-Fock exchange.	110
5.2	Total density of states (TDOS) obtained for the cubic and monoclinic polymorphs of zirconia using PBE (a) and PBE0 (b) approximations.	111
5.3	Partial density of states (PDOS) obtained for the cubic zirconia using PBE (a) and (b) PBE0 functional. Similarly, PDOS obtained for monoclinic polymorph using (c) PBE and (d) PBE0 approximations.	112
5.4	Molecular orbitals (MOs) plot for HOMO and LUMO of the cubic phase zirconia using PBE and PBE0 functionals by considering the isosurface value of 2 %. Zr atoms in grey balls and O atoms in red balls.	113

5.5	Partial and total density of states of ZrO ₂ nanocluster models with maximum passivation rate using PBE and PBE0 approximations.	114
5.6	Partial and total density of states for NP models [ZrO ₂] _n , n = 14, 16, 43, 80 and 141 with maximum passivation rate represented on the same scale: (a) PBE and (b) PBE0.	115
5.7	PDOS for partially passivated nanoparticles with 33.33 % and 16.66 % surface passivations (a), (b) for [ZrO ₂] ₄₃ and (c), (d) for [ZrO ₂] ₁₄₁ nanoclusters, respectively.	116
5.8	Computed energy band gap difference of NPs relative to that of the bulk material $\Delta E_g = E_g^{NP} - E_g^{bulk} = \beta/d^\alpha$ as a function of the NPs size. The solid lines are the fitted curves: $\Delta E_g = 0.917/d^{1.783}$ and $\Delta E_g = 0.86/d^{2.782}$ for (a) PBE and (b) PBE0 approximations.	117
5.9	Evolution of experimental band gap as a function of SnO ₂ particle size. Extracted data from Ref. [7]	117
5.10	Partial density of states (PDOS) for the atoms in core and surface of (a) [ZrO ₂] ₄₃ , (b) [ZrO ₂] ₈₀ and (c) [ZrO ₂] ₁₄₁ nanoclusters with maximum surface passivation. PDOS of surface atoms are shifted vertically for clarity.	118
5.11	Molecular orbitals (MOs) plot for HOMO and LUMO of the [ZrO ₂] _n , n=43, 80 and 141 with 100 % surface passivation using PBE0 functionals. The isosurfaces are shown in yellow and blue, representing values of +0.06 and -0.06, respectively.	119
5.12	Partial density of states (PDOS) for the atoms in core and surface of [ZrO ₂] ₄₃ and [ZrO ₂] ₁₄₁ nanoclusters with 33.33 % (a, b) and 16.66 % (c, d) surface passivation. PDOS of surface atoms are shifted vertically for clarity.	120
5.13	Molecular orbitals (MOs) plot for HOMO and LUMO for [ZrO ₂] ₄₃ and [ZrO ₂] ₁₄₁ nanocluster models with 33.33 % and 16.66 % surface passivation, using PBE0 functionals. The isosurfaces are shown in yellow and blue, representing values of +0.06 and -0.06, respectively.	121
5.14	Evolution of band gap with the fraction of HF correaltion.	122
5.15	Total density of states of tetragonal phase of SnO ₂ using (a) PBE and (b) PBE0 approximation.	123
5.16	Partial density of states of tetragonal phase of SnO ₂ using (a) PBE and (b) PBE0 approximation.	123
5.17	Partial and total density of states of [SnO ₂] nanoclusters using (a) PBE and (b) PBE0 approximation.	124
5.18	Calculated band gap of tetragonal phase of tin (IV) oxide and their modeled nanoclusters with LDA, PBE and PBE0 functional, respectively.	125

5.19	Partial and total density of states for various models $[\text{SnO}_2]_n$, $n = 15, 23, 31, 48, 69$ and 103 , using (a) PBE and (b) PBE0 approximations.	126
5.20	Calculated band gaps of different size of SnO_2 nanoclusters. The solid lines are the fitted curves: $\Delta E_g = 1.572/d^{1.70}$, $\Delta E_g = 1.51/d^{1.93}$ and $\Delta E_g = 1.91/d^{2.03}$ for (a) LDA compared with literature [82], (b) PBE and (c) PBE0 compared with experiment [7].	126
5.21	Partial density of states for the atoms in core and surface of (a) $[\text{SnO}_2]_{31}$, (b) $[\text{SnO}_2]_{48}$, (c) $[\text{SnO}_2]_{69}$ and (d) $[\text{SnO}_2]_{103}$ nanoclusters. PDOS of surface atoms are shifted vertically for clarity.	128
5.22	Comparison of computed energy band gap difference of ZrO_2 and SnO_2 NPs relative to that of the bulk material $\Delta E_g = E_g^{NP} - E_g^{bulk} = \beta_{NP}/d^{\alpha_{NP}}$ as a function of the NP size using (a) PBE and (b) PBE0 functional.	130

List of Tables

3.1	Calculated and experimental cell parameters for cubic, monoclinic, and tetragonal phases of zirconia.	75
3.2	Fraction of coordination number for Zr-atoms within the core and the surface for various size of nanoclusters.	90
5.1	Calculated band gap of zirconia models along with their standard deviation (\pm) using PBE and PBE0 functionals	115
5.2	Molecular orbitals plot for HOMO and LUMO of the $[\text{SnO}_2]_n$ nanocluster models using PBE0 functionals. The isosurfaces are shown in orange and blue, representing values of +0.02 and -0.02, respectively.	129



General introduction

Nanocrystalline materials have captured significant interest in contemporary science and emerging technologies owing to their distinct characteristics compared to traditional micrometer-scale materials. In particular, metal oxide nanoparticles, play a pivotal role in advancing several fields such as materials science, medicine, catalysis, and environmental science. Specifically, they are recognized as effective systems in various industrial applications such as optical and microelectronics devices, sensors, high-durability coatings, and solid oxide fuel cells (SOFC) [1]–[4].

The chemical and physical activity of nanocrystalline metal oxide systems is governed by their composition, structure, and size. In particular, nanocrystalline formations, such as nanoparticles (NPs), nanowires, and thin films, have become particularly prominent thanks to their unique and unconventional structural features, diverging from their perfect crystalline counterparts. Nanoparticles, for instance, exhibit a unique form of structural disorder [5], influenced by their small size, leading to significant alterations in their properties. The tiny dimensions of NPs result in quantum confinement effects, leading to unusual and size-dependent physical features [6]–[8]. While the quantum confinement effect is well established, much remains to be done to fully understand the properties of nanocrystals. In particular, the alterations in structure induced by size effects, vital for comprehending size-property relationships, remain inadequately understood, partly due to the challenges encountered in synthesizing and experimentally characterizing "ultrasmall" NPs ($\sim 2-3$ nm) objects [1]. This problem cannot be tackled experimentally alone and requires the use of modelling and simulation methods [9]. However, an additional complication arises from the point of view of modelling NPs. The presence of real NPs as isolated, stoichiometric and chemically pure entities in a vacuum is improbable. In practice, real NPs can be subject to the presence of contaminants, mainly located on their surfaces, which can impact the structure of the nanoparticles through surface relaxation and reconstruction and can even propagate to affect the core region [10]. The ratio of surface to core atoms of the NP increases noticeably as the particle size approaches the exciton Bohr radius, which results in the surface properties of the material playing a significant influence on its overall properties [11]–[14]. With this backdrop, this thesis endeavors to enhance the structural understanding of metal oxide nanocrystals, with a specific focus on how size impacts their structures and electronic properties.

In literature, a wide range of metal oxide nanoparticles were studied, encompassing titanium dioxide (TiO_2), iron oxide (Fe_2O_3 , Fe_3O_4), zinc oxide (ZnO), copper oxide (CuO , Cu_2O), zirconium dioxide (ZrO_2), silicon dioxide (SiO_2), tin dioxide (SnO_2), etc., Among these compounds, zirconium dioxide (zirconia) is particularly intriguing due to its remarkable intrinsic properties, including complex polymorphism and stability in nanocrystalline forms under conditions where macroscopic stability is not observed. This research primarily focuses on zirconia due to its technological importance. Similarly, tin dioxide (SnO_2) also exhibits unique properties at the nanoscale and finds a widespread use in photocatalysis making it another pivotal material of interest. Furthermore, the choice of these two systems is also motivated by the fact that these are among the most studied ceramic materials. In particular, some of the previous research related to synthesize the ZrO_2 nanoparticles have been done at IRCER laboratory in Limoges, where a successful synthesis of nanoparticles of size 2~3 nm has been achieved. These experiments provide us a valuable set of measurements that allow us to confront our NP models with experiments granting thereby a high level of reproducibility of our modelling methodology, provides insights into the structural characteristics of ZrO_2 nanoparticles and contributes to a more comprehensive understanding of their electronic properties. Therefore, in this work, we specifically focus on modeling ZrO_2 and SnO_2 NPs, with a primary objective of comprehensively investigate their structural properties, core-shell contributions, electronic characteristics, and quantum confinement effects.

By employing first-principles molecular dynamics (FPMD), this research aims to model ZrO_2 and SnO_2 nanoclusters across varying sizes while maintaining stoichiometric integrity. The modeling protocol aims to reproduce experimentally measured pair distribution functions (PDFs), enabling a detailed examination of core and surface structural features and their correlation with electronic properties. Through this approach, the thesis aims to contribute to a deeper understanding of the complex interplay between nanoparticle structure and properties, laying the foundation for future advancements in nanotechnology and materials science. The thesis is organized into five chapters as outlined below.

The first chapter provides a historical overview of nanoparticles, tracing their origins and highlighting their contributions to technological advancements. It briefly discusses the structure of ZrO_2 and SnO_2 polymorphs and delves into the structure and electronic properties of ZrO_2 and SnO_2 nanoparticles based on prior works in the literature.

In chapter 2, the fundamental concepts of ab-initio modeling techniques are explained with a

focus on the utilization of ab-initio molecular dynamics (AIMD) as an efficient computational tool for investigating various material properties. This chapter concludes by exploring electronic structure techniques, with a specific focus on the electronic density of states.

Chapter 3 focuses on generating ZrO_2 NP atomistic models. Various surface passivation rates are applied to address dangling bonds and investigate the nanoparticles, resulting in a closer agreement with experimental observations. The structural dependence on temperature during MD simulations is studied, along with the impact of changing the size of NP models. Moreover, we are able to disentangle the core and surface atoms of nanoclusters by evaluating the evolution of the Zr-O bond length as a function of the position of the atoms in the NP. This allow us to explain the features in the PDFs in comparison to cubic and monoclinic phases of ZrO_2 .

In chapter 4, we focus on creating SnO_2 nanocluster models and analyze their structures in comparison to experimental results. Different passivation techniques are tested to address dangling bonds and produce reliable nanocluster models. The structural changes as a function of nanocluster model size are examined. Finally, the core and surface atoms of nanocluster models are disentangled and their structures studied.

The last chapter deals with the calculation of electronic properties for the modeled ZrO_2 and SnO_2 nanoclusters using various exchange-correlation functionals within density functional theory. Quantum confinement effects are observed when reducing the size of the modeled nanoclusters. A comparative analysis of electronic properties between ZrO_2 and SnO_2 systems is presented, with a specific focus on discussing the quantum confinement effect.



1

Literature review

Summary

1.1	Nanomaterials and metal oxide nanoparticles	22
1.2	Structure of the fluorite-derived zirconia polymorphs	28
1.2.1	Cubic phase of zirconia	29
1.2.2	Tetragonal phase of zirconia	30
1.2.3	Monoclinic phase of zirconia	30
1.2.4	Orthorhombic I phase of zirconia	31
1.3	Structure of cassiterite tin dioxide	31
1.4	Structure of "ultrasmall" nanoparticles	33
1.5	Surface passivation of NP models	39
1.6	The relation between band gap and nanoparticle size	46
1.7	Conclusions	50

1.1 Nanomaterials and metal oxide nanoparticles

The progress of various fields in science and engineering has been significantly propelled by nanotechnology, often considered the foundational technology of the 20th century. Nanotechnology involves the manipulation of materials at the nanoscale, leading to nanomaterials with novel properties and applications. The use of nanomaterials dates back to Roman times, long before the craftsmen who created complex objects using these materials were aware of the underlying physical mechanisms. Examples of its historical use include the manipulation of gold and silver nanoparticles to achieve colour-changing effects, as in the case of Lycurgus' cup [15] shown in Figure 1.1. Similarly, the creation of different colors in medieval stained glass windows in churches during the 4th and 6th centuries represents another early application of nanotechnology. These instances highlight the ancient roots of nanotechnological practices that have had a lasting impact on various technological and artistic endeavors [16].



Figure 1.1: Lycurgus Cup. (a) It appears green when viewed in reflected light, such as during the day, and (b) appears red when light is shone into the cup and transmitted through the glass. Taken from Ref. [15].

The turning point for nanotechnology came with Richard Feynman's lecture titled "There's Plenty of Room at the Bottom", delivered at the California Institute of Technology in 1959 [17].

Feynman’s talk not only raised various issues but also proposed solutions related to the manipulation of matter at the atomic level, sparking significant interest in the theories and concepts of nanotechnology.

The term “nanotechnology” was first coined during a conference in 1974 by the Japanese scientist Norio Taniguchi from Tokyo University of Science. He used the term to describe semiconductor techniques involving precise control on the order of a nanometer scale, encompassing processes like thin film deposition and ion beam milling [18]. However, it was only in 1981, with the invention of the scanning tunneling microscope, that humans were able to visually observe individual atoms for the first time. The creators of this groundbreaking technology, Gerd Binnig and Heinrich Rohrer, were awarded the Nobel Prize in Physics in 1986 [19].

Subsequently, interest in nanoscience and nanotechnology has surged, as evidenced by the growth in the number of publications associated with the term “nanotechnology” from the early 21st century to the present (see Figure 1.2). Between 2000 and 2019, the Web of Science database recorded over 1.8 million articles related to nanotechnology, demonstrating an average annual growth rate of 13.9 %, according to StatNano [20]. This reflects the substantial expansion of research and development activities in the field of nanotechnology.

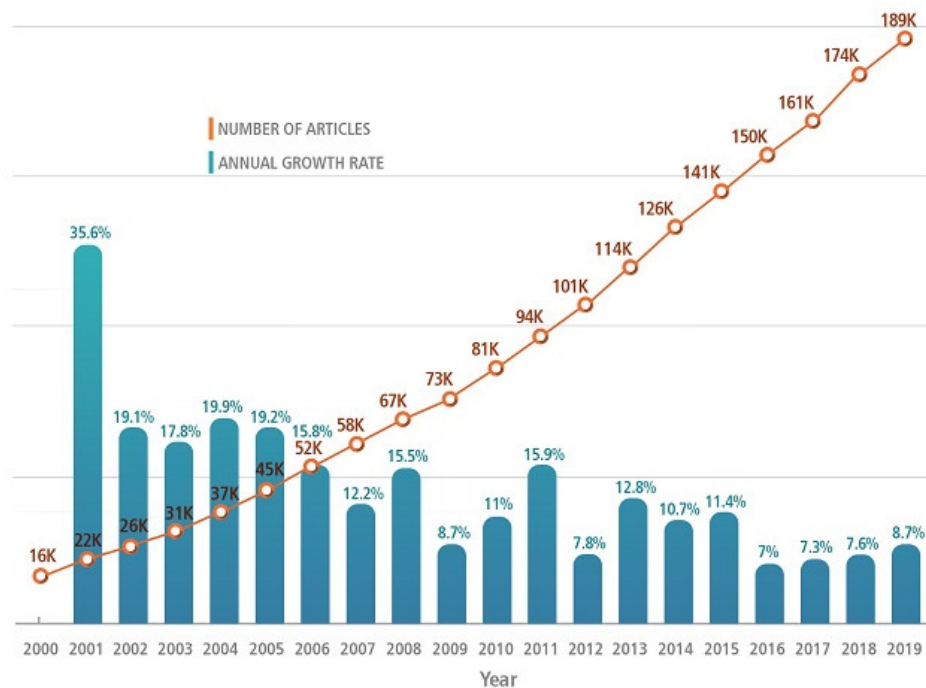


Figure 1.2: Evolution of the number of articles and annual growth rate in nanotechnology since 2000–2019. Taken from Ref. [20].

The distinctive characteristics of nanomaterials have given rise to many potential applications in a wide range of scientific and technical fields, including electronics, energy and health, as shown in Figure 1.3 [21].



Figure 1.3: Various applications of nanoparticles in nanotechnology. Taken from Ref. [21].

Nanomaterials can consist of a single chemical element or a combination of several elements. They can be metallic, ceramic, organic, amorphous or crystalline. They generally covers highly variable objects with a characteristic size ranging from 1 to 100 nm. This scale is obviously significantly below the detection limit of the unaided human eye (Figure 1.4), which is around 100 micrometers. Many authors use a more precise definition based on the size below which a particular property is observed to be exacerbated [6].

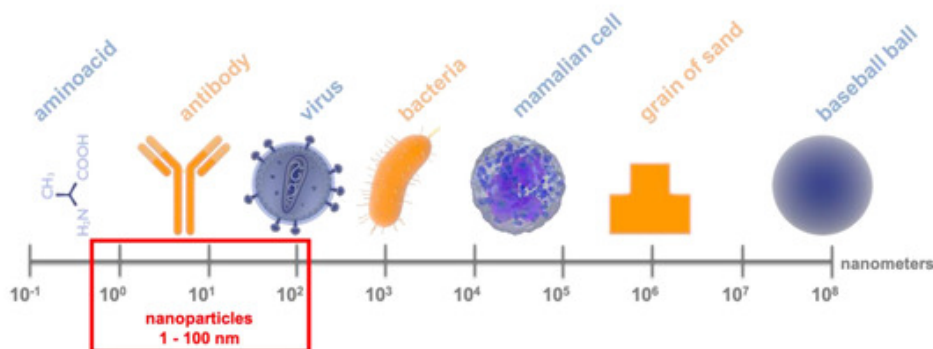


Figure 1.4: General scale of nano-materials. Taken from Ref. [22].

Nanomaterials are influenced by their size and shape, but they are generally classified according to their dimensions (0D, 1D and 2D), which gives them common characteristics. In 0-dimensional nanomaterials, namely nanoparticles and quantum dots, electrons are confined in the three dimensions of space. In this case, there is no delocalisation of electrons. In one-dimensional nanomaterials, e.g. nano-rods, quantum wires, electrons are confined in only two dimensions, i.e. electron delocalisation occurs along the long axis of a wire, rod or tube. In two-dimensional nanomaterials, the electrons are delocalised in the plane and confined throughout the thickness of the sheet (Figure 1.5).

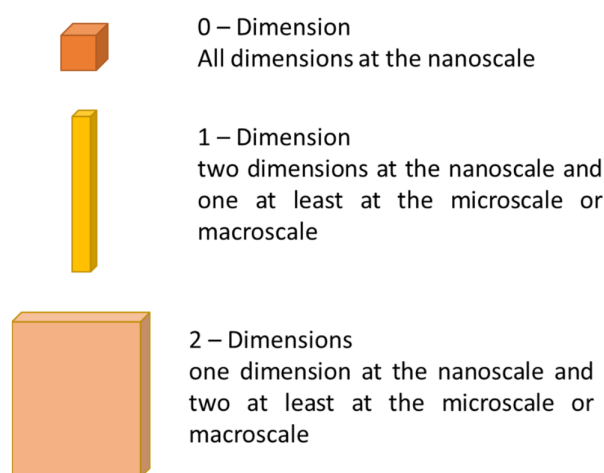


Figure 1.5: Possible dimensions of the nanoparticles. Taken from Ref. [23].

The underlying property that explains the considerable interest in nanomaterials is the quantum confinement. A simplified explanation is often given within the framework of molecular orbital theory. Starting from the discrete energy levels of the atoms, as the number of atoms in the system increases (due to its increase in size), the energy levels split and progressively transform into dense energy bands (Figure 1.6). Simultaneously, the broadening of the occupied and unoccupied orbitals leads to a reduction in the band gap, which eventually converges towards the value of the bulk material. Quantum confinement is thus characterised by an increase in the band gap as the size of the nanomaterial decreases [24]–[26], which makes the properties of nanomaterials, in particular optical and electronic properties, easily tunable as a function of their characteristic size [27], [28].

Quantum confinement manifests itself prominently in the optical properties of nanoparticles (NP), particularly in their absorption and emission spectra, leading to a blue shift in absorption and emission peaks as the NP size decreases [30], [31]. When semiconductor nanoparticles are excited by photon absorption, electrons from the valence band move to the conduction

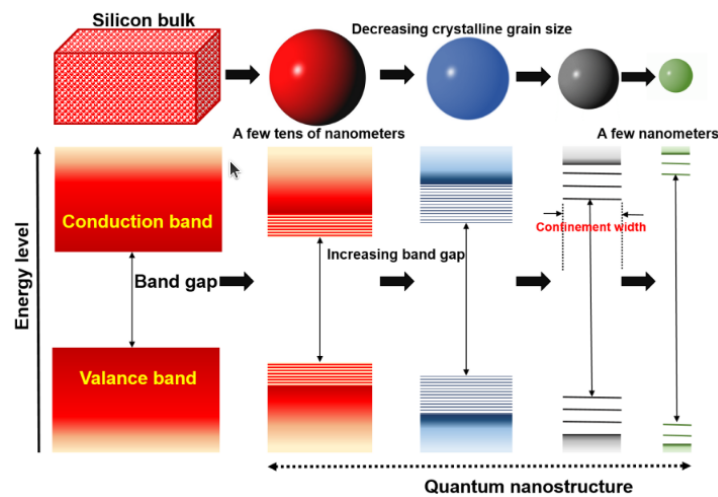


Figure 1.6: Schematic diagram of the bandgap variation in nanoparticles. Taken from Ref. [29].

band, forming electron-hole pairs. The return to the fundamental state involves the emission of photons, or fluorescence. This process, linked to quantum confinement, leads to a change in the colour emitted as a function of the size of the irradiated nanoparticles. This concept is illustrated in Figure 1.7, which shows that the fluorescence colour of CdSe-CdS nanoparticles changes from blue to red simply by varying the size of the NPs from 1.7 nm to 6 nm. This size-dependent behavior is utilized in various applications such as displays and sensors [32], [33]. This also highlights the importance of size control in tailoring properties to various applications. Understanding and exploiting these quantum effects is key to advancing nanotechnology and exploiting the unique properties of nanomaterials.



Figure 1.7: Fluorescence of CdSe-CdS nanoparticles with diameters varying from 1.7 nm (blue) up to 6 nm (red). Reproduction by H. Weller, University of Hamburg. Taken from Ref. [34].

Because of their small size, nanoparticles generally have a very high proportion of surface atoms, often higher than that of core atoms, which can lead to significant structural rearrangement. This size-dependent structural arrangement can lead to enhanced or altered chemical

properties in addition to the effects of quantum confinement. This may lead to variations in melting and boiling points, phase transition pressures, and temperatures, as well as unique optical, optoelectronic, catalytic, magnetic, and electric properties compared to their bulk counterparts or molecular species precursors [35]–[41].

In order to better understand the properties of nanoparticles, their structural determination is crucial. However, pinpointing the precise atomic arrangement in nanostructured materials is a significant issue that continues to pique the scientific community's interest today. In fact, there is still no systematic way to clearly resolve structures at the nanometric scale, as experimental techniques cannot provide unambiguous structural information and must be supplemented by modelling and simulation methods [9], [42]. The main experimental approaches are X-ray and neutron diffraction methods, Extended X-ray Absorption Fine Structure (EXAFS) technique, and Transmission Electron Microscopy (TEM). All these techniques face some challenges when dealing with nanoparticles. NPs exhibit unusual type of disorder [5] making evident that they cannot simply be regarded as miniature versions of crystals or bulk materials. They may exhibit dynamic behaviors, including surface reconstructions, making it challenging for experiments to capture a stable and representative structure [43]. They have high surface-to-volume ratios, which introduces complexities in distinguishing between surface and core structures. One of the experimental tools best suited to characterising the structure of NPs is the so-called atomic pair distribution function (PDF) method. The PDF gives the distribution of atomic distances in the material and can therefore be used to gather information on the short- and medium-range order of NPs. It is obtained from data corrected for powder diffraction (total scattering) by means of a Fourier transform, thus providing information about real space [44]. Additionally, it is one of the few methods that allow for the collection of quantitative structural data for the entire sample [23], [45]–[47]. In the present work, all the atomic-scale modelling and simulation methods are used in conjunction with the PDF method.

There exist numerous metal oxide nanoparticle systems, including titanium dioxide (TiO_2), iron oxide (Fe_2O_3 , Fe_3O_4), zinc oxide (ZnO), copper oxide (CuO , Cu_2O), zirconium dioxide (ZrO_2), silicon dioxide (SiO_2), tin dioxide (SnO_2), etc. In this work, we focus on the modelling of ZrO_2 and SnO_2 "ultrasmall" nanocrystals in order to characterize their structures and calculate their electronic properties. Zirconia and tin oxide are important oxide ceramic materials that have long been studied at IRCER, but their characteristics are clearly different. Zirconia has a complex polymorphism with 7- or 8-fold coordinated cations, more pronounced ionic chemical bonds and a single stable oxidation state for the metallic element. SnO_2 has only one polymorph at atmospheric pressure with 6-fold coordinated cations and tin atoms have 2 stable oxidation states. Earlier research conducted at IRCER has resulted in the successful synthesis of ZrO_2 ultrasmall nanoparticles, achieving sizes within the range of 1~3 nm. Similar efforts led only to the synthesis of SnO_2 NP with 5 nm diameter, which is comparatively much larger than the ZrO_2 NPs.

1.2 Structure of the fluorite-derived zirconia polymorphs

Zirconia, is a multipurpose ceramic with excellent mechanical strength, fracture toughness, hardness, resistance to wear, and thermal shock resistance [48], [49]. It is widely employed in numerous applications, such as automotive engines, cutting tools, and abrasives [50]. It is a suitable choice for thermal-barrier coatings in tough environments because of its low thermal expansion coefficient and great chemical resistance [51]. Zirconia is also a particularly effective oxygen-ion conductor [52] when doped with yttria, and is the leading electrolyte in solid oxide fuel cells. In recent years, there has been an increase in interest in zirconia's catalytic behavior and luminous features [53], [54].

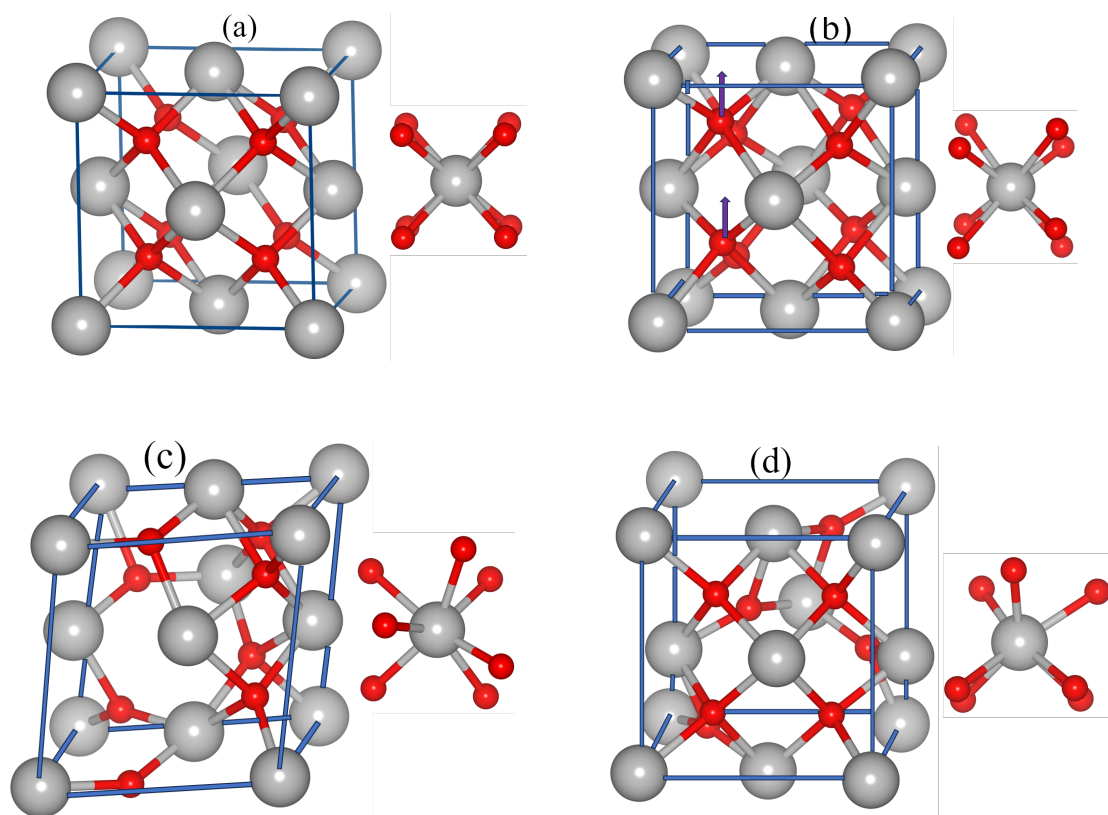


Figure 1.8: Unit cells of the four fluorite-derived zirconia polymorphs: (a) cubic, (b) tetragonal, (c) monoclinic, and (d) orthorhombic-I. The unconventional cell is used for the tetragonal polymorph in order to highlight its link with the fluorite parent phase.

Zirconia exists in five main crystalline forms, depending on temperature and pressure conditions. At atmospheric pressure, three polymorphs have been reported, namely the monoclinic (m) phase, which is thermodynamically stable up to 1543 K [55], the tetragonal (t) phase, stable between 1543 K and 2643 K [56], and the cubic (c) phase, stable above 2643 K until the melt occurs at 2979 K [57]. The cubic phase is isostructural with fluorite (CaF_2) and the tetragonal and

monoclinic phases are distortions of the parent cubic phase. The two high-pressure polymorphs have orthorhombic symmetry and are called "ortho I" and "ortho II" to represent the low- (3–11 GPa) and high-pressure (9–15 GPa) phases respectively [58], [59]. The ortho I phase also derives from fluorite and easily transforms into monoclinic when the pressure is released (the phase transition being considered martensitic). On the other hand, the ortho II phase is not related to fluorite but is isostructural with cotunnite (PbCl_2). Figure 1.8 shows the structural representation of zirconia based on fluorite-derived structures.

In the following, we describe the structure of the four fluorite-derived zirconia polymorphs, as well as their total and partial PDFs. Their unit cells and their cationic environments, are shown in Figure 1.8.

1.2.1 Cubic phase of zirconia

The cubic phase, with an ideal fluorite-type structure, crystallises with space group $\text{Fm}\bar{3}\text{m}$ (No. 225) and cell parameters $a = b = c = 5.10 \text{ \AA}$. The atomic positions in the asymmetric unit are: Zr in 0.0, 0.0, 0.0 and O in 0.25, 0.25, 0.25 [57]. Each zirconium cation is contained within a perfect cube of oxide ions, giving it 8-fold coordination. Figure 1.9 displays the calculated X-ray total and partial PDFs of the cubic-phase zirconia. We notice a number of peaks that are indicative of Zr-O, Zr-Zr, and O-O interatomic distances. The first peak corresponds to the Zr-O bond length and is located at 2.2 \AA . The second peak is at 2.6 \AA and correlates with the O-O distances. It is slightly visible next to the first peak. The third and highest intense peak is observed at 3.61 \AA and mainly corresponds to the first neighbours Zr-Zr distances, with a small contribution from the second O-O distances. The fourth peak, at 4.2 \AA is mainly due to Zr-O correlations. At larger distances, the peaks overlap more and more, making their attribution more difficult.

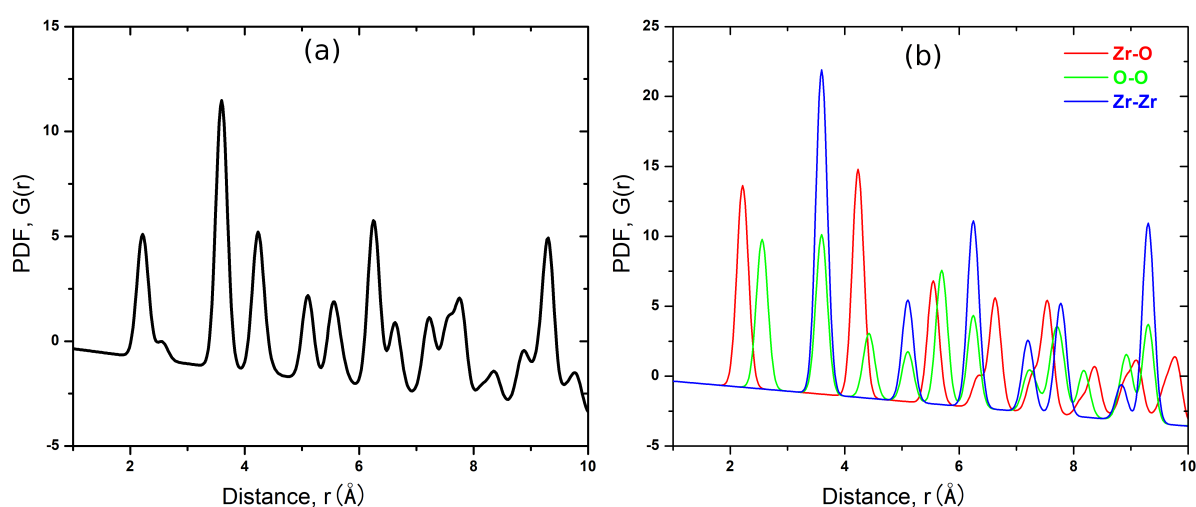


Figure 1.9: Calculated (a) total and (b) partial PDFs of cubic phase zirconia.

1.2.2 Tetragonal phase of zirconia

The tetragonal phase crystallizes with space group $P4_2/nmc$ (No. 137), $a = b = 3.64 \text{ \AA}$ and $c = 5.27 \text{ \AA}$. The atomic positions in the asymmetric unit are: Zr in 0.0 0.0 0.0 and O in 0.0 0.5, 0.185 [56]. Each zirconium cation is surrounded by eight oxygen anions to form a distorted cube. The calculated X-ray total and partial PDFs are plotted in Figure 1.10. We observe many peaks correlated with the Zr-O, Zr-Zr and O-O distances. The first two peaks, corresponding to the Zr-O bond lengths, are located at 2.0 \AA and 2.4 \AA . In comparison with the cubic phase, the first Zr-O peak is transformed into two peaks because of the slight shift of oxygen atoms along the c-axis in the tetragonal phase. The peak corresponding to the first O-O distances and positioned at 2.6 \AA is barely visible due to the low scattering contribution of O-atoms and the overlap with the second Zr-O peak. The most intense peak, corresponding to the first Zr-Zr distances, is located at 3.6 \AA , at similar distance as the cubic phase. The next peak, at 4.2 \AA and corresponding mainly to Zr-O distances, is broader than that of the cubic phase and is also a signature of the structural distortion of the tetragonal phase.

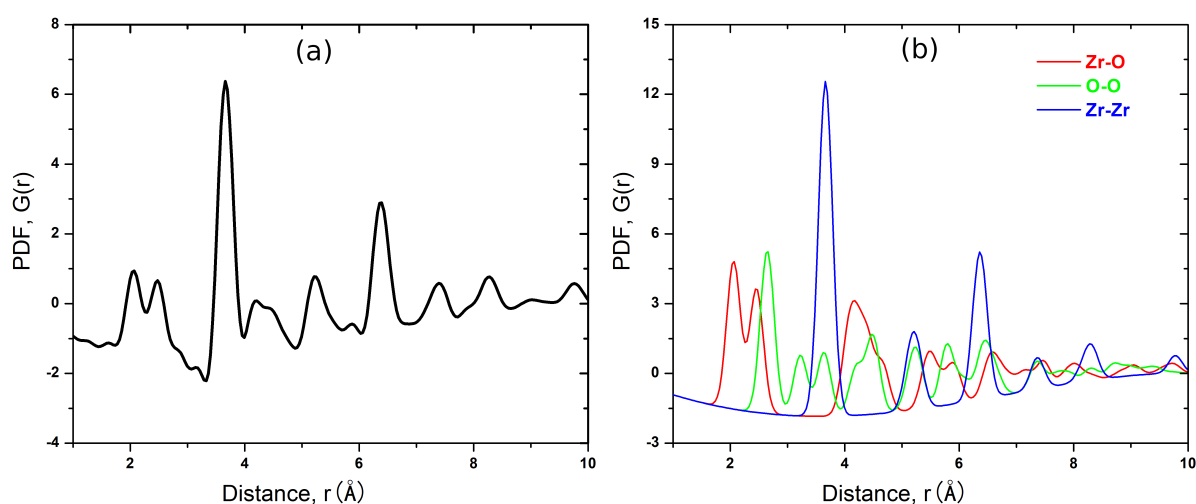


Figure 1.10: Calculated (a) total and (b) partial PDFs of tetragonal phase zirconia.

1.2.3 Monoclinic phase of zirconia

The monoclinic phase of zirconia (also called baddeleyite) is the least symmetrical of all the polymorphs and crystallises with space group $P2_1/c$ (No. 14) and cell parameters $a = 5.15 \text{ \AA}$, $b = 5.21 \text{ \AA}$ and $c = 5.32 \text{ \AA}$ with $\beta = 99.23^\circ$. The atomic positions in the asymmetric unit are: Zr in 0.275 0.039 0.208, O1 in 0.070 0.332 0.345 and O2 in 0.450 0.757 0.480 [55]. Figure 1.11 shows the calculated X-ray total and partial PDFs. The Zr-atom in monoclinic ZrO_2 has one less coordination number than the other two polymorphs, with each of these cations being seven-fold coordinated with regard to the oxygen anions. This results from a significant oxygen atom

shift that significantly distorts the fluorite oxygen cube and lowers the Zr coordination number. Therefore, a single peak around 2.2 Å actually reflects seven Zr-O distances, from 2.1 Å to 2.3 Å. The peak that correlates to the O-O distance is positioned around 2.5 Å and 3.0 Å and is made of multiple O-O distances as shown in Figure 1.11 (b). The two consecutive peaks positioned at 3.4 Å and 4.0 Å are mostly associated with the Zr-Zr distances. They partly merge with the Zr-O distances at 3.9 Å and 4.4 Å, leading to a triplet characteristic of the monoclinic phase PDF.

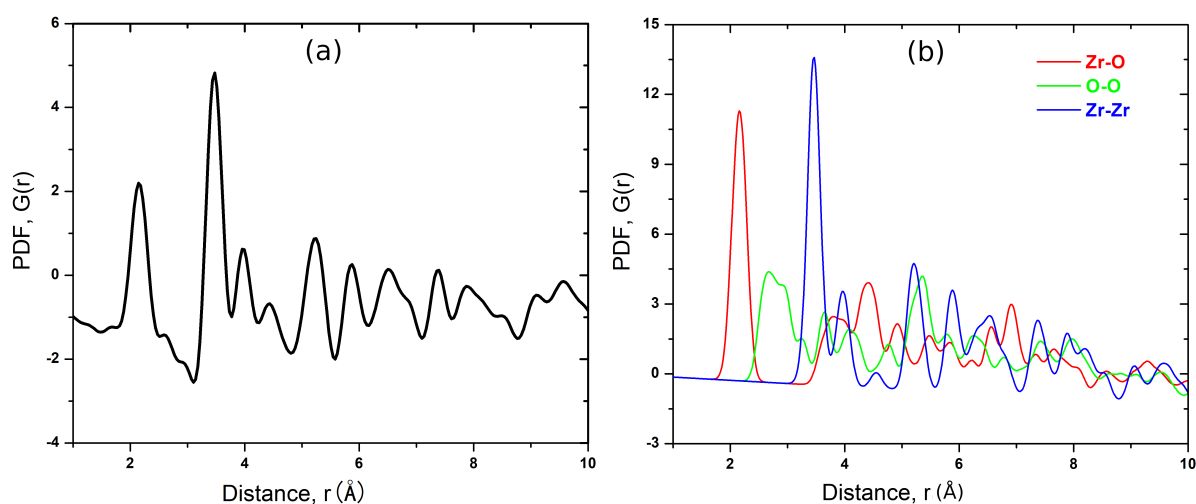


Figure 1.11: Calculated (a) total and (b) partial PDFs of monoclinic phase zirconia.

1.2.4 Orthorhombic I phase of zirconia

The ortho I phase crystallises in space group $Pbca$ (No. 61) with $a = 10.0861$ Å, $b = 5.2615$ Å, $c = 5.091$ Å and atoms in positions Zr: 0.8843 0.0332 0.2558 O1: 0.07911 0.3713 0.131 and O2: 0.9779 0.7477 0.4948 [58]. Compared with the other polymorphs, it is more symmetrical than the monoclinic, but less symmetrical than the tetragonal. Due to the substantial deformation of the ideal fluorite structure, it features a 7-fold coordinated zirconium cation surrounded by oxygen anions, just like the monoclinic phase. Therefore, a single peak is observed at 2.2 Å and represents the first Zr-O distances in Figures. 1.12. A low-intensity peak in the total PDF, corresponding to the O-O distances, is situated within the distance range of 2.5 Å to 3.1 Å. However, this peak becomes distinctly visible when examining the partial PDF. The second intense PDF peak associated with Zr-Zr distances is located at 3.4. Additionally, a PDF peak located at 3.8 Å, is a collective contribution from Zr-Zr, Zr-O, and O-O distances, as shown in Figure 1.12 (b).

1.3 Structure of cassiterite tin dioxide

Tin (IV) oxide, SnO_2 , or stannic oxide, exhibits unique properties as a special form of n-type semiconductor characterized by a relatively wide band gap of 3.6 eV at 300 K [60]. This material

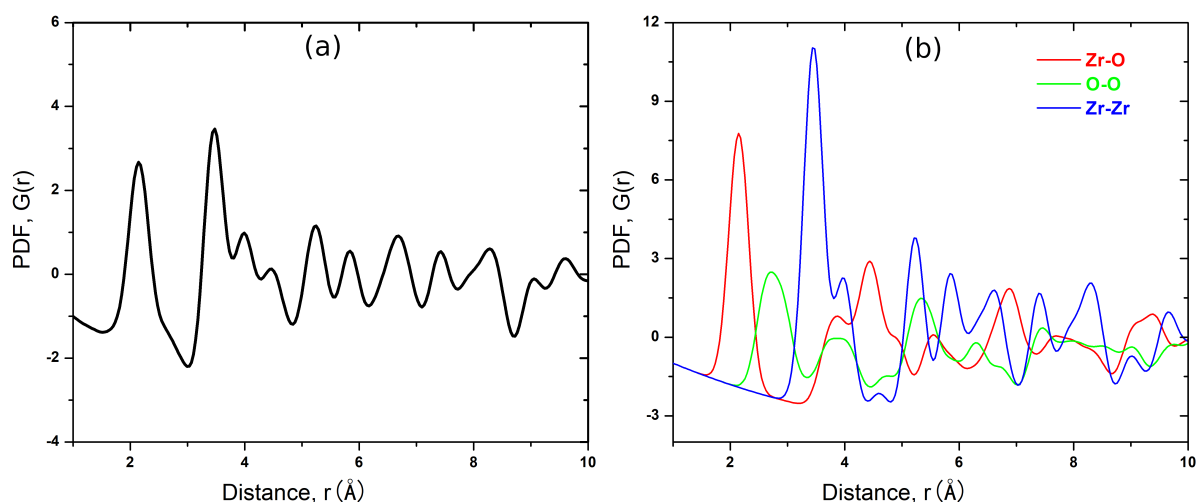


Figure 1.12: Calculated (a) total and (b) partial PDFs of orthorhombic I phase zirconia.

has garnered significant interest due to its intriguing electrical, optical, and electrochemical capabilities, leading to diverse applications. One notable application is in gas sensing, where SnO_2 serves as a sensitive component in gas sensors [61]. Additionally, it has proven effective as a catalyst in oxidation reactions [62]. Moreover, SnO_2 finds utility as a transparent electrical conductor, further expanding its range of applications [63].

In its natural mineral form, SnO_2 is known as cassiterite, and it crystallizes with the rutile-type structure. At atmospheric pressure, cassiterite represents the sole stable phase of this material. However, under high pressure SnO_2 exhibits extended polymorphism [64]. One phase transition occurs at 11.8 GPa, leading to the formation of the CaCl_2 -type phase with an orthorhombic structure (space group Pnmm), replacing the rutile phase. Another transition, observed at 12 GPa, results in an orthorhombic phase with the space group Pbcn , resembling $\alpha\text{-PbO}_2$ [65], [66]. These phases eventually convert to cubic structure with the space group $\text{Pa}3$, completing the transition at pressures of 21 GPa. The structure of SnO_2 is isostructural with TiO_2 rutile, crystallizing in tetragonal space group $\text{P4}_2/\text{mnn}$ (No.136) with $a = 4.74 \text{ \AA}$ and $c = 3.19 \text{ \AA}$. The atomic positions in the asymmetric unit are: Sn in 0 0 0 and O in 0.307 0.307 0. The unit cell is illustrated in Figure 1.13 (a). In this structure, tin atoms are coordinated to 6 oxygen atoms and are located in slightly distorted octahedra. Oxygen atoms are 3-fold coordinated by tin atoms, bridging three octahedra.

The calculated X-ray total and partial PDFs of SnO_2 are depicted in Figure 1.13 (b and c). Due to the much higher atomic number of Sn compared to O, the total PDF is dominated by Sn-Sn and Sn-O correlations. Even the strongest peak in the O-O distances, ranging from 2.59 Å to 2.90 Å , is barely visible in the total PDF. The first visible peak at 2.06 Å corresponds to Sn-O bond lengths. The second and third peaks at 3.19 Å and 3.72 Å are typical of the two shortest

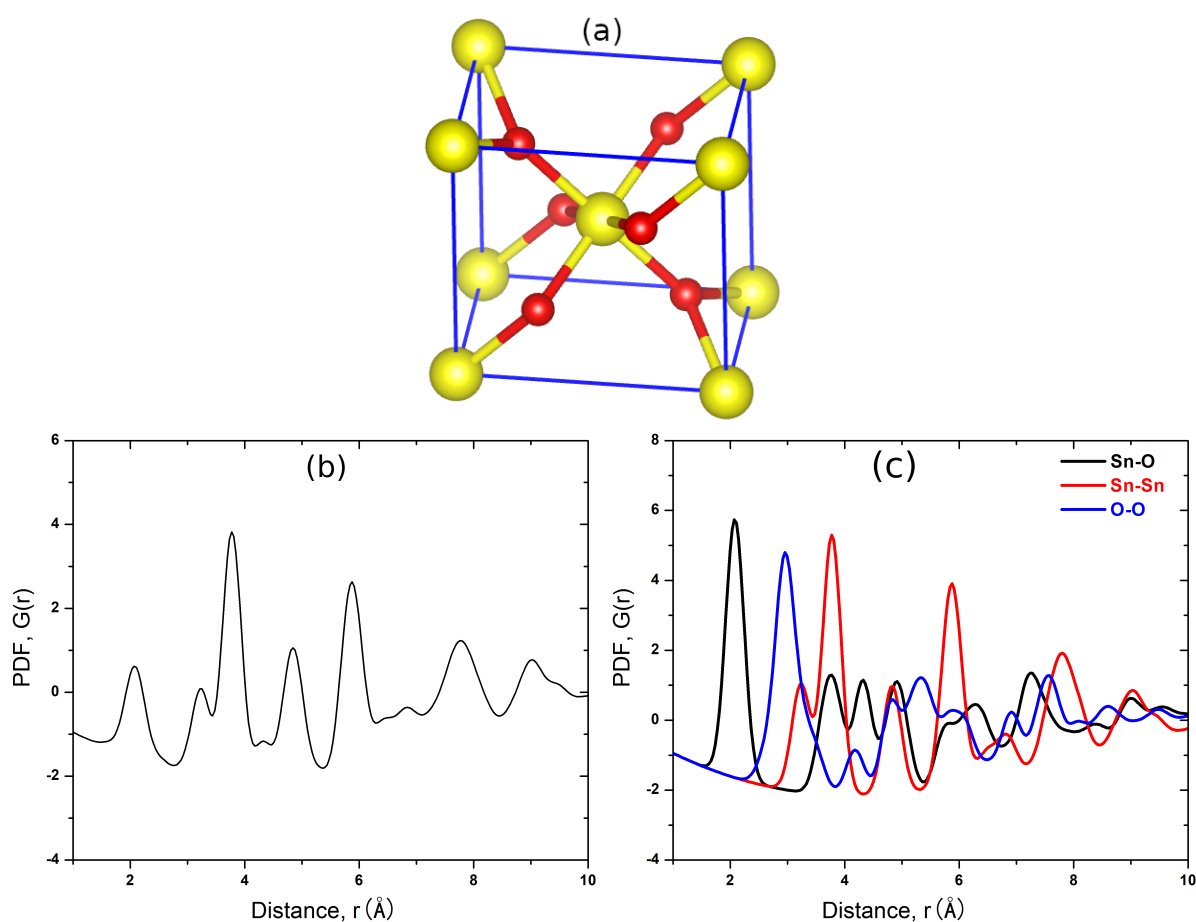


Figure 1.13: (a) Structural representation, calculated (b) total and (c) partial PDF of tetragonal SnO₂ rutile

Sn-Sn distances, with the third peak containing a minor contribution from Sn-O distances. The first Sn-Sn distance (3.19 Å) is equal to the cell parameter c and involves a double Sn^OSn bridge (between edge-shared octahedra), while the second (3.72 Å) involves a single Sn-O-Sn bridge (between corner-shared octahedra). The relative intensities of these two peaks can be explained by the difference in the number of double and single bridges, each Sn atom being linked to the next Sn atoms by 2 double bridges and 8 single bridges. The next intense peak at 4.74 Å corresponds to Sn-Sn distances equal to the cell parameter a and involves three tin atoms and two consecutive single Sn-O-Sn-O-Sn bridges.

1.4 Structure of "ultrasmall" nanoparticles

The structural characterization of metal oxide nanoparticles has been addressed by many authors over the last 20 years, with TiO₂ certainly being the most studied system (see Ref. [67]). These studies make extensive use of atomic-scale simulation methods (geometry optimization,

molecular dynamics, Reverse Monte Carlo), based on classical interatomic potentials or Density functional theory (DFT) calculations, and experimental data. Experimental data mainly comes from X-ray (and neutron) diffraction, in particular total scattering to obtain the atomic pair distribution functions of the studied materials. They are often supplemented by TEM observations and EXAFS experiments. Most of the studies, however, concern relatively "large" nanoparticles, with the smallest ones having a diameter of around 4 -5 nm, which often exhibit facets and/or a well-defined structure, close to the bulk counterpart [67]–[71]. For the largest nanoparticles (~ 10 nm in diameter), characterization is generally focused on the surface stabilization effect based on the study of 2D-periodic surfaces and the use of the results to describe the effects of hydration on surface energetics and relaxation for different facet indices [67], [72], [73]. An illustration is given in Figure 1.14 in the case of the study of monoclinic zirconia nanocrystals. For the smallest NPs (~ 4 -5 nm diameter), the main and well accepted result is the presence

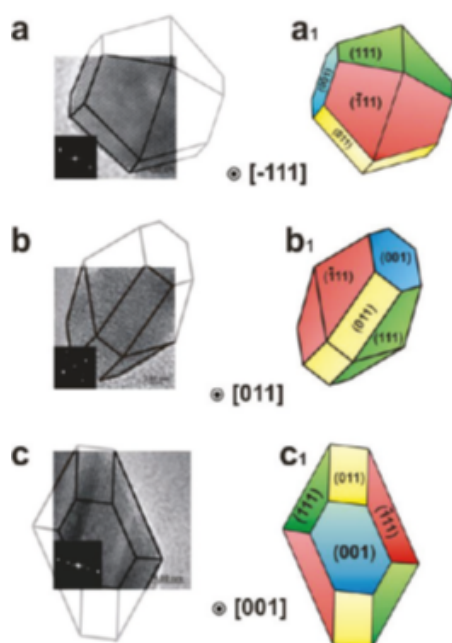


Figure 1.14: TEM pictures of the monoclinic zirconia nanocrystals (a, c) together with the calculated Wulff shapes (a1, c1), oriented along $[-111]$, $[011]$, and $[001]$ directions to align with the observed 2D images. Taken from Ref. [72].

of a core-shell structure, composed of a nearly amorphous surface layer and a particle interior with essentially bulk crystalline structure [67]. This is illustrated in Figure 1.15 for a ~ 5 nm anatase NP model obtained by molecular dynamics. Note that the model does not include any surface passivation, which corresponds to a simple model of particle in a vacuum. Other studies rely on the formation of nanoparticles in the reaction medium. This is done experimentally with in-situ synchrotron PDF experiments using very fast-acquisitions (a few seconds) [69], [70], [75]. In this case, the structural analysis focuses more on the very first stages of nanoparticle

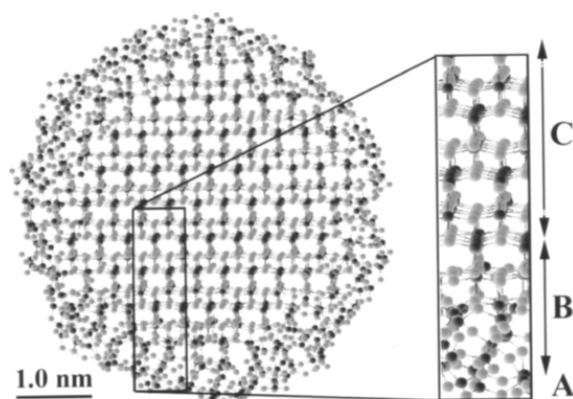


Figure 1.15: Molecular dynamics simulation prediction of the structure (cross section) of an ~ 5 nm anatase particle in vacuum. The surface layer (A) and the near-surface layer (B) are highly distorted, but the interior of the nanoparticle (C) retains typical anatase bulk structure. Region C disappears as particle diameter decreases toward ~ 2 nm. Taken from Ref. [74].

formation and on the relationship with the precursor structure, rather than on the structure of the NPs produced.

Studies on "ultra-small" particles of the order of 1 -3 nm are very scarce, and those on ZrO_2 nanoparticles are even rarer, which is certainly a consequence of the great difficulty of synthesizing and stabilizing such small particles. Reducing the size from 4 nm to 2 nm is expected to have very significant effects on the structure, as the number of surface atoms become larger than that of the particle core (and there is no longer facets, edges and corners). The resulting structure can be very different from all known crystalline polymorphs. This is illustrated with Figure 1.16, which shows the model of ~ 2 nm TiO_2 nanoparticle obtained from reverse Monte Carlo simulation, PDF and EXAFS data, exhibiting a clearly amorphous structure.

One of the first structural studies of "ultra-small" ZrO_2 nanocrystals dates back to 2005 [45]. It focused on the modelling of experimental X-ray synchrotron PDFs of samples obtained by intensive grinding of micrometric monoclinic zirconia powder. In this work, the authors showed several interesting results. Firstly, the PDFs cannot be correctly modeled in their entirety by any of the structures of the various polymorphs of zirconia. The greatest disagreement is obtained for the smallest nanocrystals (~ 3 nm). They also observed that the cubic structure reproduces the PDF at larger distances, while the monoclinic polymorph seems to better explain the PDF details at low distance values. Finally, they showed that the PDF can be correctly reproduced by refining a structural model consisting of $5 \times 5 \times 5$ cubic unit cells, but whose atomic positions can vary with the degrees of freedom of the monoclinic model. Figure 1.17 shows the good quality of their refinement using this supercell structural model.

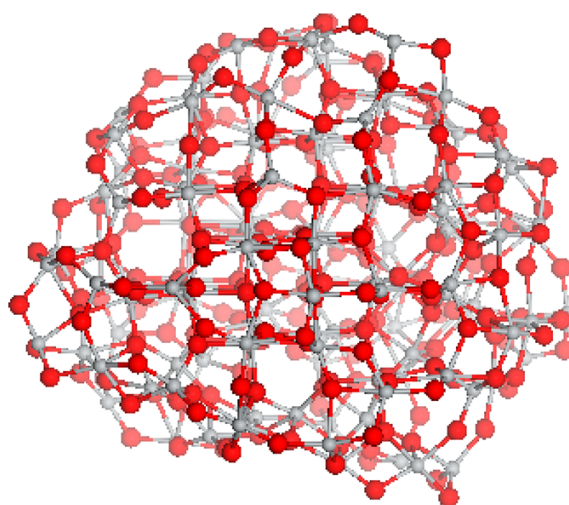


Figure 1.16: Structure of a ~ 2 nm TiO_2 nanoparticle obtained from reverse Monte Carlo simulation using both experimental PDF data and EXAFS spectra. Taken from Ref [76].

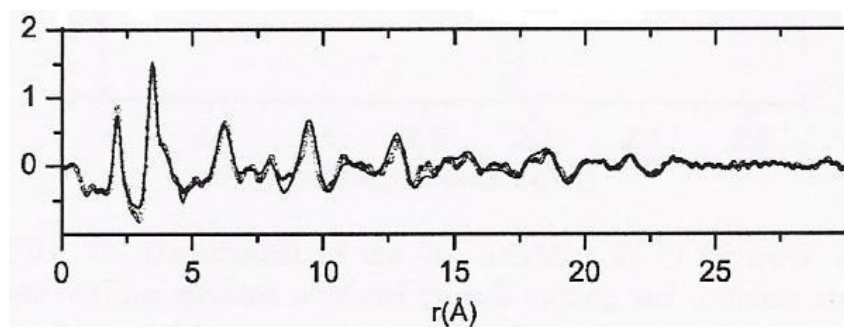


Figure 1.17: Fit of the experimental PDF of ZrO_2 nanocrystals obtained by intensive grinding of micrometric monoclinic zirconia powder, from Ref. [77].

We summarize below the latest work carried out at IRCER on the structure of very small ZrO_2 NPs, some of whose experimental results are used in this thesis [23]. In this study, different non-hydrolytic sol-gel routes were used in order to synthesize zirconia NPs with various sizes. In one of them, the sample was prepared with zirconium isopropoxide-isopropanol adduct in alkaline benzyl alcohol at 210°C for a duration of three days. Figure 1.19 illustrates the TEM images of the synthesized zirconia nanoparticles alongside the size distribution analysis, employing 70 particles data points. The obtained average particle diameter is 3.2 nm. The structural characteristics of the resulting sample were scrutinized first using Rietveld refinement, which showed that the prepared sample belongs to the tetragonal or cubic phase of zirconia with refined average apparent size of about 3 nm (consistent with TEM observation). However, the PDF analysis showed that although the PDF envelop resembles that of the tetragonal or cubic

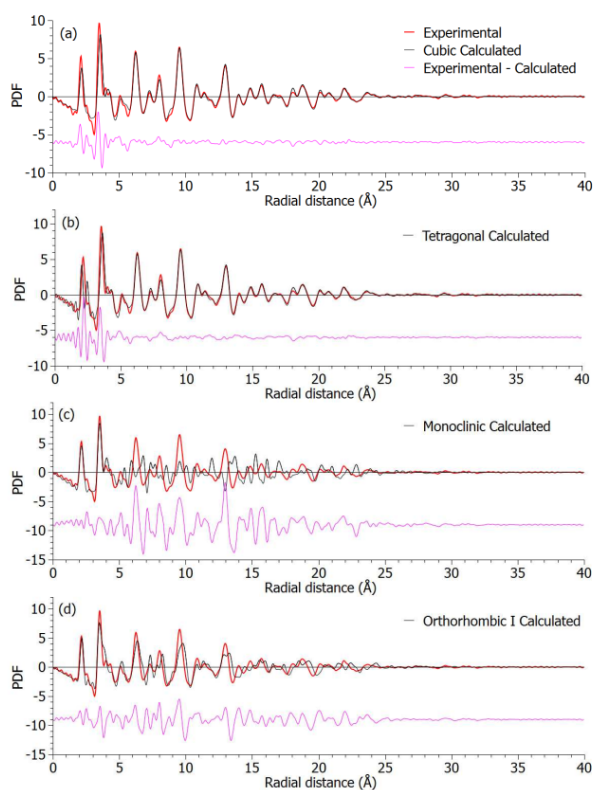


Figure 1.18: Experimental PDF of the zirconia particles produced at 210 °C for 3 days in benzyl alcohol with 0.2 mol.L⁻¹ NaOH with the (a) cubic model, (b) tetragonal model, (c) monoclinic model, and (d) orthorhombic I model of zirconia. Taken from Ref. [23].

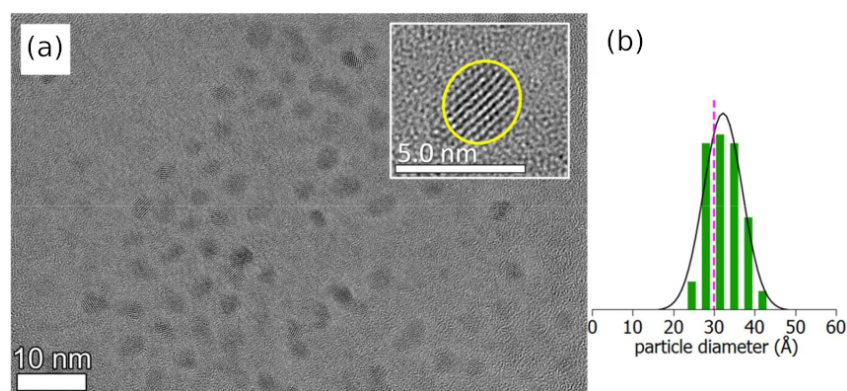


Figure 1.19: (a) TEM micrographs of the zirconia particles synthesized at 210 °C for 3 days in benzyl alcohol and (b) size dispersion analysis with 70 data points for the benzyl alcohol sample. Taken from Ref. [23].

polymorphs for largest r values, the short-range region ($r < 5 \text{ \AA}$) is different. In particular, the peaks between 2 \AA and 5 \AA exhibit clear deviations and similarities with the monoclinic model, as depicted in Figure 1.18 (c and d). Although this study reports that it is tempting to speculate that the sample may be a mixture of tetragonal and monoclinic phases, the PDF peaks in both short-range and medium-range regions that would correlate to the mixture of phases indicates the opposite. Instead, it was suggested that the sample exhibits a local structure closer to the monoclinic phase and a medium-range order comparable to the tetragonal phase. This study also addresses XRD measurements, elucidating the reasons behind the XRD pattern resembling that of a tetragonal phase. However, it suggested that the true structure is neither tetragonal nor monoclinic. Therefore, for convenience, the authors refer to this sample as a tetragonal-like structure.

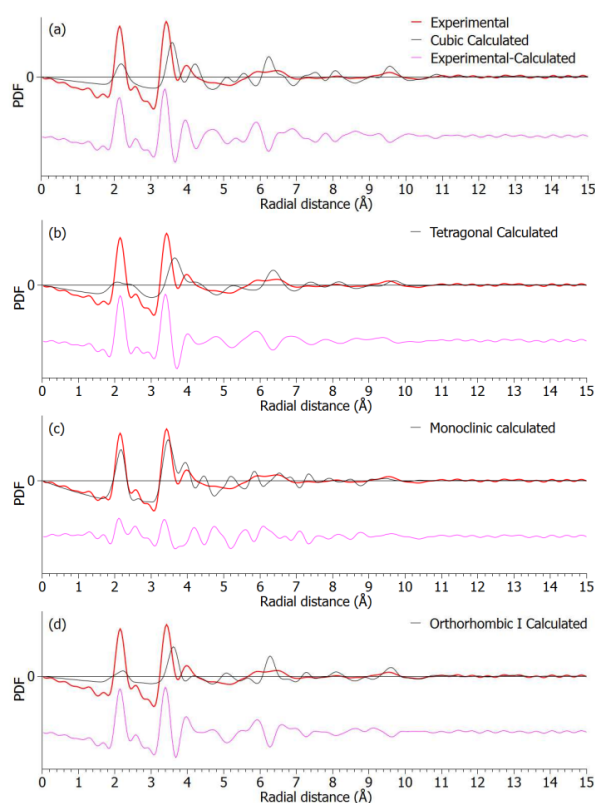


Figure 1.20: (a) Experimental PDF of the zirconia particles produced at $210 \text{ }^\circ\text{C}$ for three days in anisole with 0.2 mol.L^{-1} NaOH compared with the unrefined (a) cubic model, (b) tetragonal model, (c) monoclinic model, and (d) orthorhombic I model of zirconia. Taken from Ref. [23].

A second series of samples was prepared using anisole as a solvent to obtain even smaller NPs [23]. Figure 1.21 (a) and (b) displays the TEM image of the synthesized zirconia nanoparticles and the size distribution analysis using 49 particles data points. The obtained average

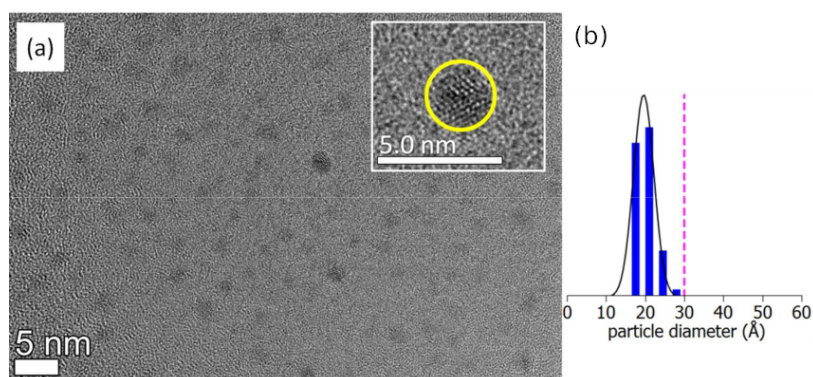


Figure 1.21: (a) TEM micrographs of the zirconia particles synthesized at 210 °C for 3 days in anisole and (b) size dispersion analysis with 49 data points for the anisole sample. Taken from Ref. [23].

diameter of the particles in this sample is approximately 2 nm. This work stated that it is very challenging to identify the type of zirconia phase using Rietveld refinements as all polymorph models provided reasonable agreements with experimental data. The PDF analyses also failed to identify a precise polymorph of ZrO_2 , in particular in the medium-range order region, where the PDF exhibits substantially broad peaks, encompassing none of the ZrO_2 polymorphs. However, in the short-range region ($r < 5 \text{ \AA}$), the PDF seems to be much more similar to the monoclinic phase as shown in Figure 1.20. The significant broadening of the experimental PDF peaks and its quick damping indicate a significant atomic positional disorder. Hence, the authors concluded that these ultrasmall particles are likely to have a local monoclinic structure and a quick loss of structural coherency.

In conclusion, this work suggests an overall tetragonal-like structure for the largest NPs, local monoclinic distortion, and a relatively high positional structural disorder for the smallest NPs.

1.5 Surface passivation of NP models

Most of material modelling schemes are based on the generation of structure models using some energy minimization procedure and checking of the quality of the models against experimental data. Such a powerful approach is routinely followed for the analysis of disordered systems (mostly glasses), by coupling for example molecular dynamics simulations and diffraction experiments [78]. Unfortunately, when modelling the structure of nanoparticles, things become much more complicated because of the following three reasons. First, real nanoparticles can hardly be considered as isolated objects in vacuum with pure stoichiometric chemical composition. This is inherent to the chemical (possibly physical) synthesis route used. Real nanoparticles may, for instance, be aggregated with an appreciable number of surface contacts between each other, or they may be almost isolated with grafted surfactant molecules at their surface, or they may be

polluted by impurities mostly located at the surface too. Second, as the structure of nanoparticles largely depends on their surface relaxation/reconstruction, any perturbations (as those stated above) of the surface environment may affect the nanoparticle structure. A good illustration has been recently given for the case of chalcogenide compounds, for which it has been shown that nanoparticles can undergo structural transformations, even reversible, in response to changes in the surface environment, rather than particle size [10]. Lastly, it is expected that these kind of surface stabilizing effects may be more or less pronounced depending on the nanoparticles chemical system and may be induced by even very small amount of impurities, not easy to characterize experimentally. Consequently, the way the real nanoparticles system differs from the “pure stoichiometric isolated” case and affects the structure is not trivial and not easy to anticipate, and this makes the establishment of nanoparticle models more complex.

Another problem concerns the calculation of electronic properties from non-passivated surface NP models. The presence of dangling bonds and other surface defects, as well as a too strong defect-induced surface reconstruction, generally lead to the presence of unrealistic defect energy states in the band gap and even lead to band gap closure. It is therefore essential to define an effective method of surface passivation in order to remove these band gap states (without introducing new artefacts). In what follows, we first illustrate in more detail the problems that arise when no surface passivation is envisaged for modelling NPs. We then present the main surface passivation procedures used to date.

In the work of Ponce *et. al.* [79], molecular dynamics simulations were conducted for SnO₂ nanoparticles of different sizes without surface passivation. The final models reveal pronounced structural reorganization and surface defects. In particular, it is observed that oxygen dimers and trimers form on the nanoparticle surface, as shown in Figure 1.22. Due to these high surface disorder and defects, the electronic properties get affected and produced defect states in the band gap, as shown in Figure 1.23. Looking to the Partial Density of States (PDOS) profile, defects attributable to surface dangling bonds are evident, particularly in proximity to the Fermi level and within the conduction band. These defects contribute to the closure of the band gap.

In the work of Puigdollers *et. al.* [80], electronic properties of zirconia nanoparticles models within the size range of 1.5 to 2 nm and without surface passivation were calculated with DFT methods at different level of theory (standard DFT functionals, the DFT+U approach, and hybrid functionals). The study considered octahedral-based morphologies as representative initial models for the NPs. A varying number of Zr surface atoms were removed to achieve stoichiometric systems. The resulting initial models, Zr₁₆O₃₂, Zr₄₀O₈₀, and Zr₈₀O₁₆₀, are shown in Figure 1.24. According to the authors of Ref. [80], structural relaxation led to large distortions, unable to maintain the initial tetragonal structure. An examination of the electronic structure calculated from

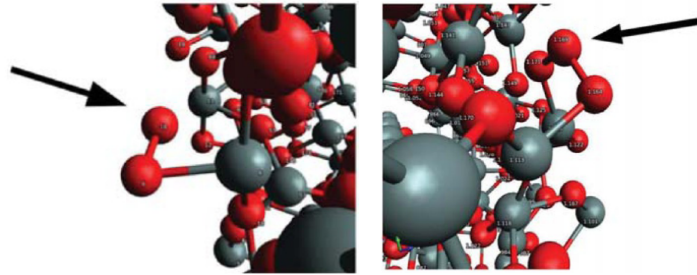


Figure 1.22: Surface oxygen atoms forming a (a) dimer and (b) trimer bonded together with Sn atoms. Taken from Ref. [79].

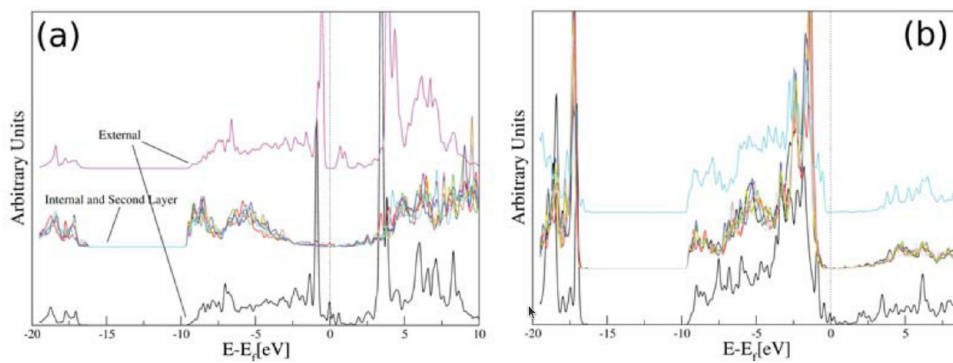


Figure 1.23: (a) PDOS of tin atoms and (b) PDOS of oxygen atoms. Taken from Ref. [79].

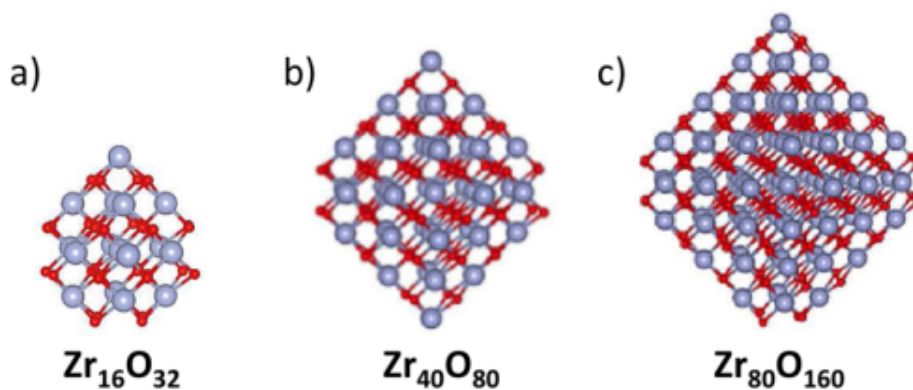


Figure 1.24: Models of partly truncated octahedral zirconia nanoparticles $(\text{ZrO}_2)_n$ created by removing (a) three Zr corner atoms from the $\text{Zr}_{19}\text{O}_{32}$ nanoparticle, (b) four Zr corner atoms from $\text{Zr}_{44}\text{O}_{80}$, and (c) five Zr corner atoms from $\text{Zr}_{85}\text{O}_{160}$. Zr is represented by big blue atoms and O by red small atoms. Taken from Ref. [80].

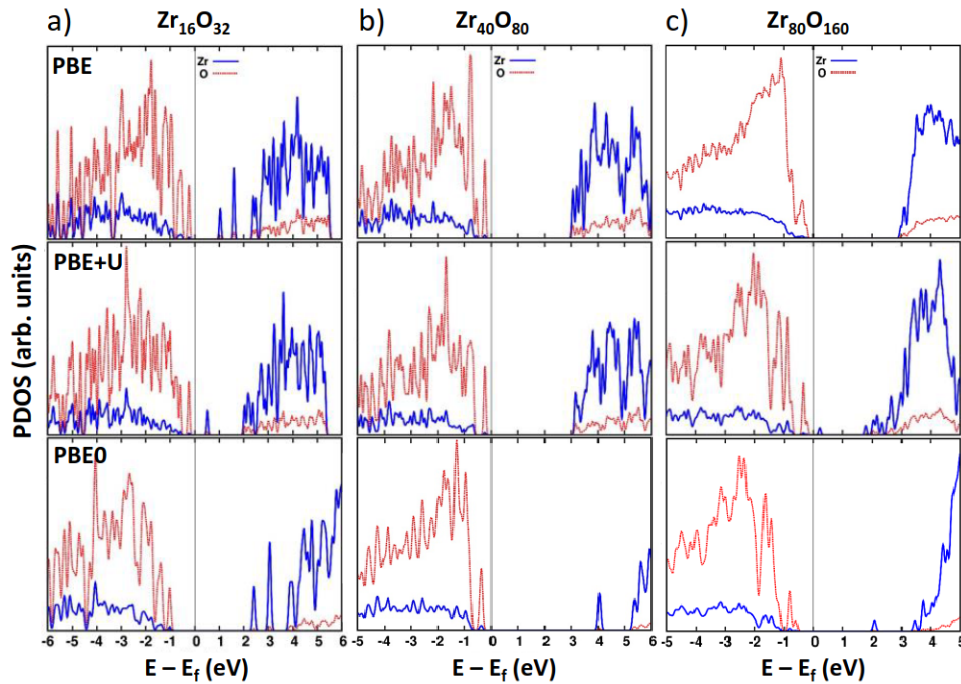


Figure 1.25: The Projected Density of States for nanoparticles $Zr_{16}O_{32}$, $Zr_{40}O_{80}$, and $Zr_{80}O_{160}$ are presented in (a), (b), and (c) respectively. These are obtained from PBE, PBE+U, and PBE0 calculations, arranged from top to bottom. The energy reference point corresponds to the Fermi level. Taken from Ref. [80].

the models is instructive. Figure 1.25 shows the PDOS plots calculated using the PBE, PBE+U and PBE0 functionals for the relaxed models. We notice defect states in the electronic structure, which are distinct from the valence (O sites) and conduction (Zr sites) bands. As a result, the band gap is reduced. Once again, this is due to the presence of poorly coordinated Zr and O atoms.

These examples highlight the importance of passivating the surface of NP models to avoid dangling bonds and the appearance of excessively under-coordinated atoms. We now describe the passivation methods.

The most used method to effectively passivate the dangling bonds of surface was introduced 20 years ago and is based on pseudo-hydrogen atoms model [81]. Pseudo-hydrogen atoms allow to pair the unbonded dangling bond electron with other electrons, by keeping the system locally neutral. They thus describe the essence of a good passivation agent and can serve as simplified models for the real passivation situations. In a tetrahedrally coordinated crystal, for example, if a surface atom has m valence electrons, that atom will provide $m/4$ electrons to each of its four bonds. To pair these $m/4$ electrons in each dangling bond, a passivating agent must provide $(8-m)/4$ additional electrons. For the system to remain locally neutral, there must be a positive nuclear charge $(8-m)/4$ nearby. Thus, the simplest passivation agent can be a hydrogen atom

with $(8-m)/4$ electrons and a nuclear charge $Z = (8-m)/4$. Depending on the type of nanoparticle, this generally results in hydrogen-like atoms with a non-integer nuclear charge Z , hence the term pseudo-hydrogen atom.

This methodology has been applied fairly recently to the study of SnO_2 quantum dots (QDs) [82]. In this work, the authors constructed a large bulk rutile SnO_2 structure and positioned a Sn atom at its center. They selected a sphere with a radius r (dependent on the quantum dot size) and eliminated all atoms located outside this sphere. They then removed surface Sn atoms with more than two dangling bonds and surface O atoms with more than one dangling bond. In rutile SnO_2 , each Sn atom is surrounded by six O atoms and possesses four valence electrons. Consequently, each Sn atom contributes four-sixths ($4/6 = 2/3$) of its electrons to each band. Given that hydrogen requires two electrons to complete its 1s shell, they opt for the pseudohydrogen ($^{4/3}\text{H}$) with $Z = 2 - 2/3$, or $4/3$, to saturate the Sn dangling bonds. Conversely, an O atom, surrounded by three Sn atoms, holds six valence electrons, aiming for a stable state with eight electrons to form a closed shell. Therefore, the pseudohydrogen ($^{2/3}\text{H}$) with $Z = (8 - 6)/3$, or $2/3$ is required, to neutralize the O dangling bonds. Figure 1.26 shows the passivation of the dangling bonds at the surface Sn and O atoms using $^{4/3}\text{H}$ and $^{2/3}\text{H}$, respectively.

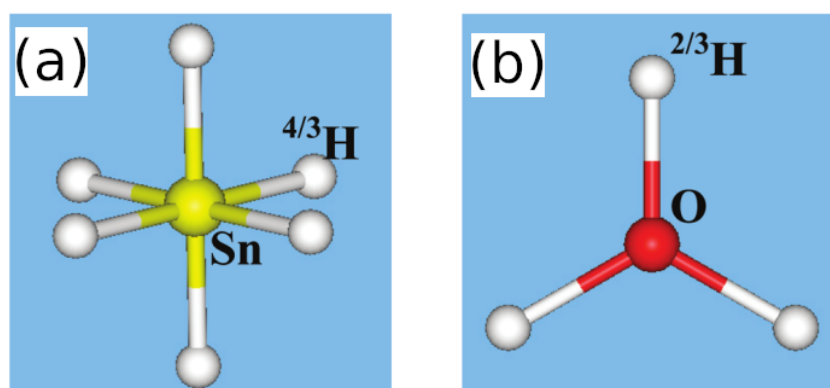


Figure 1.26: The schematic plots of (a) an octahedral Sn ($^{4/3}\text{H}$)₆ structure, and (b) a regular triangular O ($^{2/3}\text{H}$)₃ structure. The yellow, red, and white balls represent Sn, O, and pseudo-hydrogen atoms, respectively. Taken from Ref. [82].

In a more recent work carried out at IRCER on very small ZrO_2 [83] nanoparticles, a different approach based on the use of chemisorbed water molecules was used. In this study, the authors used ab-initio simulation techniques to examine how water molecules can stabilise the structure of NPs. The Car-Parrinello molecular dynamics method and conventional structure optimisation techniques were used to study cluster models with a diameter of about 1.25 nm, as shown in Figure 1.27. The PDFs calculated from the optimised structures, i.e. of lowest energy, structures without surface passivation, were found to be completely different from the experimental PDFs,

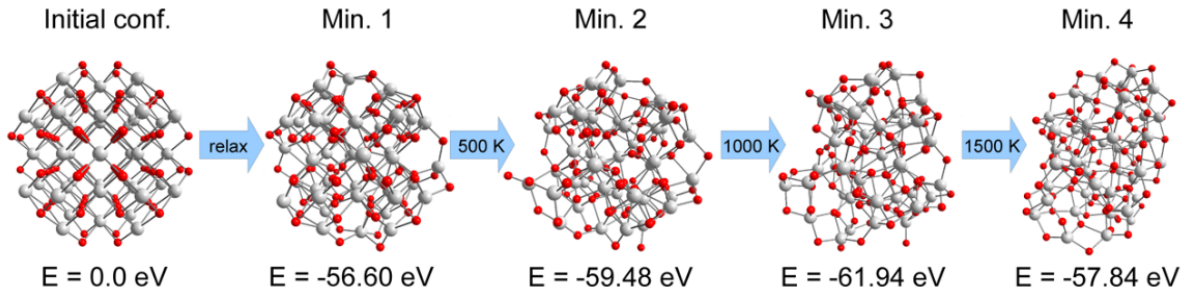


Figure 1.27: Initial cubic configuration and four configurations that are local minima of energy, for the $\text{Zr}_{43}\text{O}_{86}$ cluster without surface impurities, found with CP heating/cooling cycles. Below each cluster, the energy loss with respect to the initial configuration is shown. Taken from Ref. [83].

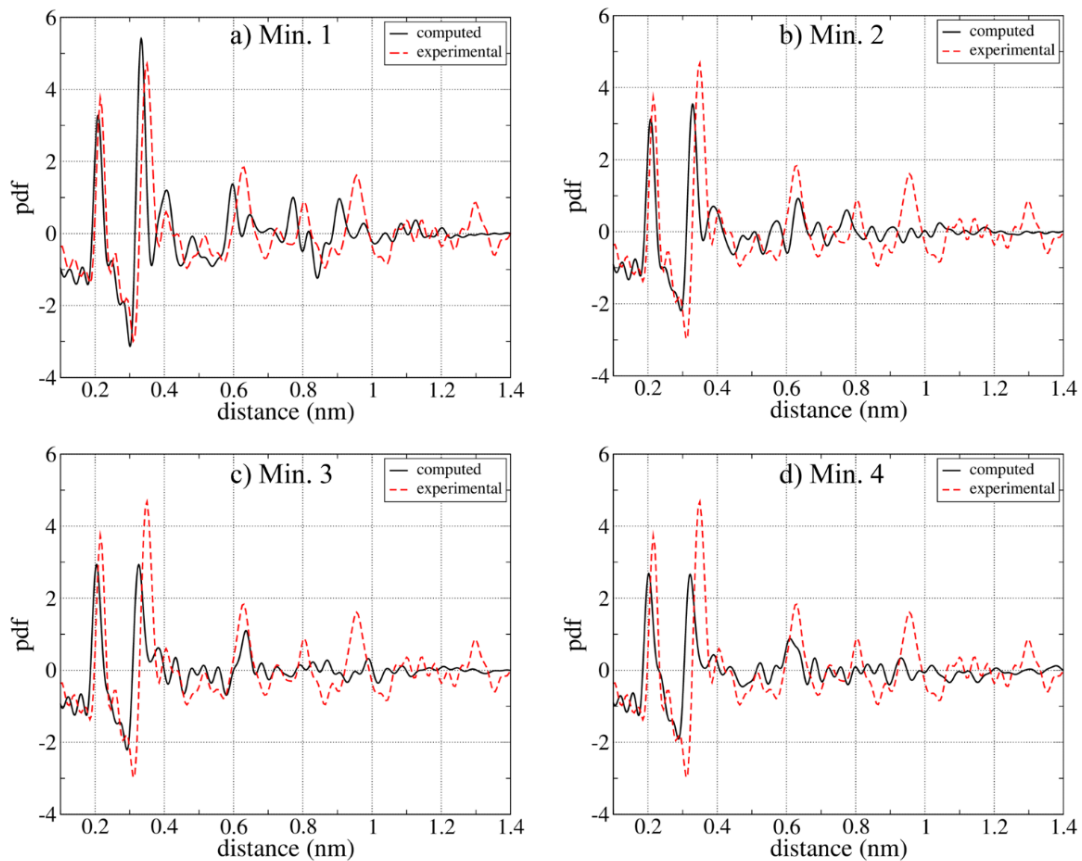


Figure 1.28: Comparing the experimental result with the PDFs computed from the four local energy minima observed for the unpassivated cluster: direct minimization from the starting perfect cubic crystal structure (a), and heating cooling cycles up to 500 K (b), 1000 K (c), and 1500 K (d). Taken from Ref. [83].

as shown in Figure 1.28. These results show that it is difficult to identify the best NP models based solely on energy minimisation and that a hypothetical sample of pure ZrO_2 nanoparticles in vacuum would probably have an amorphous structure, which is not the case in reality.

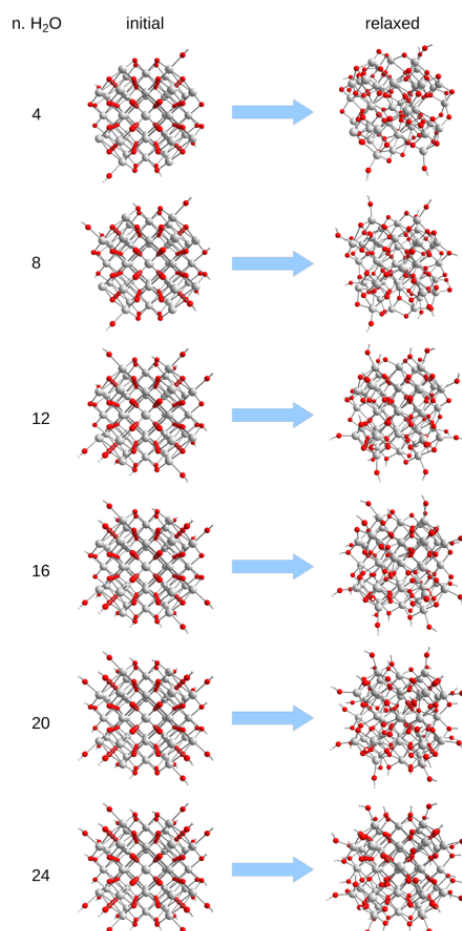


Figure 1.29: Initial and optimized configurations for clusters with dissociated H_2O impurities on the surface. Taken from Ref. [83].

The surface stabilization effect was explored by coating manually the particle surface with chemisorbed water molecules to varying degrees (15 % to 100 %). The introduction of dissociated water molecules, played a pivotal role in stabilizing the cluster structures. Even a minimal coverage of 4 H_2O molecules induced notable changes in the PDFs, with characteristics resembling experimental results. The study demonstrated that the stabilizing effect increases with coverage, and a fully covered cluster exhibited excessive stabilization, resembling a crystal-like structure, as shown in Figure 1.29. The comparison of computed PDFs with the experimental PDF from nanoparticles of comparable size showed good agreement when chemisorbed water were present, particularly at a surface coverage of around 80 % as depicted in Figure 1.30. This underscores the significance of accounting for the surface stabilization in models to accurately reflect the experimental ZrO_2 nanocrystal structures. The proposed model, featuring chemisorbed

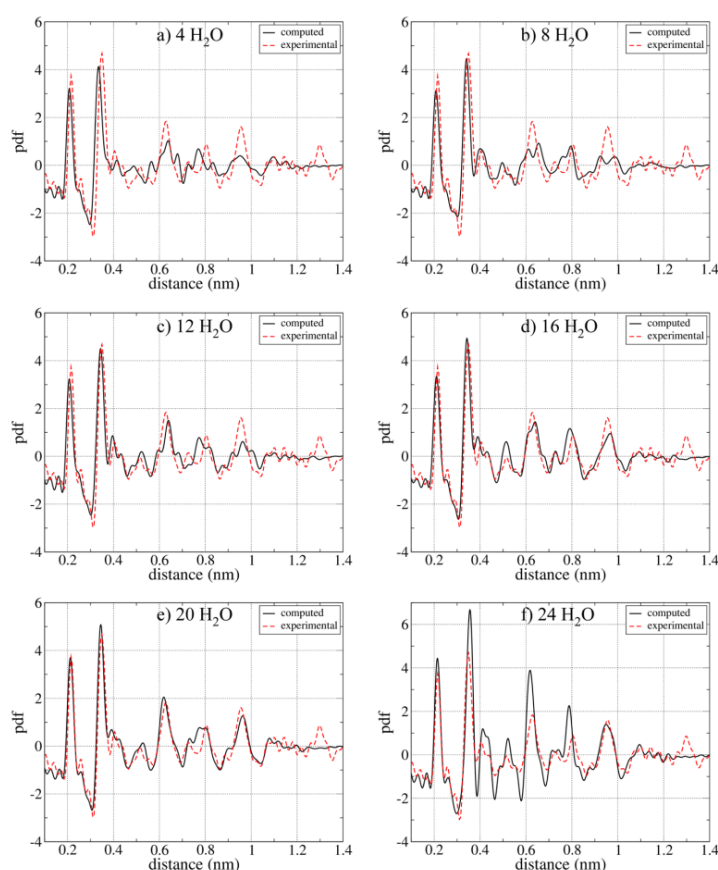


Figure 1.30: PDFs obtained from the optimized configurations with H₂O surface impurities: coverage with 4 (a), 8 (b), 12 (c), 16 (d), 20 (e), and 24 (f) water molecules. Taken from Ref. [83].

water molecules, emerged as an efficient and practical means of achieving structural stabilization, shedding light on the likely occurrence of such phenomena in real ZrO₂ systems.

In the present thesis work, instead of manually dissociating water molecules on given surface sites, we used a scheme that avoids prior knowledge of the required surface coverage (described in chapter 3).

1.6 The relation between band gap and nanoparticle size

Once models of NPs of different sizes have been produced, we can calculate the corresponding band gaps and obtain their evolution as a function of NP size. It is then essential to determine the relationship between the band gap and the size of the NP to better understand the quantum confinement effect present in the system under study. Generally, this is done by fitting the calculated data with theoretical or empirical models, which allows the key quantum confinement parameters to be extracted. Several theoretical models have been proposed to describe the

variation of band gap as a function of nanoparticle size. In an initial approach proposed by Brus [26], the photogenerated electron-hole pair is modeled using a Hamiltonian for a bound state within the effective mass approximation (EMA), considering an effective surrounding potential. By solving the Hamiltonian with the effective mass approximation, the energy yielding the band gap energy can be determined, as expressed below:

$$E_g = E_{g,bulk} + \frac{\hbar^2 \pi^2}{2R^2} \left(\frac{1}{m_e^*} + \frac{1}{m_h^*} \right) - \frac{1.8e^2}{\epsilon R} + \frac{e^2}{R} \sum_{n=1}^{\infty} \alpha_n \left(\frac{r_e + r_h}{R} \right)^{2n} \quad (1.1)$$

Here, $E_{g,bulk}$ represents the band gap of the bulk material. The second term denotes the increased kinetic energy resulting from the localization of the electron-hole pair within a sphere with radius R , scaling as R^{-2} . The third term represents the Coulomb attraction energy in a screened environment, scaling as R^{-1} . The fourth term is a polarization energy and exhibits the same scaling as the screened Coulomb attraction. This provides a physical rationale for a functional relationship between the band gap E_g in eV and the particle diameter d in nm, as described in Equation 1.2.

$$E_g = C_1 + \frac{C_2}{d} + \frac{C_3}{d^2} \quad (1.2)$$

In equation 1.2, the coefficients C_n need to be determined, which Brus found in the case of ZnO systems to be 3.37, -1.35, and 8.47. However, this model is noted to overestimate the band gap for particles size smaller than 5 nm [84] (see Figure 1.31). An alternative approach proposed by Viswanatha *et al.* [84] employs the tight binding (TB) approximation to calculate the size dependence of the band gap in ZnO systems. Additionally, it relates the band gap to experimentally determined particle sizes obtained from XRD data. While this analysis yields a better correlation to experimental data as shown in Figure 1.31, it sacrifices analyticity. The latter approach results in two expressions: Equation 1.3, which resembles the functional dependence of Brus but with variable exponents similar to the cluster size equations from Jortner [85], and equation 1.4, which provides a good fit to the data without any specific physical motivation for the functional dependence.

$$E_g = 3.35 + \frac{1.67}{d^{1.4}} \quad (1.3)$$

$$E_g = 3.35 + \frac{100}{18.1d^2 + 41.4d - 0.8} \quad (1.4)$$

Another approach to address the issue is a purely empirical one proposed by Meulenkamp *et al.* [86]. In their study, ZnO particle sizes were determined from XRD data and then compared to the wavelength corresponding to half the absorption of the first absorption maximum when transitioning from longer wavelengths. Although this value slightly differs from E_g , it

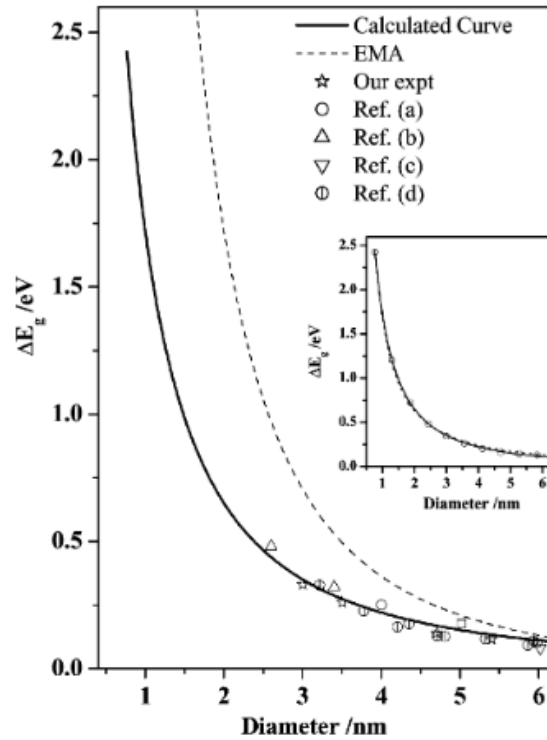


Figure 1.31: Comparison of the band gap variation in ZnO nanocrystals derived from the Tight-Binding (TB) approximation and its comparison with experimentally obtained data from various references. The dashed line represents the values obtained from the Effective Mass Approximation (EMA). The inset illustrates the fit to the calculated values. Taken from Ref. [84].

exhibits a similar functional dependence on particle size. The experimental data was fitted to the functional form of equation 1.2, yielding coefficients of 3.301, 1.09, and 294.

Equation 1.3 can be written in analytical form as:

$$E_g^{NP} = E_g^{bulk} + \frac{\beta}{d^\alpha} \quad (1.5)$$

$$\Delta E_g = \frac{\beta}{d^\alpha}$$

where, α and β are the fitting parameters, also called quantum confinement parameters and $\Delta E_g = E_g^{NP} - E_g^{bulk}$.

The equation mentioned above are a different way to fit the band gap. In the work of Jacobsson *et. al.* [87], the authors made a different fitting analysis in the case of ZnO systems and compared them, as shown in Figure 1.32 (a). As a result, the authors found that EMA gives the best fit of the band gap, as shown in figure 1.32 (b). The equation for the fit is given as below:

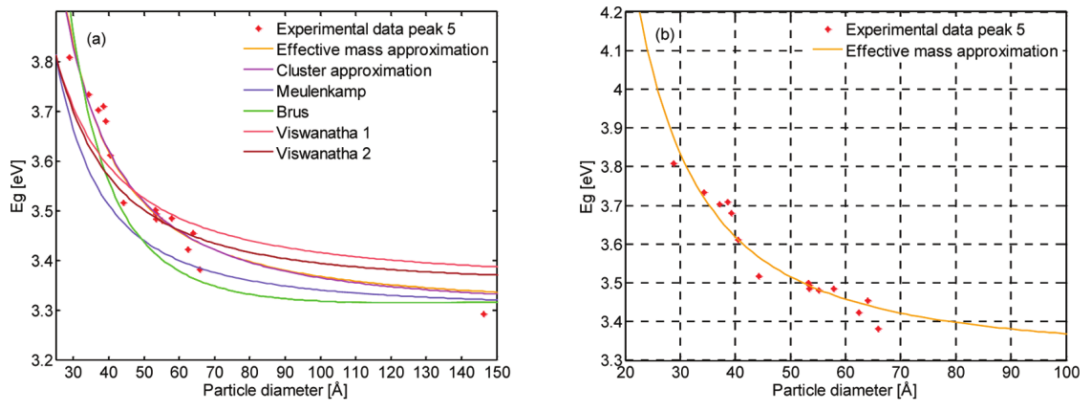


Figure 1.32: Band gap against ZnO particle sizes together with (a) expressions from the literature and, together with (b) the best fit using effective mass approximation. Taken from Ref. [87].

$$E_g = 3.30 + \frac{0.293}{d} + \frac{3.94}{d^2} \quad (1.6)$$

$$E_g = 3.30 + \frac{3.54}{d^{1.73}} \quad (1.7)$$

These two equations, equation 1.6 and equation 1.7 give more or less identical results.

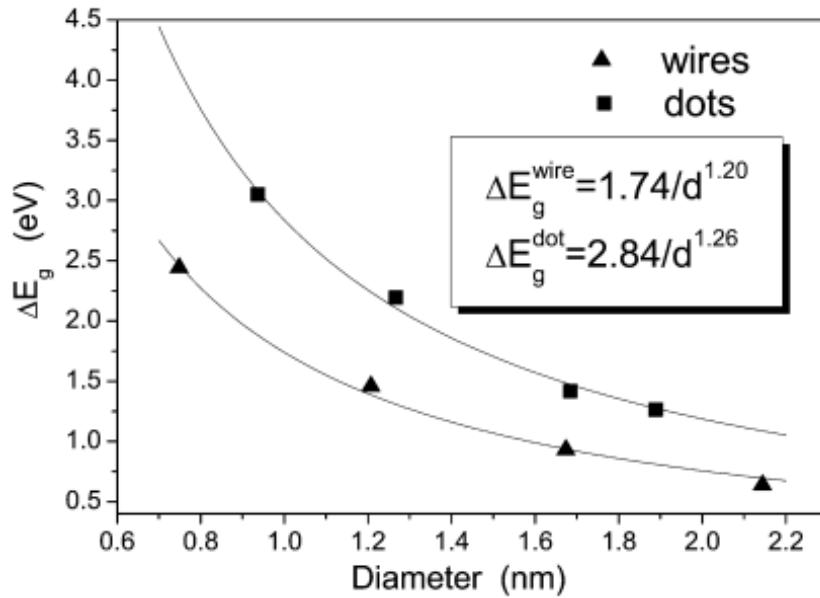


Figure 1.33: The calculated band gaps of different size SnO₂ QWs and QDs. The solid lines are the fitted curves. Taken from Ref. [82].

Among the various studies attempting to fit the band gap dependence on the NP size, equation 1.5

is frequently employed as it provides the most accurate fit for the band gap [8], [81], [82], [87]–[89]. In the work of Deng *et. al.* [82], the authors have used the equation 1.5 to fit the band gap in SnO₂ quantum dots (QDs) and quantum wires (QWs). The band gap increase follow the expressions $\Delta E_g^{wire} = 1.74/d^{1.20}$ for QWs and $\Delta E_g^{dot} = 2.84/d^{1.26}$ for QDs as shown in Figure 1.33. All of these studies reported in the above references have not explained the impact of quantum confinement parameter (α and β) on the strength of quantum confinement effect.

Therefore, we will adopt the same empirical formula (equation 1.5) to fit the calculated band gap in our studies.

1.7 Conclusions

In conclusion, this chapter highlights the overview of the historical background of nanomaterials, focusing particularly on the structural features of metal-oxide nanoparticles. We discuss the structure of the fluorite-derived zirconia polymorphs and cassiterite tin dioxide. Furthermore, we review the structural properties of "ultrasmall" nanoparticles based on previous studies. Through this discussion, we highlight the complexity of determining the structure of nanoparticles compared to bulk materials. Indeed, the synthesis of nanoparticles, especially with precise control, can be a sophisticated and intricate process. Achieving uniformity in size, shape, and surface properties is challenging. Additionally, nanoparticles may be prone to aggregation or changes in morphology over time, affecting the reproducibility and stability of the studied nanoparticles. It emphasizes that considering nanoparticles merely as small fragments of the bulk system is inadequate. The presented studies highlighted the impact of nanoparticle size on various properties, including optical, structural, and sensing behaviors. Nanoparticles exhibited distinct features, with variations in size influencing surface area, reactivity, and optical band gaps. Previous research lacked a precise understanding of nanoparticle structures, but recent investigations, particularly the work by Gambe *et. al.* [23], delve into the short-range and medium-range regions of nanoparticle structures. Previous theoretical investigations have highlighted the crucial role of surface stabilization, particularly through surface passivation, in generating accurate models of nanoparticle structures. The absence of surface passivation leads to deviations in the structure of ultrasmall nanoparticles from experimentally observed, thereby impacting their electronic properties. This deficiency introduces defects in both the valence and conduction bands, consequently reducing the width of the electronic band gap. Developing accurate models for nanomaterials, as seen in the work by Grena [83], involves inherent complexities. The dynamical behavior of nanoparticles, as well as the need to consider various factors like surface interactions, ligands, and solvent effects, adds a layer of complexity to the modeling process. This methodology provides insights into nanoparticle stabilization mechanisms. Lastly, we have discussed various empirical formulas aimed at fitting the evolution of the band gap with nanoparticle size. Among

these, empirical formulas derived from EMA model have consistently demonstrated the best fit for describing the electronic band gap evolution.



2

Atomic scale modelling

Summary

2.1	A quick overview of density functional theory	54
2.1.1	Many body problem	54
2.1.2	Born-Oppenheimer approximation	56
2.1.3	Density Functional Theory	57
2.1.4	Hohenberg-Kohn theorem	57
2.1.5	Kohn-Sham formalism	58
2.1.6	Exchange-Correlation Functionals	61
2.1.6.1	Local Density Approximation	62
2.1.6.2	Generalized Gradient Approximation	62
2.1.6.3	Hybrid Functional	63
2.1.7	Electronic wave functions basis-set	63
2.1.8	Pseudopotential approximation	64
2.2	Ab-initio Molecular Dynamics	66
2.2.1	Born-Oppenheimer molecular dynamics	66
2.2.2	Temperature control	66
2.2.2.1	Temperature in the NVE ensemble	66
2.2.2.2	Temperature in the NVT ensemble	67

2.3	Ab-initio principles for calculating electronic properties	69
2.3.1	Total and projected Density of states	69
2.4	CP2K code	71

2.1 A quick overview of density functional theory

Density Functional Theory (DFT) has become a powerful computational methodology in physics, chemistry and materials science. This approach provides a computational framework to investigate the electronic structure of materials. It was widely used for studying and predicting the properties of isolated molecules, solids, and material interfaces. It is based on the concept that the energy of a many-body interacting system, consisting of nuclei and electrons, can be effectively described in terms of its electronic density. The use of electronic density have, considerably, reduced the complexity of the mathematical resolution of the Schrödinger equation for the many-body system. DFT is not only a tool for theoretical understanding but also a practical approach for designing new materials. The DFT approach helps researchers to gain insights into the electronic properties of materials and make informed decisions during the material design process. In this chapter, we will introduce the key assumptions and fundamental theorems that form the basis of density functional theory.

2.1.1 Many body problem

The description of the electronic structure of an atom (molecule or solid) and the interactions between its components (see in Figure 2.1) play a critical role in determining its properties. In quantum mechanics (QM), the information about the system and how it evolves over time (a quantum state), is mathematically described using wave functions. Through the use of the Schrödinger equation (SE), quantum mechanical regime aids in estimating the electronic structure, density, and other properties of the atom.

The study of the electronic structure of a system made up of nuclei and electrons, requires to consider the kinetic energies of all the particles and also the potential energies describing their mutual coulombic interactions. In quantum chemistry, the kinetic and potential energies are linked to mathematical operators \hat{T} and \hat{V} . The sum of these operators is the Hamiltonian \hat{H} of the studied system. In this section, we will examine the general form of the SE in the case of a many-body system, and provide an overview of the methodology used to mathematically solve this equation. The general form of the time-independent SE equation is given by :

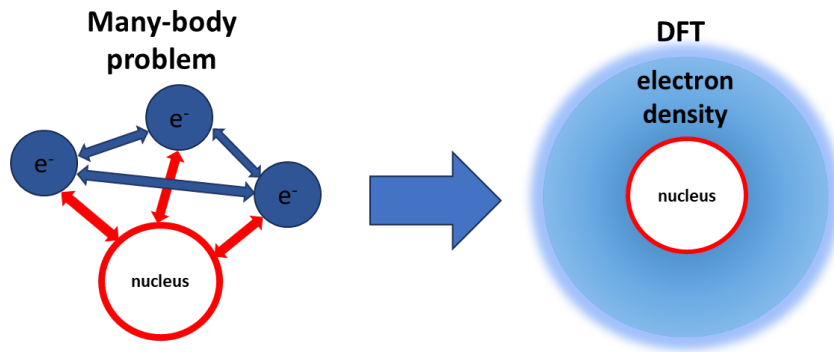


Figure 2.1: Schematic diagram for many-body interaction between electrons and nucleus.

$$\hat{H}\Psi(r, R) = E\Psi(r, R); \quad (2.1)$$

Where \hat{H} represent the Hamiltonian operator for a system with N nuclei and n electrons. Solving the above differential equation yields to both eigenvalues E_i and their corresponding eigenfunctions Ψ_i . The former corresponds to the permitted values for the total energy, and the latter are the many-body wave functions describing the studied system. The total Hamiltonian is written as:

$$\hat{H} = \hat{T} + \hat{V} = (\hat{T}_e + \hat{V}_{ee}) + (\hat{T}_N + \hat{V}_{N-N}) + \hat{V}_{e-N} \quad (2.2)$$

Where \hat{T} and \hat{V} are respectively the kinetic energy and potential energy operators. \hat{V}_{N-N} , \hat{V}_{e-N} and \hat{V}_{ee} are the potential energy operators related to the coloumbic nucleus-nucleus, electron-nucleus and electron-electron interactions, respectively. The mathematical formula of the different terms contributing to the Hamiltonian are written as:

$$\hat{T}_e = -\frac{\hbar^2}{2} \sum_i \frac{1}{m_i} \nabla_i^2 ; \quad \hat{V}_{e-e} = \frac{1}{2} \sum_{i,j} \frac{1}{4\pi\epsilon_0} \frac{e^2}{|r_i - r_j|} \quad (2.3)$$

$$\hat{T}_N = -\frac{\hbar^2}{2} \sum_a \frac{1}{M_a} \nabla_a^2 ; \quad \hat{V}_{N-N} = \frac{1}{2} \sum_{a,b} \frac{1}{4\pi\epsilon_0} \frac{Z_a Z_b e^2}{|R_a - R_b|} \quad (2.4)$$

$$\hat{V}_{e-N} = \sum_{i,a} \frac{1}{4\pi\epsilon_0} \frac{-Z_a e}{|r_i - R_a|} \quad (2.5)$$

Where the indexes a and b run on nuclei, i and j on electrons, M and m are the nucleus and electron masses, R and r are the position vectors of the nuclei and electrons, respectively.

2.1.2 Born-Oppenheimer approximation

This first approximation assumes the fact that the mass of a nucleus is much greater than that of an electron. In fact, the mass of a proton is about 1836 times greater than that of an electron. The existence of a Coulombic interaction between nuclei and electrons necessarily implies a correlation between their dynamics. Since a nucleus is much heavier than an electron, the relative speed of electrons is much higher than that of a nucleus. Consequently, electrons react instantaneously to the movement of their nuclei and immediately adapt to their new positions. In other words, electronic stationary states have time to relax before nuclei have moved enough to noticeably change the atomic environment. The movement of electrons can therefore be considered as independent of that of the nuclei, which are therefore assumed to be fixed. This decoupling of the motion of the electrons from that of the nuclei, introduced in the Born-Oppenheimer approximation [90], is considered as a first step in solving the Schrödinger equation. This approach allows us to write the wave functions of the many-body system as the product of a nuclear wave function and an electronic wave function. We therefore, try to solve the Schrödinger's equation for a system of fixed nuclei positions. This equation can be expressed (in atomic units) as follows:

$$\hat{H}\Psi(r_i) = E\Psi(r_i) \quad (2.6)$$

For a resulting fixed nuclei system, the electronic part of the Hamiltonian can be written as :

$$\hat{H}_e = -\frac{1}{2} \sum_i \nabla_i^2 + \frac{1}{2} \sum_{i,j} \frac{1}{|r_i - r_j|} - \sum_{i,a} \frac{Z_a}{|r_i - R_a|} \quad (2.7)$$

$$\hat{H}_e = \hat{T}_e + \hat{V}_{e-e} + \hat{V}_{e-N} \quad (2.8)$$

Thus, the time-independent SE can be expressed as:

$$\hat{H}_e \Psi_e(r_i, R_a) = E_e(R_a) \Psi_e(r_i, R_a) \quad (2.9)$$

Even when applying the BO approximation, solving the resulting Schrödinger equation remains a real complicated task. As mentioned above, the many-body system contains, generally, a very large number of interacting electrons. Analytically describing this system requires, to consider all mutual and simultaneous interactions between the electrons. This immediately presents a real mathematical challenge. The main difficulty is to consider all quantum mechanical effect, such as exchange, static and dynamic electron-electron and the difference between interacting and non-interacting kinetic energies. Thus, some approximations must be introduced to deal with these quantum effects. In the following sections we will give an overview of the DFT approach and the different approximations used to solve the Schrödinger equation.

2.1.3 Density Functional Theory

It was attempted to use electron density as the fundamental factor in the n electron problem. Since electron density solely depends on spatial coordinates, the task of solving a $3n$ -dimensional equation in 3-dimensions is now broken down into n independent 3-dimensional equations. It is described as the number of electrons in a certain volume. In DFT, we presume that there is no interaction between the electrons so the electron density is expressed as:

$$\rho(r) = \sum_i^N |\phi_i|^2 \quad (2.10)$$

Here, the electron density is represented by the non-interacting orbital ϕ_i rather than by ψ_i which is called the Kohn-Sham orbital. Total electron is calculated by summing the electron densities throughout the space:

$$\int_{space} \rho(r) dr = n \quad (2.11)$$

2.1.4 Hohenberg-Kohn theorem

The origins of density functional theory go back several decades ago to the famous paper by Hohenberg and Kohn published in 1964 [91]. The work proposed by Hohenberg and Kohn, was inspired by the Thomas-Fermi model, developed by Llewellyn Thomas and Enrico Fermi in 1927 [92], [93] and considering the density as a basic variable to solve the electronic structure of the many-body problem. Fortunately, Hohenberg and Kohn, succeeded in establishing a more rigorous theory which legitimised the intuitive idea introduced by Thomas and Fermi. They based their work on two fundamental theorems :

Theorem 1: Demonstrates that, for any system of interacting particles in an external potential $V_{ext}(r)$, the ground state potential is determined, to within a trivial constant, uniquely by the ground state particle density $\rho(r)$.

$$E = E[\rho(r)] \quad (2.12)$$

Theorem 2: A universal functional for the energy $E[\rho(r)]$ can be defined in terms of the electron density $\rho(r)$, for any external potential $V_{ext}(r)$, the exact ground state energy is the global minima value of this functional. Since, all observables such as kinetic energy, $V_{ext}(r)$ are uniquely determined if $\rho(r)$ is specified, they can be viewed as a functional of $\rho(r)$;

$$E_{HK}[\rho] = T[\rho] + V_{e-e}[\rho] + V_{e-N}[\rho] \quad (2.13)$$

$$E_{HK}[\rho] = F_{HK}[\rho] + \int \rho(r)V(r)dr \quad (2.14)$$

where $F_{HK}[\rho]$ is the universal Hohenberg-Kohn functional that represents the sum of kinetic and $e^- - e^-$ interaction energy. We use the second theorem in order to calculate the ground state energy by minimizing the above equation. The ground state energy is obtained by minimizing a function (\mathcal{L}) created by the Lagrange method of indeterminate multipliers.

$$\delta\{E_{HK}[\rho] - \mu[\int \rho(r)dr - n]\} = \delta\mathcal{L} = 0 \quad (2.15)$$

μ is the Lagrange multiplier. Now, Euler Lagrange equation gives:

$$\mu = \frac{\delta E_{HK}}{\delta n(r)} = V(r) + \frac{\delta F_{HK}[\rho(r)]}{\delta \rho(r)} \quad (2.16)$$

$V(r)$ is the external potential of the system. $F_{HK}[\rho(r)]$ is the so-called the Hohenberg-Kohn universal functional, and it operates independently of external potential. If we consider the exact form of the functional $F_{HK}[\rho(r)]$, we would be able to solve the Schrödinger equation exactly. Unfortunately, the explicit form of both $T[\rho]$ and $V_{e-e}[\rho]$ functionals remain unknown. A considerable effort has been devoted to attempting approximate representations of the functional $F_{HK}[\rho(r)]$.

2.1.5 Kohn-Sham formalism

A very efficient method based on the Hohenberg-Kohn theorems, which has been used with remarkable accuracy in calculating the electronic structure of solids, is the Kohn-Sham formalism. In order to provide a good approximation of the functional $F_{HK}[\rho(r)]$, Kohn and Sham (KS) proposed a fictitious system exactly like the real system in all respects other than the absence of electrons interactions. The fictitious non-interacting system (known as KS system), have the same density as the real system. Non-interacting electrons were assumed to be travelling in an effective potential V_{KS} (Kohn-Sham potential). The Hamiltonian of the non-interacting electrons KS system is devoid of energy due to $e - e$ interaction. Hence, the Hamiltonian is written as:

$$H_{KS} = \sum_i -\frac{1}{2}\nabla_i^2 + \sum_i V_{KS}(r_i) \quad (2.17)$$

The Kohn-Sham wavefunction is a single Slater determinant constructed from a set of orbitals that are the lowest-energy solutions to:

$$\left[-\frac{1}{2}\nabla^2 + V_{KS}(r) \right] \phi_i(r) = \epsilon_i \phi_i(r) \quad (2.18)$$

Here ϵ_i is the orbital energy of the corresponding Kohn-Sham orbital ϕ_i .

By using equation 2.18, kinetic energy in the KS system can be written as:

$$T_{KS} = \sum_i^n \int \phi_i^*(r) \left(-\frac{1}{2} \nabla^2 \right) \phi_i(r) dr \quad (2.19)$$

And a charge density in the KS system using single orbital can be written as:

$$\rho_{KS} = \sum_i^n \phi_i^*(r) \phi_i(r) \quad (2.20)$$

Hence, the energy functional for non-interacting electron in a KS system is given as:

$$E[\rho_{KS}] = T_{KS}[\rho_{KS}] + \int V_{KS}(r) \rho_{KS}(r) dr \quad (2.21)$$

The aforementioned equation needs to be minimized with respect to electron density in order to obtain the ground state energy. This can be accomplished by reducing a functional and applying the Lagrange method of unknown multipliers.

$$\mathcal{L}[\rho_{KS}] = T_{KS}[\rho_{KS}] + \int V_{KS}(r) \rho_{KS}(r) dr - \mu \left[\int \rho_{KS}(r) - n \right] \quad (2.22)$$

As μ is a Lagrange multiplier and the functional minimization $\delta \mathcal{L}[\rho_{KS}] = 0$, the Euler-Lagrange multiplier is expressed as:

$$\mu = V_{KS}(r) + \frac{\delta T_{KS}[\rho_{KS}]}{\delta \rho_{KS}(r)} \quad (2.23)$$

We are aware that an interacting system has distinct properties than a non-interacting system. In the next step, let's try to connect the two i.e;

$$T[\rho] = T_{KS}[\rho] + (T[\rho] - T_{KS}[\rho]) \quad (2.24)$$

The term enclosed in brackets signifies the deviation in kinetic energy between the two systems. Similar to how charge energy distribution is represented, exchange energy and correlation energy are each represented by a classical and non-classical term, the $e^- - e^-$ interaction energy for an interacting system is described as a total of these terms.

$$V_{ee} = J_{ee}[\rho] + (V_{ee}[\rho] - J_{ee}[\rho]) \quad (2.25)$$

And, J_{ee} is calculated as:

$$J_{ee}[\rho] = \frac{1}{2} \iint \frac{\rho(r_1)\rho(r_2)}{|r_1 - r_2|} dr_1 dr_2 \quad (2.26)$$

So, the energy function for interacting system in the form of KS system is expressed as:

$$\begin{aligned} E[\rho] &= T_{KS}[\rho] + J_{ee}[\rho] + \int \rho(r)V(r)dr + (T[\rho] - T_{KS}[\rho] + V_{ee}[\rho] - J_{ee}[\rho]) \\ &= T_{KS}[\rho] + J_{ee}[\rho] + \int \rho(r)V(r)dr + E_{XC}[\rho] \end{aligned} \quad (2.27)$$

Two components make up the E_{XC} exchange-correlation functional : (i) the difference in kinetic energy between interacting and non-interacting systems; and (ii) the non-continuum component resulting from $e^- - e^-$ interaction. The exact analytical formula for this functional is still unknown. Thus, the expected accuracy in solving the electronic structure problem is closely related to the choice of the exchange correlation functional.

Similarly, in order to get ground state energy, the functional $E[\rho]$ should be minimized. By using the Lagrange undetermined multiplier scheme to get the Euler-Lagrange equation as follows:

$$\mu = V_{eff} + \frac{\delta T_{KS}[\rho]}{\delta \rho(r)} \quad (2.28)$$

$$\begin{aligned} \text{where, } V_{eff} &= V(r) + \frac{\delta J_{ee}[\rho]}{\delta \rho(r)} + \frac{\delta E_{XC}[\rho]}{\delta \rho(r)} \\ &= V(r) + \int \frac{\rho(r')}{|r - r'|} dr' + V_{XC}(r) \\ &= V(r) + V_H(r) + V_{XC}(r) \end{aligned} \quad (2.29)$$

Here, $V(r)$ stands for the nuclei potential, $V_H(r)$ for the Hartree potential resulting from the distribution of electron charge, and $V_{XC}(r)$ potential is obtained by derivating the exchange correlation energy. Therefore, by simply changing V_{KS} to V_{eff} , it is possible to calculate the ground state real system's density. The electron density is then extracted from the N single electron orbitals $\phi_i(r)$ obtained by solving a set of N mono-electronic Schrödinger Equations called Kohn-Sham equations written as :

$$\left[-\frac{1}{2}\nabla^2 + V_{eff}\right]\phi_i(r) = E_i\phi_i(r) \quad (2.30)$$

A self-consistent iterative numerical method is used to solve the Kohn-Sham equations. The

flowchart in Figure 2.2 describes the workflow of the Kohn-Sham method.

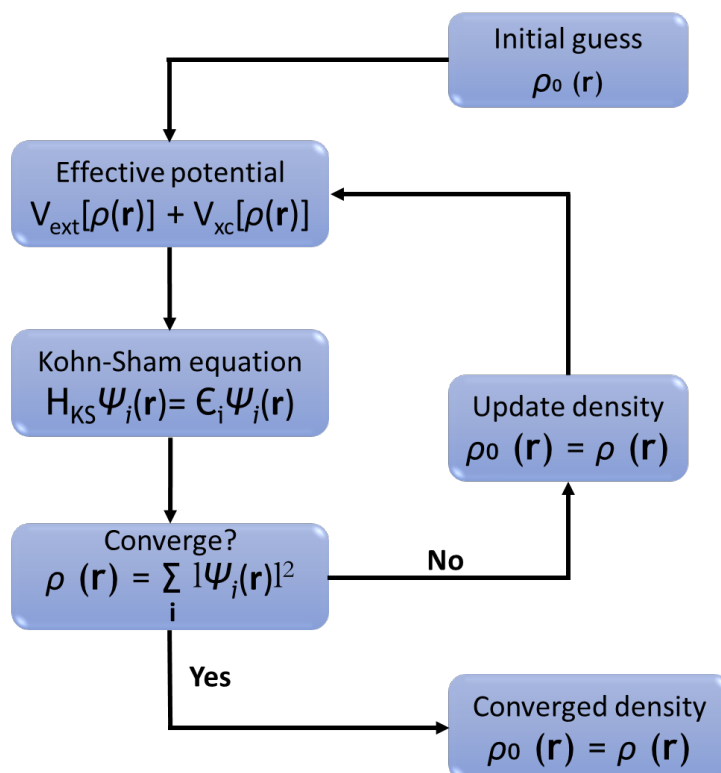


Figure 2.2: Flowchart representation of solving the Kohn-Sham equations.

The final output energy is then derived to calculate the forces acting on the nuclei using the Hellmann-Feynman theorem [94]. Considering the calculated forces, specific algorithms are used to propagate the nuclei over space and time to perform geometry optimisation, Molecular Dynamics (MD), etc.

2.1.6 Exchange-Correlation Functionals

As mentioned in eq. (2.27), the functional energy $E[\rho]$ described in the Kohn-Sham scheme, contains an exchange correlation term $E_{XC}[\rho]$ whose exact form is unknown. Although, this energy value is too low relative to the overall energy, but it plays a crucial role in determining the ground state features. It can be assumed that the main task of the Kohn-Sham DFT method is to find the optimal form of the exchange-correlation energy that accurately describes the studied system. Two exchange-correlation functionals have been widely used in DFT calculations in solid state physics and materials chemistry. In the next sections, we provide an introduction to a few of the most prevalent $E_{XC}[\rho]$ functionals.

2.1.6.1 Local Density Approximation

In the local density approximation (LDA), the fluctuating electron density is dealt with by partitioning the inhomogeneous electron region into several small regions, and viewing each of these small regions as a homogeneous electron gas. In other terms, the electron density is considered as locally uniform. The exchange-correlation functional of the nonuniform electron gas is then obtained by considering the exchange-correlation energy of each electron in a uniform density electron gas.

$$E_{XC}^{LDA}[\rho(r)] = \int \rho(r) \varepsilon_{XC}^{HEG}[\rho(r)] dr \quad (2.31)$$

Where, $\varepsilon_{XC}^{HEG}[\rho(r)]$ refers to XC energy possessed by an electron in a homogeneous electron gas (HEG) in terms of its density $\rho(r)$. A HEG is described as a system made up of electrons interacting in response to a uniform positive background charge of fixed density $\rho(r)$ for all values of r . The aforementioned equation can be adapted to take account of electron spin component, and the resulting approximation is now known as the local spin density approximation (LSDA).

$$E_{XC}^{LDA}[\rho \downarrow (r), \rho \uparrow (r)] = \int \rho(r) \varepsilon_{XC}^{HEG}[\rho \downarrow (r), \rho \uparrow (r)] dr \quad (2.32)$$

According to literature, this approach has led to fairly good accuracy in its outcomes. However, there are some negative aspects to it:

- It usually underestimates lattice parameters [95], [96]
- It underestimates the exchange energy and overestimate the correlation energy [97], [98]
- Does not produce accurate results for materials having hydrogen bonds [99].

2.1.6.2 Generalized Gradient Approximation

Real systems often showcase varying densities and lack homogeneity. The concept of a uniform density across real space, as assumed by LDA, is deemed non-physical. This is because it is plausible to have a higher electron density closer to the nucleus than in a more distant region. Therefore, the Generalized Gradient Approximation (GGA) addresses this limitation by considering both the electron density (ρ) and its gradient effects to improve the E_{XC} functional approximation. Consequently, GGA tends to yield more accurate results compared to LDA. The expression for the GGA exchange-correlation functional is given by:

$$E_{XC}^{GGA}[\rho, \nabla \rho] = \int \rho(r) \varepsilon_{XC}^{GGA}[\rho, \nabla \rho] dr, \quad (2.33)$$

A number of different GGA functionals have been proposed for the exchange and correlation energies. We can list, Lee, Yang and Par's (LYP) correlation functional [100] and Becke's (B88)

exchange functional [101], as well as Perdew and Wang's (PW91) [102] and Perdew, Burke and Ernzerhof (PBE) exchange-correlation functionals [103].

2.1.6.3 Hybrid Functional

For semiconductors and insulators, the band structure DFT calculations using LDA and GGA exchange correlation potentials demonstrated that the band structure given by KS eigenvalues yields too small gaps [104]. These inaccuracies can significantly impact the positions of both the conduction and valence bands, resulting in transition energy errors comparable to the magnitude of the band-gap error [104]. To address these limitations, several hybrid functionals including Becke3 Lee–Yang–Parr (B3LYP) [105], [106], Heyd–Scuseria–Ernzerhof (HSE) [107], and PBE0 [108], [109] have been developed to align the electronic structure more closely with experimental values. In our study, we employed the PBE0 functional to achieve electronic properties that closely match experimental references. The PBE0 functional is characterized by incorporating 75% of PBE exchange energy, 25% of Hartree-Fock exchange energy, and the full PBE correlation energy. Its formula is as follows:

$$E_{XC}^{PBE0} = 0.75E_X^{PBE} + 0.25E_X^{HF} + E_C^{PBE} \quad (2.34)$$

2.1.7 Electronic wave functions basis-set

The next step in solving the Kohn-Sham equations (2.18) involves the selection of a basis set to expand the electronic wave functions. In this context, the wave function is represented as a vector within the chosen basis set, with the components of this vector corresponding to the coefficients of the basis functions in the linear expansion.

From a mathematical point of view, a basis set is a collection of vectors that spans a space. For example, the i , j , and k Cartesian unit vectors form a basis set that spans three-dimensional (3D) Cartesian space. In quantum chemistry, the term "basis set" refers to the collection of one-particle functions utilized in methods like the Linear Combination of Atomic Orbitals (LCAO) to construct molecular orbitals.

Unlike in mathematics, the basis set in quantum chemistry, which focuses on an atom determining a single-electron atomic orbital, may not necessarily be orthogonal. There are two well-known types of basis sets commonly used: Slater Type Orbital (STO) and Gaussian Type Orbital (GTO). Both of these basis sets play a crucial role in quantum chemistry calculations. STO can be expressed as:

$$\phi_{abc}^{STO}(x, y, z) = Nx^a y^b z^c e^{-\zeta r}, \quad (2.35)$$

In this equation, N represents a normalization constant, while x , y , and z denote the Cartesian coordinates. ζ indicates the strength of single electron function localization, whereas a , b , and c regulate the angular momentum L , under the constraint $L = a + b + c$. Similarly, the GTO is defined in the same fashion to that of STO, except for the difference that the exponential term is quadratic in radial distance, described as:

$$\phi_{abc}^{GTO}(x, y, z) = Nx^a y^b z^c e^{-\zeta r^2} \quad (2.36)$$

Constructing basis functions in this manner offers the advantage of enabling quick Gaussian integrals and leveraging techniques such as the product of two Gaussians, which simplifies computations significantly. However, a drawback of these functions is their inability to precisely capture short and long-range orders. To address this challenge while still utilizing Gaussian methodologies, one can employ a linear combination of GTOs to create a function that emulates STOs. This approach is known as Contracted Gaussian Type Orbital (CGTO), and it is expressed as follows:

$$\phi_{abc}^{CGTO}(x, y, z) = N \sum_i^n c_i x^a y^b z^c e^{-\zeta_i r^2}, \quad (2.37)$$

where, n denotes the number of GTOs in the linear combination.

To enhance the accuracy of approximating the wave function, the previously explained orbitals can undergo linear contraction. Linear contraction involves reducing the number of orbitals in various ways, including:

- Minimal basis set
- Double-Zeta (DZ) basis set
- Triple-Zeta (TZ) basis set

2.1.8 Pseudopotential approximation

The solution of the Kohn-Sham equation requires to consider both core and valence electrons, and when constructing the external potential (V_{ext}) using the entire Coulomb potential, the computational cost becomes prohibitively high. This is primarily due to the rapid oscillation of the valence wave functions in the core region, due to the strong potential and the orthogonality requirements across states, necessitating the use of a large basis set.

To address this computational challenge, a pragmatic approach is to treat the inner electrons as inert, positing that only the valence electrons actively participate in bonding. In this approach, the effective full potential term in the Schrödinger equation, serving as a means to account for the intricate effects arising from the motion of the core electrons and the nucleus, is effectively replaced by a pseudopotential. Thus, the pseudopotential (V_{pseudo}) effectively accounts for

the frozen core electrons and nucleus. Pseudopotentials are required to correctly represent the long range interactions of the core and to produce pseudowavefunction that exhibits slower fluctuations (smooth functions) in the core region. Therefore, fewer basis functions are required to expand the smooth valence pseudowavefunctions, reducing significantly the computational cost. This method allows for a more efficient representation of the electronic structure while maintaining accuracy in the description of chemical bonding and properties.

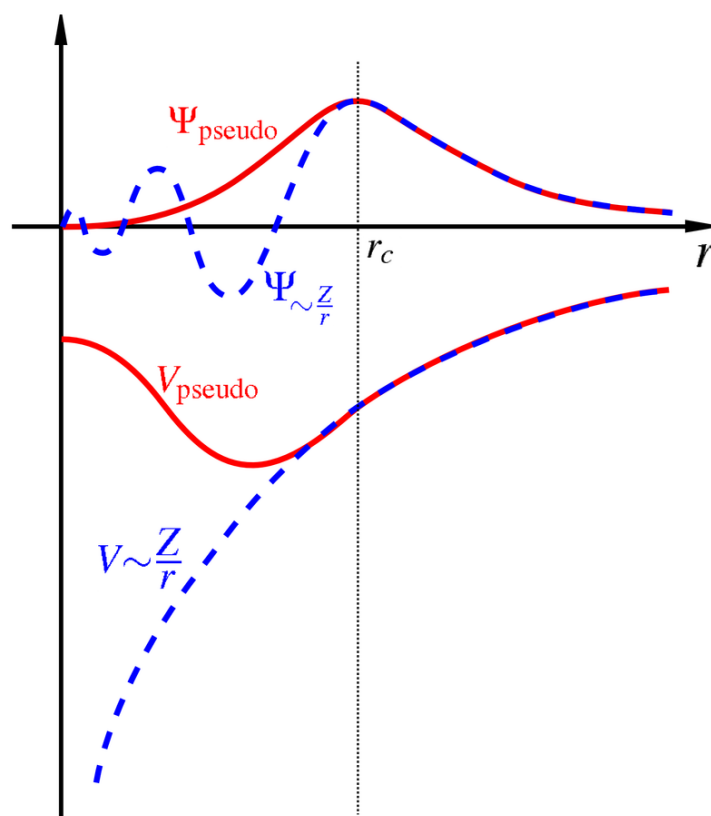


Figure 2.3: Schematic depiction of the pseudopotential (solid lines) and all-electron potential (dashed lines), together with the corresponding wave-functions. The radius value at which both potentials exhibit identical behavior is shown by the vertical line r_c . Taken from Ref. [110].

A crucial aspect of pseudopotential design is ensuring their precise correspondence to the real Coulomb potential in the valence region (refer to Figure 2.3). This meticulous design guarantees that the charge density generated in the valence region accurately reflects the real charge density of the system. Consequently, this approach streamlines computational calculations by reducing the complexity associated with modeling the intricate behavior of core electrons, while retaining accuracy in describing the behavior of valence electrons—often the primary contributors to chemical bonding and reactivity.

2.2 Ab-initio Molecular Dynamics

To investigate the behavior of atoms and molecules under specific thermodynamic conditions, researchers often utilize molecular dynamics as a computational method. Ab-initio molecular dynamics (AIMD) specifically attempts to approximate the solution to the electronic Schrödinger equation to derive an effective potential for the studied system. This potential is subsequently employed to compute forces acting on the nuclei. The resulting information is used to apply Newton's equations of motion and to determine the velocities of the atoms. Through the numerical solution of Newton's equations, MD simulations aim to delineate the trajectory of each particle.

2.2.1 Born-Oppenheimer molecular dynamics

Born-Oppenheimer Molecular Dynamics (BOMD) is based on the adiabatic Born-Oppenheimer approximation described in section 2.1.2. The main idea is to combine both quantum electronic structure calculations and Newton classical dynamics to solve the equations of motion. It consists in solving the time independent Schrödinger equation using DFT, considering a set of fixed nuclear positions, at each molecular dynamics step. In that way, the time-dependence of the electronic structure results from the nuclear dynamic. Therefore, the resulting Born-Oppenheimer molecular dynamics approach is characterized by:

$$M_I \ddot{\mathbf{R}}_I(t) = -\nabla_I \min_{\psi_0} \{ \langle \psi_0 | \hat{H}_e | \psi_0 \rangle \}, \quad (2.38)$$

for molecular dynamics considering the time independent Schrödinger equation :

$$\hat{H}_e \psi_0 = E_0 \psi_0 \quad (2.39)$$

for the electronic ground state. where, $\ddot{\mathbf{R}}_I$ is the acceleration of the nucleus I and M_I represents its mass. Here the nuclei are supposed to be classical point particles. The minimum of \hat{H}_e have to be reached in each molecular dynamics step.

2.2.2 Temperature control

2.2.2.1 Temperature in the NVE ensemble

The microcanonical ensemble, often denoted as NVE (constant Number of particles, Volume, and Energy), is a statistical ensemble in which the number of particles and their total energy remain constant. In the microcanonical ensemble, the system is considered isolated, meaning that it cannot exchange particles or energy with its surroundings. As a result, the system's total

energy is conserved over time. The temperature (T) in the microcanonical ensemble is related to the kinetic energy of the particles through their momenta given as:

$$\sum_{i=1}^N \frac{|P_i|^2}{2m_i} = \frac{k_B T}{2} (3N - k) \quad (2.40)$$

where, k_B and k are the Boltzmann constant and number of constraints, respectively. The average of this temperature ($\langle T \rangle$) gives similar values to the macroscopic temperature.

2.2.2.2 Temperature in the NVT ensemble

In many real-world applications, the conditions under which experiments are conducted often do not align with the assumptions of the microcanonical ensemble. For practical purposes, the NVT ensemble, which involves molecular dynamics simulations with a thermostat, is a more suitable approach for studying system properties at a specific temperature.

The NVT ensemble, also referred to as the canonical ensemble, is specifically designed to maintain constant values for the number of particles (N), volume (V), and temperature (T). This ensemble comprises multiple nearly independent assemblies, separated by stiff, impermeable, but conducting walls. While the number of particles and volume remain fixed, energy exchange is allowed between the assemblies, facilitating the attainment of a common temperature. This ensemble proves particularly useful for studying systems under well-defined temperature conditions. It accurately represents scenarios where a system is in thermal contact with a heat reservoir, facilitating energy exchange while keeping the particle number and volume constant.

Nosé–Hoover thermostat

The Nosé–Hoover thermostat stands as a deterministic algorithm employed in constant-temperature molecular dynamics simulations. Initially developed by Nosé and subsequently refined by Hoover [111]–[113], this thermostat, despite its heat bath comprising only one imaginary particle, successfully maintains realistic constant-temperature conditions (canonical ensemble) during AIMD. As a result of its accuracy and efficiency, the Nosé–Hoover thermostat has become a widely adopted and reliable method for constant-temperature molecular dynamics simulations. Let's consider a system comprising N particles with coordinates r_i , momenta p_i , masses m_i , and potential energy $E(r)$ (DFT energy). Additionally, we introduce extra degrees of freedom with artificial variables s , velocity \dot{s} , and an associated effective mass $Q > 0$. The magnitude of Q governs the coupling between the heat bath and the actual system, thereby regulating

the temperature. In this context, we also introduce virtual variables (r'_i, p'_i, t') , establishing a connection with the real system $(r_i, p_i, \text{ and } t)$ through the relationship:

$$dt' = sdt; \quad r'_i = r_i; \quad s' = s; \quad p'_i = sp_i \quad (2.41)$$

As the atomic coordinates remain unaltered in the extended coordinates, the artificial coordinate s can be perceived as functioning as a time-scaling parameter. It effectively extends the timescale in the extended system by an s factor (refer to Ref. [114]). The transformation of velocities is expressed as:

$$\dot{r}_i = \frac{dr_i}{dt} = s \frac{dr'_i}{dt'} = s\dot{r}'_i \quad (2.42)$$

The Lagrangian \mathcal{L} for the extended system, in accordance with equations 2.41 and 2.42, is selected to be:

$$\mathcal{L} = \sum_i^N \frac{m_i}{2} s^2 \dot{r}'_i{}^2 - E(r') + \frac{Q}{2} \dot{s}^2 - Nk_B T \ln(s) \quad (2.43)$$

The initial two terms in the above equation signify the kinetic and potential energy of the real system. The subsequent two terms represent the kinetic energy of s and the potential energy, which is tailored to ensure that the formalism yields the canonical ensemble. This formulation results in the following equations of motion:

$$\dot{r}'_i = \frac{F'_i}{m_i s^2} - \frac{2\dot{s}r'_i}{s}, \quad (2.44)$$

$$\dot{s} = \frac{1}{Q_s} \left(\sum_i^N m_i s^2 \dot{r}'_i{}^2 - gk_B T_0 \right) \quad (2.45)$$

In the given equations, T_0 represents the target temperature. These equations describe the micro-canonical ensemble of the extended system. However, it is important to note that the energy of the real system is not constant, given the continuous exchange of heat between the heat bath and the real system, aimed at maintaining the temperature of the real system.

The choice of Q in the Nosé-Hoover formalism is critical. A careful selection is necessary because, with $Q \rightarrow \infty$, achieving canonical sampling may take an extended period due to the prolonged energy transfer time. On the other hand, when $Q \rightarrow 0$, there is a risk of unrealistic, high-frequency temperature fluctuations.

2.3 Ab-initio principles for calculating electronic properties

Electronic properties encompass a broad array of parameters and representations that thoroughly describe the state and dynamics of electrons within a given material. A notable example is the electronic band structure [115], where electron states are depicted based on their energy E and momentum (k).

The phenomenon of quantum confinement occurs when electrons are confined to nanoscale dimensions in one or more spatial directions, leading to a notable alteration of the electron density of states [116]. The conventional “electron-in-a-box” model provides a qualitative understanding of the phenomenon. In such a system, discrete electronic states emerge at distinct energies, and as quantum confinement intensifies (i.e., the size of the box decreases), the gap between these states widens. The specifics of this discretization depend on the degree to which spatial directions are constrained. The observed behavior of nanostructures has significant implications for their properties. For instance, in terms of electronic characteristics, an increased gap between electronic states can lead to transitions from metal to semiconductor or from semiconductor to insulator. Alongside quantum confinement, the scattering of electrons at surfaces and interfaces is a noteworthy phenomenon that profoundly influences electrical and thermal conductivity in nanoparticles.

2.3.1 Total and projected Density of states

In the fields of solid-state physics and condensed matter physics, the density of states DOS represents the count of distinct electron states permissible at a specific energy level, denoting the number of electron states within a given volume per unit energy. Calculations of DOS enable the assessment of the overall state distribution relative to energy and can ascertain the intervals between energy bands in semiconductors. The concept of density of states can be expressed as follows: $D(E) = \frac{N(E)}{V}$, where $D(E) \delta E$ represents the count of states within a volume V that have energies ranging from E to $E + \delta E$. The mathematical representation of the system is conveyed through a probability density function that characterizes the distribution. This distribution is typically obtained by averaging over the space and time domains, encompassing the numerous states held by the system. The relationship between the density of states and the dispersion relations of the system’s attributes is straightforward. A high density of states at a given energy level implies a significant number of available states.

When examining the density of states for electrons positioned at the boundary between the valence and conduction bands within a semiconductor, it becomes apparent that an increase in electron energy corresponds to a greater availability of states for electron occupation within the conduction band. In contrast, the density of states exhibits a discontinuity over a specific

energy range, leading to the absence of accessible electron states within the material's band gap. Furthermore, for an electron situated at the conduction band edge to transition to a different state within the valence band, a minimum amount of energy equivalent to the material's band gap must be released.

The calculation of the density of states in quantum mechanical systems is contingent upon the particular system being studied. For entities such as electrons, photons, or phonons, the density of states can be computed and represented as a function of either energy (E) or wave vector k . To establish a connection between the density of states as a function of energy and the DOS as a function of wave vector, one must have knowledge of the system-specific energy dispersion relation that links the variables E and k . This dispersion relation provides essential information about how the energy of the system varies with changes in the wave vector and serves as a bridge between different representations of the density of states.

The density of states related to volume V and N countable energy levels is defined as:

$$D(E) = \frac{1}{V} \sum_{i=1}^N \delta(E - E(k_i)) \quad (2.46)$$

As, the minimum permissible change in momentum, denoted as k , for a particle confined within a box of dimensions d and length L is:

$$(\Delta k)^d = (2\pi/L)^d \quad (2.47)$$

Equation (2.46) can be rewritten as:

$$D(E) = \int d^d k / (2\pi)^d \cdot \delta(E - E(k)) \quad (2.48)$$

The calculation of the DOS begins by counting the N allowed states at a specific k that are contained within $[k, k + dk]$ inside the volume of the system. This process involves differentiating the entire k -space volume $\Omega_{n,k}$ in n -dimensions at an arbitrary k with respect to k . The n -dimensional spherical k -space is expressed by:

$$\Omega_n(k) = c_n k^n \quad (2.49)$$

According to this scheme, the density of wave vector states N is, through differentiating $\Omega_{n,k}$ with respect to k , expressed by:

$$N_n(k) = d\Omega_n(k)/dk = n c_n k^{n-1} \quad (2.50)$$

The wavelength (λ) is related to k through the relationship: $k = 2\pi/\lambda$.

Finally we have to find the number of states per unit sample volume at an energy E inside an interval $[E, E + dE]$. The general form of DOS of a system is given as:

$$D_n(E) = \frac{d\Omega_n(E)}{dE} \quad (2.51)$$

The projected density of states (PDOS) is useful for analyzing chemical bonding. It provides the overall density of states (DOS) projected onto localised atomic-like-orbitals. By summing over all these projections, the total density of states is obtained. This analysis helps in understanding the contribution of individual atomic orbitals to the overall electronic structure and provides some information about the behavior of the studied material.

2.4 CP2K code

In this work, all DFT and MD calculations were conducted using the CP2K suite of programs [117]. One major challenge with DFT lies in the computational expense associated with orthogonalizing the wavefunction and calculating the Hartree energy (E_H) (refer to equation 2.30), which does not scale linearly with system size. Consequently, the selection of CP2K was driven by its efficient and scalable DFT implementation, enabling simulations of large systems. The QUICKSTEP approach [118], a prominent technique within the CP2K suite, is also known as the Gaussian and plane waves (GPW) method. This method employs atom-centered Gaussian basis functions and an auxiliary basis of plane waves to expand the wavefunctions (Kohn-Sham orbitals) for solving the Kohn-Sham equations. The electronic density is also expanded using this auxiliary basis of plane waves. Gaussian functions are computationally efficient and relatively straightforward to calculate due to their localized nature, finite extent, and potential availability of analytical solutions. Furthermore, the use of plane waves on uniform grids facilitates the efficient calculation of Hartree energy (E_H) by leveraging the effectiveness of Fast Fourier Transform (FFT) techniques, particularly in cases involving periodic boundary conditions. As a result, it becomes feasible to compute the Kohn-Sham matrix (and total energy) with quasi-linear scaling, given that the FFT is $\mathcal{O}(n \log n)$, allowing the computation to be readily extended to encompass thousands of atoms/electrons. In addition to the conventional diagonalization method employed during self-consistent field (SCF) calculations, CP2K incorporates the orbital transformation (OT) method [119] to achieve wavefunction orthogonalization within the QUICKSTEP method. The use of OT and QUICKSTEP algorithmic approaches renders CP2K exceptionally efficient and proficient in modeling extensive systems within the DFT paradigm. Furthermore, CP2K has been optimized for high-performance computing through parallelization via MPI and OpenMPI [120].



3

Structure of ZrO₂ Nanoparticle Models

Summary

3.1	Computational Details	74
3.2	Experimental Data	75
3.3	NP Model Generations	77
3.3.1	Methodology	77
3.3.2	Assessment of the nanocluster models	81
3.4	Results and Discussions	84
3.4.1	Structure Evolution as a Function of the NP Size	84
3.4.1.1	The overall structure of the NP models	84
3.4.1.2	Disentangling Core and Surface Contributions	85
3.4.1.3	Structural Properties of the Core and Surface Atoms	87
3.5	Conclusions	90

This chapter focuses on generating several ZrO₂ nanocluster models with varying size on stabilizing an appropriate modeling strategy able to reproduce experimental data. Further, we will examine the structural changes corresponding to the nanocluster size. Specifically, we will distinguish between the core and surface of the nanocluster to observe the structural behavior of atoms within the core compared to those at the surface.

3.1 Computational Details

All computations were performed on ZrO₂ nanoparticles (NPs) with a maximum diameter of about 2 nm. Density functional theory calculations within the Kohn-Sham scheme [91], [121] are carried out by using CP2K software employing the mixed Gaussian and plane wave basis set technique [117]. The Perdew-Burke-Ernzerhof (PBE) [122] electron exchange and correlation functional are used for all the calculations, and the core-valence interactions are described by resorting to pseudopotentials of type Goedecker-Teter-Hutter [123]. An atom-centered Triple- ζ valence with polarization (TZVP) [124] basis set is employed to describe the orbitals, while an auxiliary plane-wave basis set is used for the expansion of the electron density. The Brillouin zone is sampled at the Γ point, and a proper convergence of the total energy is achieved by setting the energy cutoff for the expansion of the plane waves to 400 Ry, as shown in Figure 3.1. First-principles molecular dynamics is conducted within the Born-Oppenheimer scheme in the canonical ensemble, integrating equations of motion with a time step of $t = 1$ fs. Optimal thermal control during the dynamics is maintained using a Nosé-Hoover thermostat chain [125]. Atomistic models of [ZrO₂]₁₄, [ZrO₂]₁₆, [ZrO₂]₄₃, [ZrO₂]₈₀, and [ZrO₂]₁₄₁ are generated and placed in a periodic cubic simulation box with side lengths of 25 Å, 25 Å, 30 Å, 35 Å, and 40 Å, respectively. The chosen box size for each system minimizes interactions between periodic replicas.

The atomic pair distribution functions of the atomistic models were calculated using an in-house software implementing an exact formalism [126] to simulate the experimental PDFs obtained from X-ray total scattering measurements using a maximum scattering vector length (Q_{\max}) of 17.0 Å⁻¹. They were averaged over the last 5 ps of the molecular dynamics trajectory.

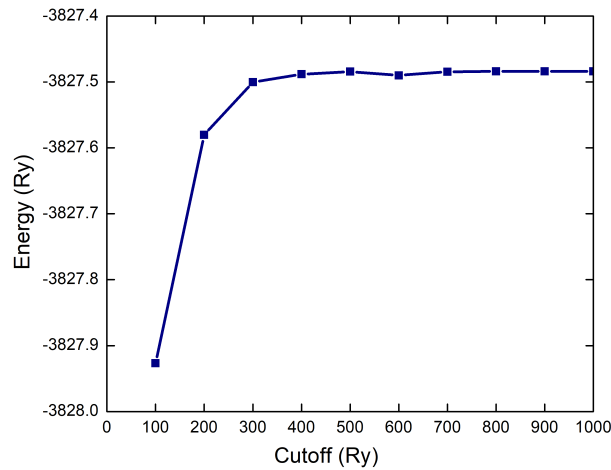


Figure 3.1: Energy convergence test of the cubic polymorph as a function of energy cutoff values.

Geometry optimisation tests were carried out on cubic, tetragonal and monoclinic polymorphs of zirconia (c-ZrO₂, t-ZrO₂ and m-ZrO₂). The optimised cell parameters are given in Table 1 together with the experimental values [127], [128]. As can be seen, the agreement is good.

ZrO ₂ poly-morph	Computed	Experiment [128]
Cubic	$a = b = c = 5.12 \text{ \AA}$	$a = 5.15 \text{ \AA}$
Tetragonal	$a = b = 3.637 \text{ \AA}, c = 5.304 \text{ \AA}$	$a = b = 3.60 \text{ \AA}, c = 5.17 \text{ \AA}$
Monoclinic	$a = 5.189 \text{ \AA}, b = 5.247 \text{ \AA}, c = 5.372 \text{ \AA}$ and $\beta = 99.44^\circ$	$a = 5.15 \text{ \AA}, b = 5.2 \text{ \AA}, c = 5.31 \text{ \AA}$ and $\beta = 99.24^\circ$

Table 3.1: Calculated and experimental cell parameters for cubic, monoclinic, and tetragonal phases of zirconia.

3.2 Experimental Data

The quality of the structure of the nanoparticle models is assessed against experimental PDFs obtained from NP samples produced by soft chemistry at IRCER in previous works [23], [83]. Two different synthesis routes, namely hydrolytic (hereafter referred to as Exp1) and non-hydrolytic sol-gel routes (hereafter referred to as Exp2), were chosen in order to highlight the effect of the synthesis on the structure and modelling procedure of the NPs. The main characteristics are briefly outlined below.

The hydrolytic sol-gel route was based on the zirconium n-propoxide, n-propanol, water, and

acetylacetonate (chelating agent) chemical system, whereas the non-hydrolytic route was based on the zirconium isopropoxide and anisole system in alkaline conditions. With the first method, the water molecules should contribute more significantly to the structural stabilisation of the NPs, while the second is recognised as a very effective method for obtaining small, spherical, monodisperse and non-aggregated particles.

Figure 3.2 shows the experimental PDFs obtained from the two samples with the IRCER laboratory X-ray total scattering setup (details are given in Ref. [23], [83]).

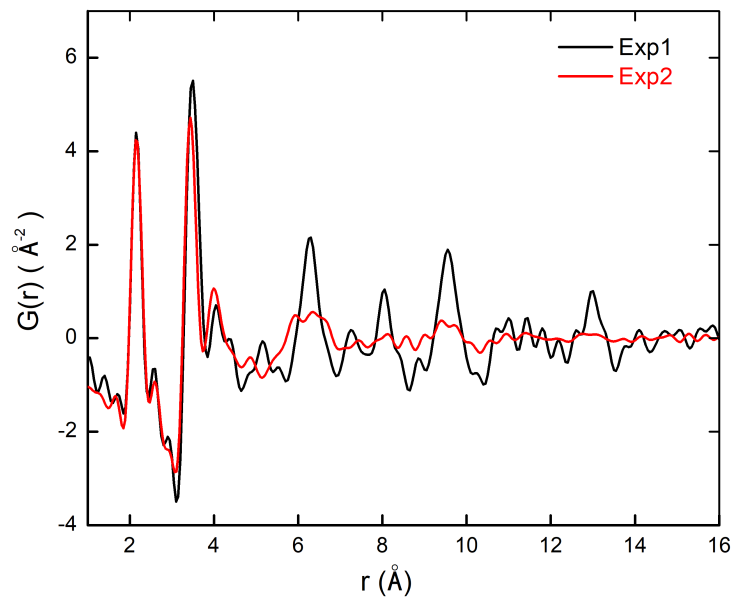


Figure 3.2: Experimental pair distribution function where black and red color shows Exp1 and Exp2 PDFs. Data taken from Ref. [23], [83]

The dampening of the PDFs is very abrupt and indicates that both synthesis methods produced zirconia nanoparticles with very small correlation lengths, around 1.5 nm and 1.1 nm for Exp1 and Exp2, respectively. The first peak at about 2.15 Å corresponds to Zr-O bond lengths. The peak corresponding to the shortest O-O distances at 2.70 Å is barely visible because it merges with the oscillations induced by the finite Q_{\max} value used experimentally (17.0 Å⁻¹). The shortest Zr-Zr distances correspond to the most intense peak at around 3.5 Å for Exp1, and slightly less for Exp2. The subsequent peaks, which lie between 3.9 Å and 4.7 Å, are mainly correlated with Zr-O distances. Interestingly, this region of low r values cannot be fully interpreted on the basis of the known ZrO₂ polymorphs, indicating the presence of structural disorder within the NPs [83].

3.3 NP Model Generations

3.3.1 Methodology

The initial nanocluster models were constructed from the periodic cubic structure of ZrO₂. The cubic polymorph was chosen for simplicity, as it has the highest degree of symmetry, and the other polymorphs are simply distortions of the cubic phase (see Chapter 01). The nanocluster models were derived by extracting atoms within specified radii from a central atom, either Zr or O. The as-obtained models are very close to the stoichiometry. In order to make our models stoichiometric ([ZrO₂]_n, where n is an integer), we remove very few number of atoms from the nanocluster surface. To investigate the size influence on the properties of ZrO₂ NPs, five models were generated, namely [ZrO₂]_n with $n=14, 16, 43, 80,$ and 141 , corresponding to diameters of 0.9 nm, 1.04 nm, 1.32 nm, 1.78 nm and 2.04 nm, respectively. However, all the models obtained have dangling bonds and under-coordinated Zr and O atoms at the surface of the nanoclusters. As stated in the introduction, a structural stabilization effect due to modification of the nanoparticle surface is required to avoid unrealistic, highly disordered, amorphous-like structures. In real systems, the surface structure environment may be disturbed, for instance, by the effects of surface contaminants on the cluster, which may saturate chemical (dangling) bonds and stabilize the nanocluster's structure. In this paper, we use chemisorbed water molecules to mimic possible stabilizing mechanisms. This is an effective and simple way of achieving structural stabilization, although in real systems, more complex molecules (e.g. alkoxide ligands in the case of non-hydrolytic sol-gel routes) may be present instead.

Instead of manually dissociating water molecules on given surface sites, we followed a scheme that avoids prior knowledge of the required surface coverage. For this purpose, water molecules (with number depending on the NP size) were spread out at a distance of 2.2 Å from the surface Zr atoms and their orientation was adjusted to keep them as apart as possible. This ensured a almost uniform distribution. The maximum number of water molecules used was set equal to the number of surface Zr atoms with less than 6 neighbors. This arbitrary value proved adequate for all the models studied and led to 8, 12, 24, 26 and 54 water molecules for the [ZrO₂]₁₄, [ZrO₂]₁₆, [ZrO₂]₄₃, [ZrO₂]₈₀ and [ZrO₂]₁₄₁ nanoparticles, respectively. Resulting models are shown in Figure 3.3. Note that we produce models with fewer water molecules to test the effect of a low passivation rate.

This procedure is expected to saturate chemical dangling bonds after spontaneous water splitting. Geometry optimization of the initial constructed nanoclusters (nanocluster with water molecules) was performed and led to the dissociation of some water molecules, ensuring a partial stabilization of the surface and H bonding with oxygen atoms and OH groups bonding with zirconium atoms. Nevertheless, there were still dangling bonds at the surface of the nanoclusters. In order to

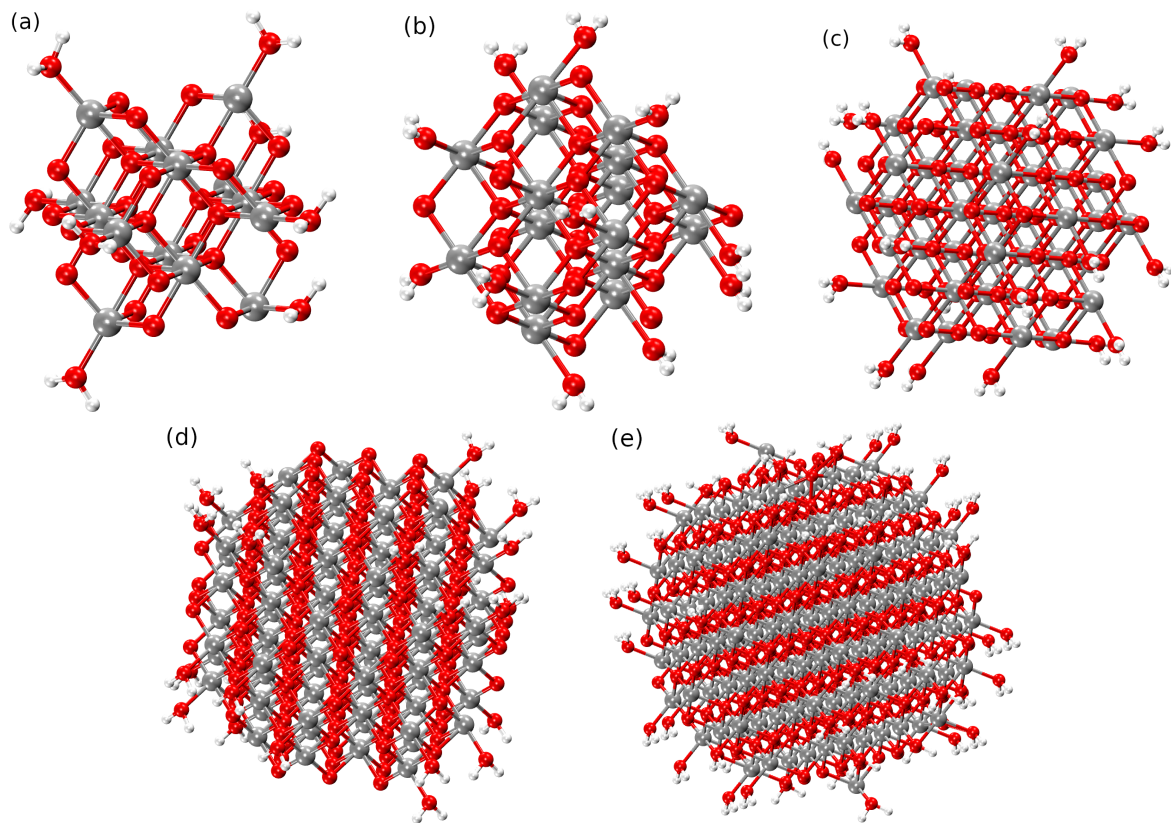


Figure 3.3: Initial NP models with water molecules (a) [ZrO₂]₁₄, (b) [ZrO₂]₁₆, (c) [ZrO₂]₄₃, (d) [ZrO₂]₈₀, and (e) [ZrO₂]₁₄₁.

efficiently minimize the dangling bonds, we need to enhance water splitting and ensure structural relaxation of the nanocluster surface. We have performed molecular dynamics calculations using different thermal treatments (see Figure 3.4).

First, the MD calculation is applied to the optimized nanocluster structures at a temperature $T = 300$ K during 25 ps (thermal treatment 1, later called TT1). The second thermal treatment (TT2) consists of MD simulation at a temperature plateau at $T = 300$ K for 5 ps, followed by a second plateau at $T = 550$ K for 25 ps. The third thermal treatment (TT3) consists of heating at three consecutive temperature steps: $T = 300$ K for 5 ps, $T = 550$ K for 5 ps and $T = 750$ K for 25 ps. After that, a quenching is driven at $T = 550$ K for 4 ps followed by a second at $T = 300$ K for 10 ps.

We first illustrate the impact of thermal treatment with the [ZrO₂]₄₃ model (1.32 nm in diameter). The initial configuration, with 24 H₂O, and the configuration after MD thermal treatment TT3 are shown in Figure 3.5(a) and Figure 3.5(b) respectively. After the MD run, most of the water molecules are chemisorbed (dissociated into H and OH) and the few undissociated molecules remain close to the surface, forming H-bonds. We can also note the appearance of significant

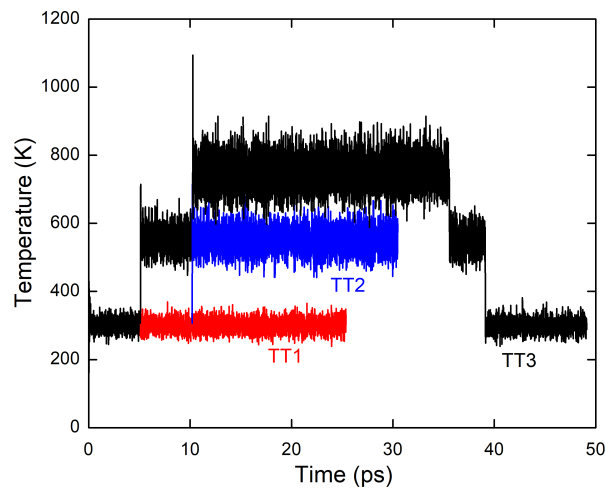


Figure 3.4: Temperature evolution during MD simulation corresponding to three different thermal treatments: TT1 (red), TT2 (blue) and TT3 (black).

positional disorder in the MD-relaxed structure, which nevertheless retains a crystalline character in view of the atomic planes that are still clearly visible.

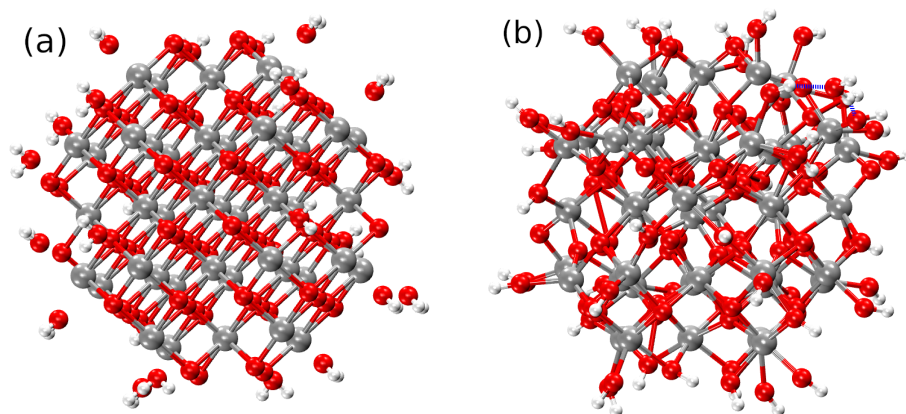


Figure 3.5: (a) Initial structure of [ZrO₂]₄₃ nanocluster covered with 24 water molecules and (b) the final structure obtained after MD thermal treatment TT3. Zirconium, oxygen and hydrogen atoms are in silver, red and white, respectively. Blue dotted line shows the hydrogen bonds.

Figure 3.6 shows the evolution of the number of chemisorbed H₂O molecules over time. Irrespective of the thermal cycle, the number of dissociated molecules reaches a plateau before the end of the simulation, typical of surface saturation at the considered temperature. Comparing the three thermal treatments, annealing at T = 300 K (TT1) leads to the dissociation of 20 water molecules, heating to T = 550 K (TT2) permit the chemisorption of 23 molecules, while a full annealing cycle (TT3) leads to a number of the chemisorbed molecules that fluctuates around 22±1.

Similarly to the [ZrO₂]₄₃ model, the [ZrO₂]₁₄, [ZrO₂]₁₆, [ZrO₂]₈₀ and [ZrO₂]₁₄₁ NPs were produced and annealed by following the thermal treatment TT3. The evolution of the water

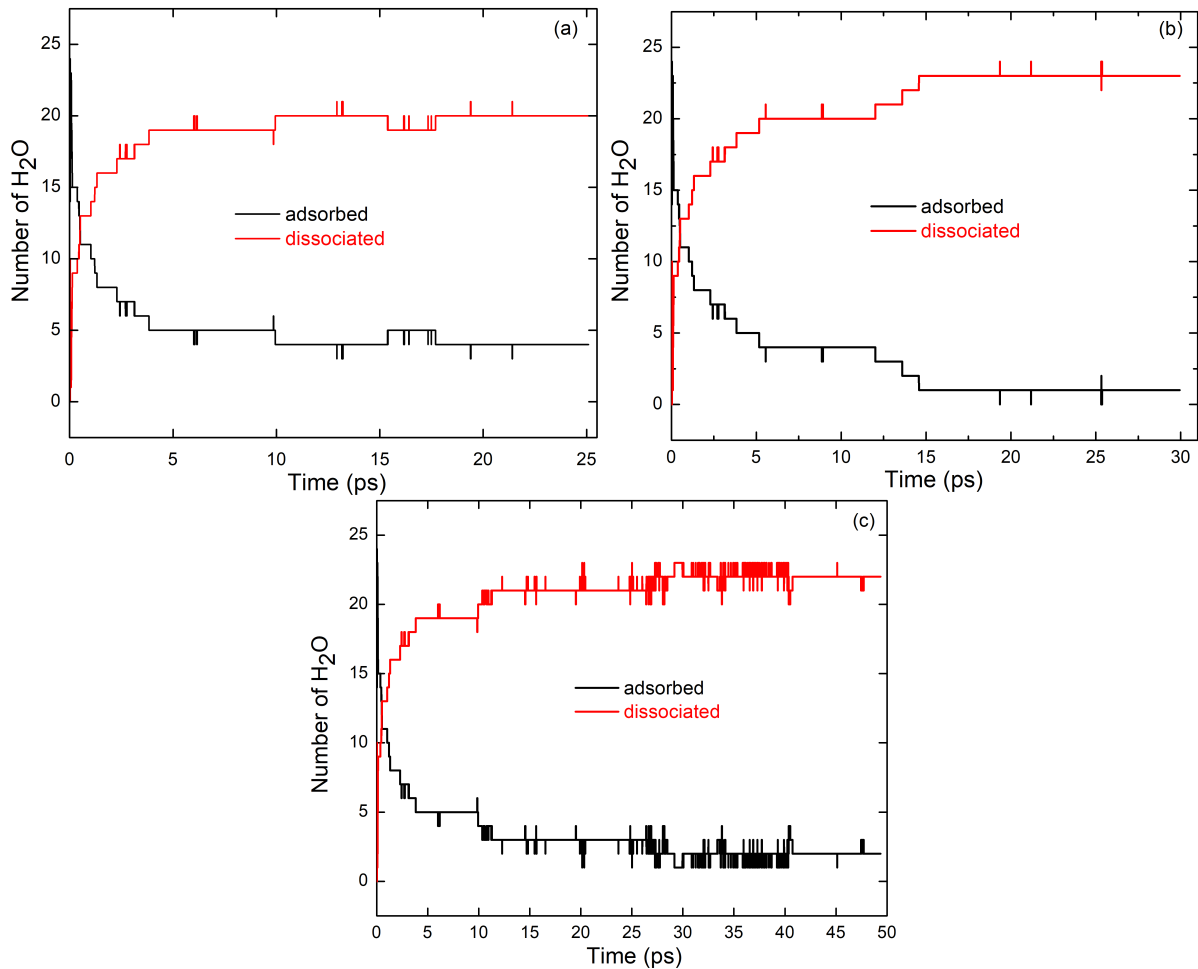


Figure 3.6: Number of chemisorbed and physisorbed water at the surface of [ZrO₂]₄₃ nanocluster during MD thermal treatments (a) TT1, (b) TT2 and (c) TT3.

molecules dissociation rate as a function of the temperature of the TT3 heat treatment is shown in Figure 3.7 (a). It can be seen that for all the studied NPs, the number of dissociated water molecules first increases with temperature, then remains constant after reaching $T = 750$ K, even when the temperature is reduced to $T = 300$ K. In addition, a 100% passivation is achieved for the smallest $n = 14$ and $n = 16$ NPs. In Figure 3.7 (b), the chemisorption rate is depicted as a function of nanoparticle size after thermal treatment TT3. We observe a decrease of this rate with increasing NPs size, with a minimum value of 85% reached for the largest cluster.

All these results highlight the efficiency of using molecular dynamics in achieving a surface passivation without a prior knowledge on the required surface cover.

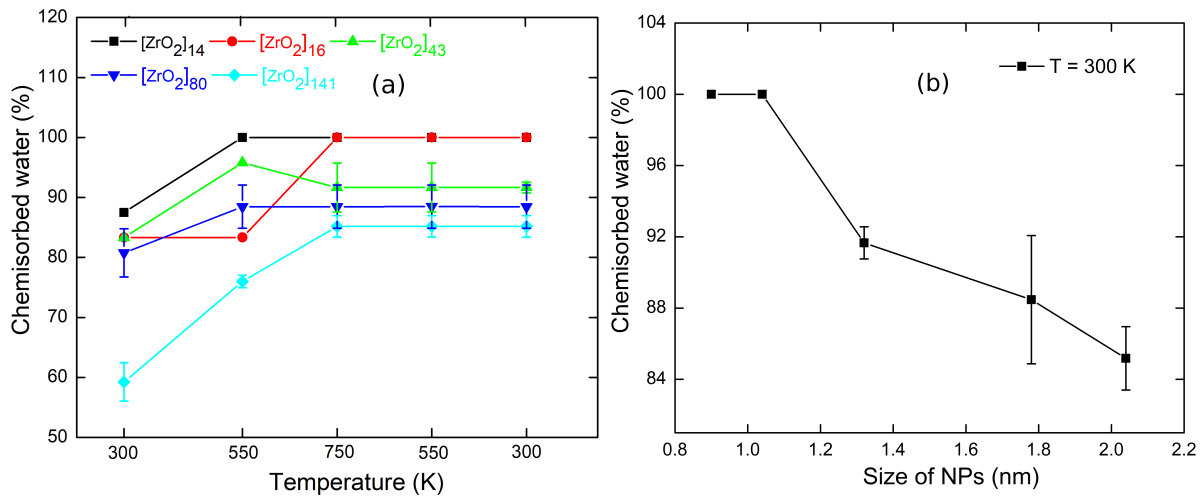


Figure 3.7: Evolution of the rate of chemisorbed water as a function of (a) temperature during thermal treatment TT3 applied and (b) size after quenching at T = 300 K to various [ZrO₂]_n models. The error bars represent the fluctuation of chemisorbed water molecules.

3.3.2 Assessment of the nanocluster models

To evaluate the quality of the generated models, we compare the calculated PDFs with those obtained experimentally through total X-ray scattering.

We first assess the quality of the obtained models using the [ZrO₂]₄₃ nanocluster with the highest passivation rate (92%). Figure 3.8 compares the PDFs calculated over the last 5 ps of the MD trajectory after the TT1, TT2 and TT3 thermal treatments (i.e. at T = 300 K for TT1, T = 550 K for TT2 and T = 300 K for TT3) with the two experimental ones (Exp1 and Exp2). An overall inspection of Figure 3.8 (a) reveals that the models produced after TT3 show the best agreement with the PDF of the Exp1 sample. The first peaks are fairly well reproduced in terms of position, intensity and width, especially in the range from 3 to 5 Å. The two peaks at 4.0 Å and 4.4 Å are perfectly reproduced in the case of the TT3 model only.

A similar trend is observed in the region from 7.1 Å to 8.5 Å where only the TT3 model is able to reproduce the two experimental peaks. For larger distances, no heat treatment is able to reproduce the experimental data due to the limited size of the [ZrO₂]₄₃ model. Figure 3.8(b) compares the calculated PDFs of the [ZrO₂]₄₃ models with data from Exp2 sample (produced in non-hydrolytic conditions). All the models reproduce the experimental PDF fairly accurately for values of *r* below 5 Å and above 9 Å, with the TT3 model being slightly better in the region around 4 Å. However, in the intermediate region, all three models give peaks that are better defined than experimentally, suggesting that they still lack structural disorder.

Overall, it appears that the TT3 treatment, implementing a full annealing cycle, produces

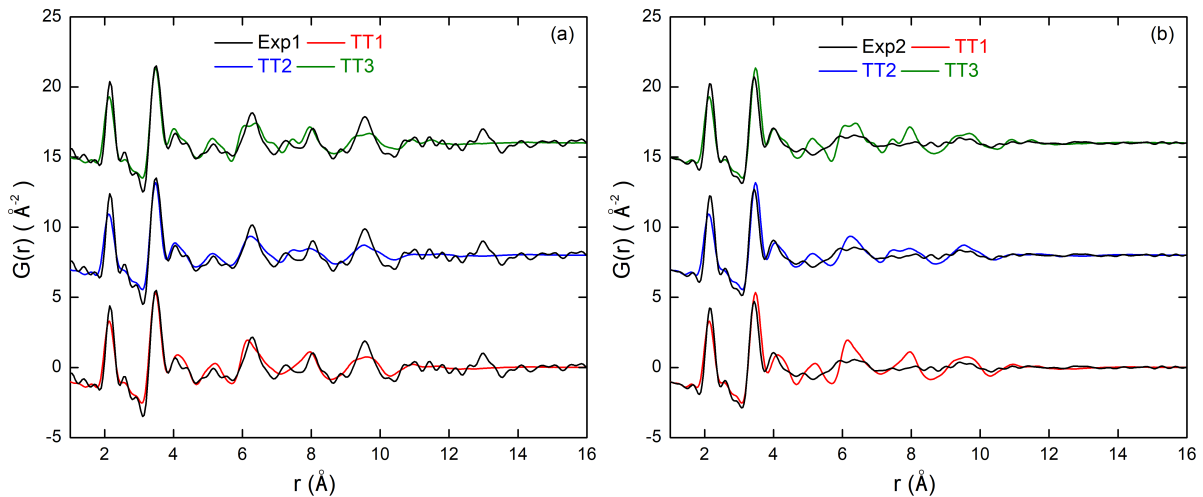


Figure 3.8: PDFs computed from the resulting structure of [ZrO₂]₄₃ nanocluster after thermal treatments, compared to the experimental (a) Exp1 PDF, and (b) Exp2 PDF.

the best models of relaxed structures at room temperature, capable of reproducing the fine details of both experimental PDFs.

Beside the thermal treatment and NP size, the surface coverage is another important factor that can affect the structure of the simulated NPs. In the above analysis we only considered NPs models with a maximum coverage of their surfaces. We now focus on the effect of partial stabilization of the nanoparticle surface. To this end, we also built models based on the [ZrO₂]₄₃ and [ZrO₂]₁₄₁ clusters with a surface coverage of 16.7% and 33.3% and annealed using the TT3 treatment. These passivation rates correspond respectively to 4 and 8 chemisorbed H₂O molecules for the [ZrO₂]₄₃ model and 18 and 54 molecules for the [ZrO₂]₁₄₁ model, respectively.

The calculated PDFs of the [ZrO₂]₄₃ models are presented in Figure 3.9(a,b) and compared with the experimental data. We remark that as the passivation rate decreases, the two intense peaks (corresponding to Zr-O and Zr-Zr distances) shift their positions toward lower distances compared to both experimental PDFs. This trend can be explained by the increase of the fraction of dangling bonds at the surface of nanoclusters, leading to a decrease in the Zr coordination number and consequently a shortening of the Zr-O bonds and a contraction of the Zr-O-Zr bridges. Focusing on Exp1, we find that the maximum passivation model shows the best agreement with the experimental PDF. In contrast, for Exp2, partially passivated models appear to be the best compromise, as they better reproduce the flat, broad peaks of the experimental PDF in the r region above 5 Å, while maintaining good agreement in the low r region.

In the case of the [ZrO₂]₁₄₁ clusters (Figure 3.9 (c,d)), the best agreement is obtained between the maximum passivation model and data from Exp1 sample. However, although this

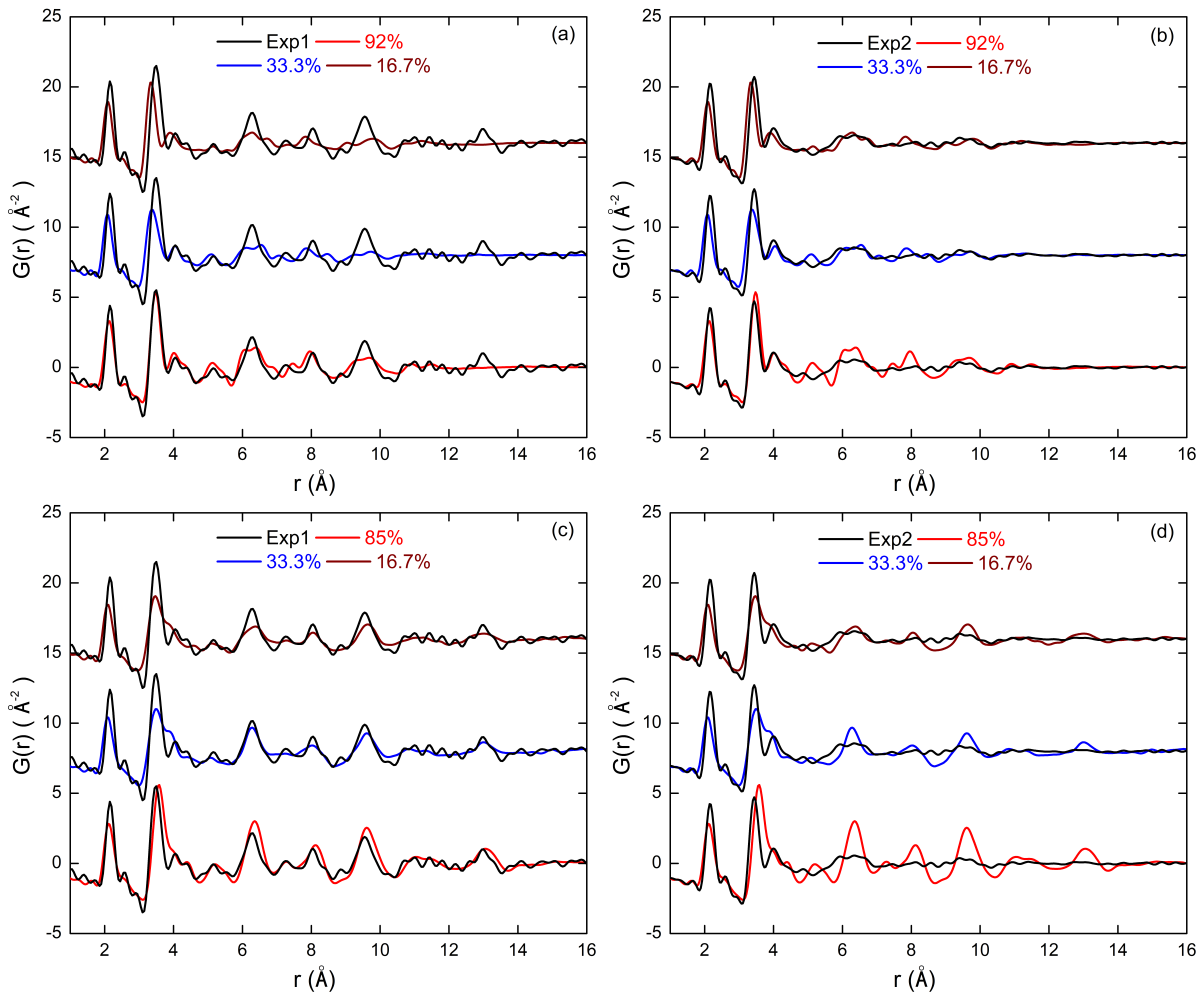


Figure 3.9: The PDFs computed from the resulting structure after thermal treatment TT3 are analyzed in relation to the amount of surface coverage. A comparison is drawn between the experimental PDFs, labeled as (a) Exp1 and (b) Exp2, for the [ZrO₂]₄₃ nanocluster. Likewise, the experimental PDFs (c) Exp1 and (d) Exp2 are compared for the [ZrO₂]₁₄₁ nanocluster.

model reproduces the peaks of the PDF fairly well for intermediate and larger values of r , it does not capture the details of the PDF in the region of low values of r , much less well than the [ZrO₂]₄₃ model. For Exp2 sample, none of the considered [ZrO₂]₁₄₁ models can reproduce the experimental PDF. This is certainly due to the size of the model, which is too large compared with that of the nanoparticles of Exp2 sample.

Overall, these results suggest that the [ZrO₂]₄₃ model produced following the full thermal annealing cycle TT3 is able to capture the details of both Exp1 and Exp2 samples by varying its surface passivation rate from 92% to 16.7% respectively. This observation seems to be consistent with the synthesis protocols used in Exp1 and Exp2. Indeed, we expect a greater passivation effect under hydrolytic conditions, as water molecules can more easily bind to metal oxide surface

sites than larger organic molecules present in a non-hydrolytic reaction medium. In addition, these results show that achieving an accurate structural models of metal-oxide NPs requires an assessment of the particle size, the surface passivation rate and the MD thermal treatment.

3.4 Results and Discussions

3.4.1 Structure Evolution as a Function of the NP Size

3.4.1.1 The overall structure of the NP models

In order to investigate the NP structure evolution as a function of their size, we computed the partial pair distribution function on the NP models produced through a full thermal annealing cycle (TT3) with maximal passivation rate. The obtained results for the [ZrO₂]_n models with $n=14, 16, 43, 80$ and 141 are shown in Figure 3.10. By looking at the Zr-O partial PDF (Figure 3.10 (a)), regardless of the nanocluster size, we see a first intense peak occurring at around 2.12 \AA , characteristic of the Zr-O chemical bond length. The second and third peaks, located at distances between 3 and 6 \AA , are well resolved and clearly visible for the larger NP models and becomes broader and less intense as the size of the nanocluster decreases. In the case of [ZrO₂]₁₄ and [ZrO₂]₁₆ NPs, they are particularly spread out over the range of r values considered. These differences observed with decreasing NP size are very similar to those between the Zr-O partial PDFs of cubic and monoclinic zirconia (see Figure 3.12 in the following sections). This suggests that smaller NPs tend to have a more monoclinic-like structure. For higher r values, the peaks are dampened due to the reduction in NP size, but oscillations are still visible up to r values close to the NP diameter, reflecting the crystalline nature of the NP.

Focusing now on the O-O partial PDFs (Figure 3.10 (b)), we can see for the largest nanocluster an intense peak at 2.7 \AA followed by a shoulder at 3.3 \AA . As the size of the nanoclusters decreases, the first peak shifts slightly towards lower r values and the shoulder turns into a well-separated intense peak. At the same time, the third peak at around 4 \AA , clearly visible for all cluster sizes, shifts slightly towards higher r values. Overall, the partial PDF of the smallest nanocluster more closely resembles that of the monoclinic polymorph, but the trend observed in the evolution with NP size of the shape of the Zr-O partials, from cubic to monoclinic, is less evident here.

The Zr-Zr partial PDFs (Figure 3.10 (c)) show the most significant changes as a function of NP size. For the largest model a single broad peak centered around 3.6 \AA is present, followed by 3 peaks at about $5.1, 6.3$ and 7.3 \AA . As nanocluster size decreases, the first peak shifts to lower r values and splits in two, leading to an intense peak at 3.3 \AA followed by a smaller one at 3.9 \AA for the smallest NP. At the same time, the 3 next peaks change in position and intensity to form a flatter shape made of 4 bumps at around $5.2, 5.7, 6.2$ and 6.5 \AA for the smallest model. As

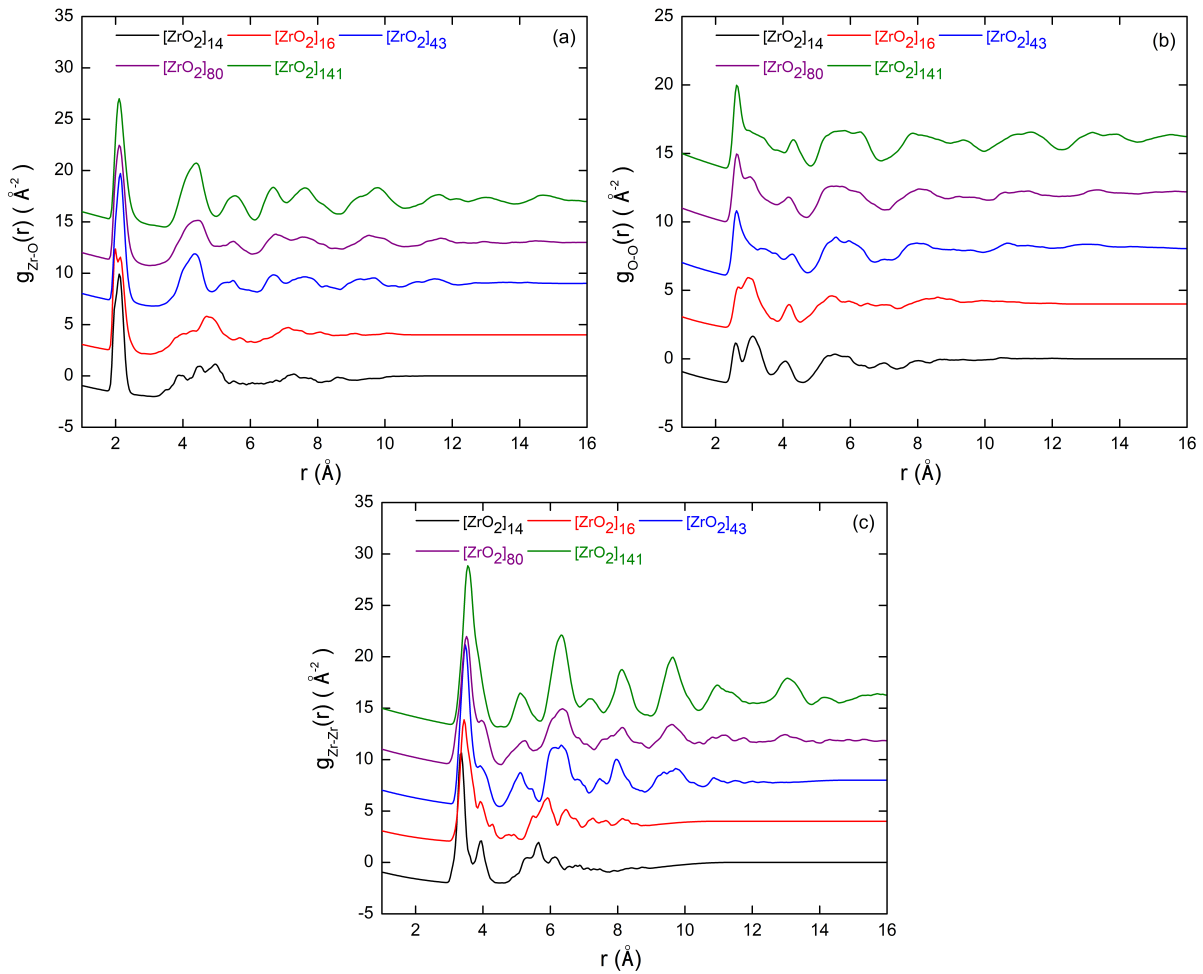


Figure 3.10: The computed partial PDFs related to (a) Zr-O, (b) O-O, and (c) Zr-Zr distances for the ZrO₂ nanocluster models.

with the Zr-O partial, this evolution suggests a transition from a more cubic to a more monoclinic structure with decreasing NP size.

The above analysis shows that there is a strong correlation between the size of nanoparticles and their structure; in particular, the smaller the size, the closer the structure is to the monoclinic polymorph. Given the high proportion of surface atoms in nanoparticles, this opens the question of the contribution of surface atoms to the overall structure and electronic properties of NPs, as well as the presence of a boundary between surface atoms and core atoms for such small particles.

3.4.1.2 Disentangling Core and Surface Contributions

In order to establish whether there is a boundary between the atoms belonging to the core and those belonging to the surface, we used the length of the Zr-O bond as a structural fingerprint. This choice was motivated by the sensitivity of this descriptor to the coordination of the Zr

atom. Indeed, Zr atoms on the NP surface are expected to have bonds with terminal or under-coordinated O atoms, which should be slightly shorter than those in the reference bulk material. In practice, we computed the average Zr-O distance within a shell of 3 Å width. The position of this shell was shifted from the centre of the NP to the surface, thereby providing the average evolution of the Zr-O bond length as one approaches the NP surface. All the calculations were averaged over the last 5 ps of the considered trajectory. The results are provided in Figure 3.11.

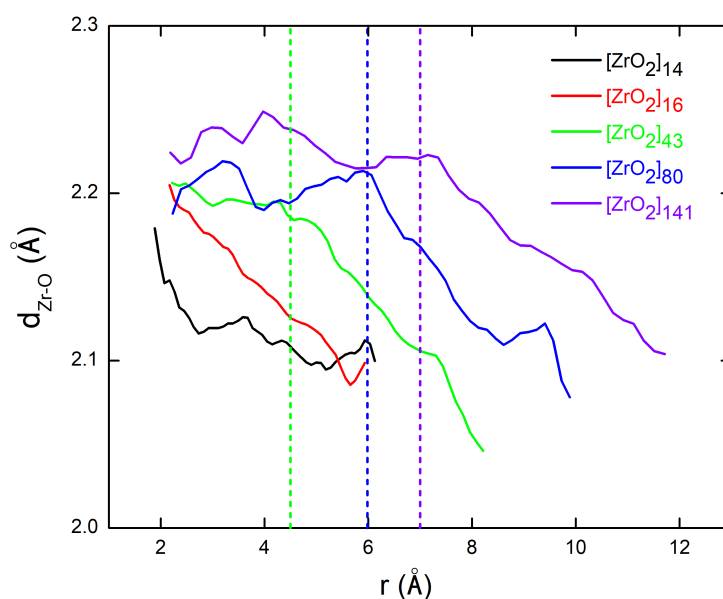


Figure 3.11: Evolution of Zr-O bond length as a function of the position of the atoms in the NP for various size of ZrO₂ models.

For the two smallest nanoclusters, the average Zr-O distance immediately decay beyond the coordination sphere of the central atom and reaches a value around 2.1 Å at the surface of the NP. This behaviour can be explained by the fact that for such small NPs, the surface has such a strong influence on the overall NP structure that it is not possible to make a distinction between the core atoms and the surface atoms. On the other hand, for the larger models, the average Zr-O bond length is initially almost constant, with a value close to 2.2 Å, before decreasing towards values of the order of 2.1 Å. Threshold values around 4.5, 6.0 and 7.0 Å are found for the [ZrO₂]_n models with n=43, 80 and 141 respectively. These values delimit the regions from which surface effects start to be important, thus affecting the average Zr-O bond length. Interestingly, the fraction of atoms belonging to the surface is found to be around 82 %, 76 %, and 79 % for models with n=43, 80 and 141, respectively.

3.4.1.3 Structural Properties of the Core and Surface Atoms

We now use the core-surface thresholds established in the previous section and investigate the structural features of each region of the NP. To this end, we computed the histograms of the Zr-O, O-O and Zr-Zr distances for atoms belonging to the core or to the surface of the NPs, and compare them to the partial PDFs calculated from the cubic and monoclinic ZrO₂ polymorphs. The results are shown in Figure 3.12.

In the case of the smallest $n=14$ and 16 models, the histograms were computed by considering all the atoms of the NPs. The distribution of Zr-O, O-O, and Zr-Zr distances in these systems show a high similarity with the corresponding partial PDFs of the monoclinic structure in terms of peak positions and widths, which is in line with the discussion of previous sections.

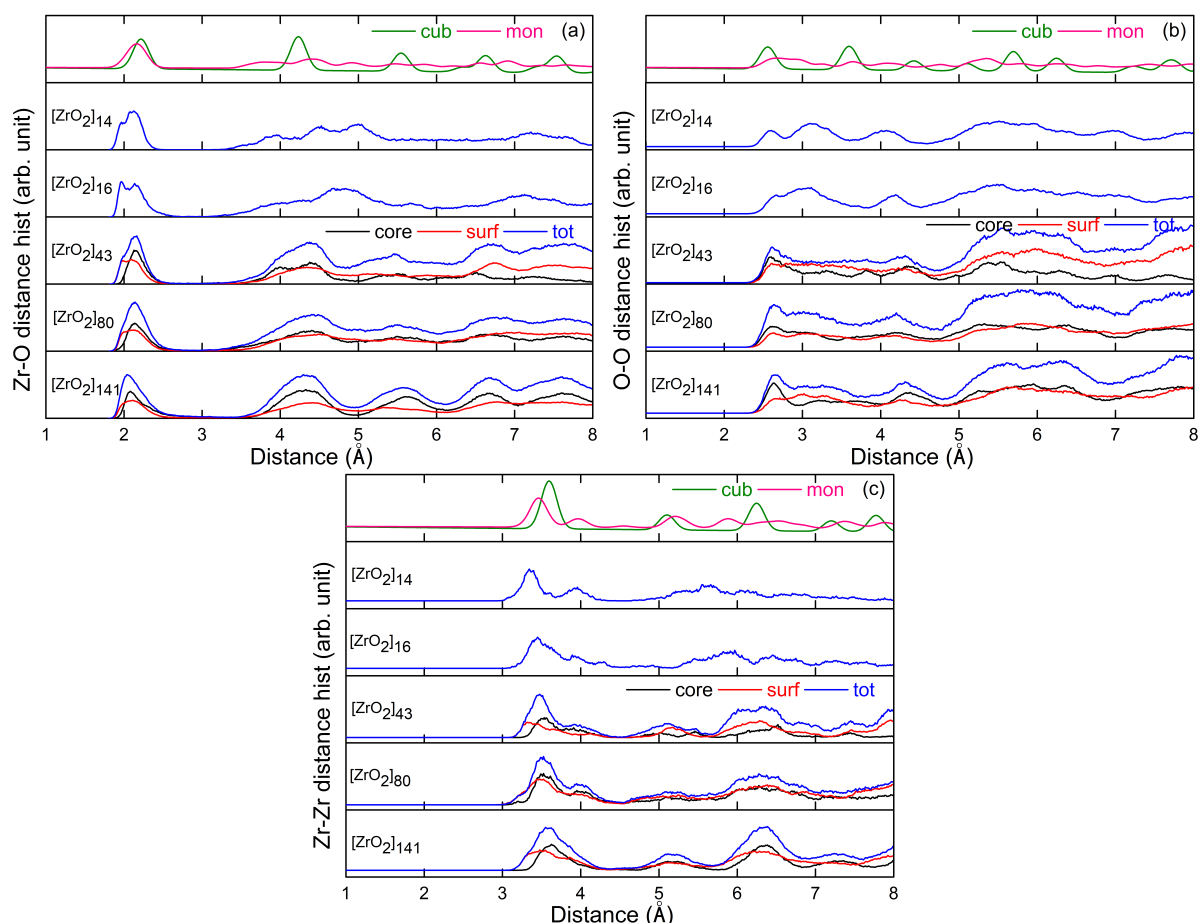


Figure 3.12: Histogram of (a) Zr-O, (b) O-O and (c) Zr-Zr distances found in nanocluster models with various sizes, compared with the calculated partial PDFs from the cubic and monoclinic polymorphs of zirconia (upper curves)

For larger nanoclusters, Figure 3.12(a) shows that the first peak of Zr-O distances is made up of

two distinct contributions. The first comes from atoms belonging to the NP core and is centered around 2.15 Å, 2.15 Å and 2.11 Å for the [ZrO₂]₄₃, [ZrO₂]₈₀ and [ZrO₂]₁₄₁ models, respectively. These peaks occur at a slightly shorter distance than Zr-O distance in the cubic phase of zirconia. The second contribution comes from surface atoms. The peaks are broader and located at shorter distances, recalling those of the monoclinic structure. Similarly, for larger distances, the histograms calculated from the surface atoms are flatter than those calculated from the core atoms, which is also reminiscent of a monoclinic distortion. In the case of O-O correlations, the atoms belonging to the NP core generate a well-defined first peak, located at 2.60 Å, 2.62 Å and 2.64 Å for [ZrO₂]₄₃, [ZrO₂]₈₀ and [ZrO₂]₁₄₁ models, respectively, corresponding better to what is observed with the cubic structure. For the surface atoms, a much broader and almost flat peak is observed in the range of 2.4 to 3.6 Å, similar to that observed in the monoclinic phase. Finally, the Zr-Zr correlations in the core of the NP feature first distances of 3.49 Å, 3.54 Å and 3.57 Å in the case of [ZrO₂]₄₃, [ZrO₂]₈₀ and [ZrO₂]₁₄₁, respectively, in a close agreement to those reported in cubic ZrO₂. Those in the surface of the NP show slightly shorter distance in better agreement with the monoclinic zirconia polymorph. The second peak at 4 Å typical of the monoclinic structure is also present for most of the NP models. Interestingly, this peak is more pronounced in the case of the small NPs and tend to merge with the main Zr-Zr peak as the NP size increase. In addition, both the surface and core Zr atoms contribute the this peak irrespective of their size. In the case of the largest [ZrO₂]₁₄₁ model, we note that all the peaks due to the core atoms reproduce very well the Zr-Zr partial PDF of the cubic phase, while those induced by the surface atoms are similar to the partial PDF of the monoclinic phase, albeit with substantial broadening.

Overall, the above analysis demonstrates the effectiveness of using the Zr-O bond length to distinguish the core and surface regions of ZrO₂ NPs. In addition, by focusing on the histograms of the Zr-O, O-O and Zr-Zr distances, it turns out that the core of the largest NPs shows a strong similarity to the cubic phase, while the surface of the NPs tends to be closer to the monoclinic phase. Such a finding highlights the importance of surface reconstruction of metal-oxide nanoparticles, where a simple ideal NP model will fail in explaining the overall structure of the NP.

To complement the above results, we analysed the environment of the Zr atoms in the core and on the surface of the nanoclusters by applying the Rigorous Investigation of Networks Generated using Simulation (RINGS) code [129], [130].

Specifically, we computed the coordination numbers of Zr-atoms within the core and at the surface of [ZrO₂]₄₃, [ZrO₂]₈₀, and [ZrO₂]₁₄₁ nanoclusters, as illustrated in Figure 3.13 (a), (b), and (c), respectively. Across all the models, Zr-atoms within the core mainly displayed a high proportion of 7-fold geometry and a lower proportion of 6-fold geometry. Conversely, the surface predominantly exhibited 6-fold geometry with a notable proportion of 5-fold geometry.

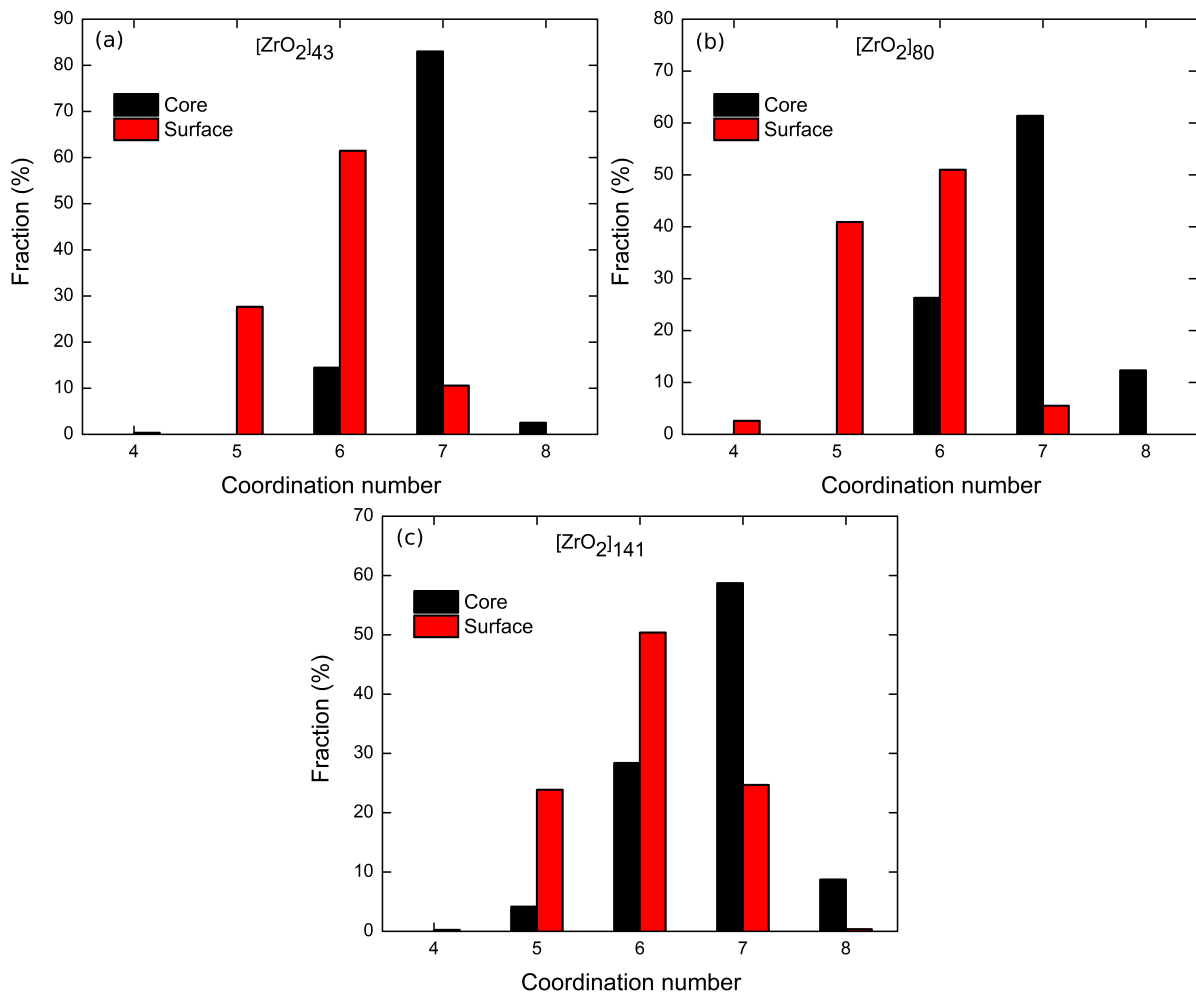


Figure 3.13: Fraction of the coordination number of Zr-atoms within the core and the surface of (a) [ZrO₂]₄₃, (b) [ZrO₂]₈₀ and (c) [ZrO₂]₁₄₁, nanoclusters.

Specifically, the core regions of the [ZrO₂]₈₀ and [ZrO₂]₁₄₁ models showcased 8-fold geometry due to their larger sizes. Additionally, in the case of the larger nanocluster ([ZrO₂]₁₄₁), Zr-atoms on the surface displayed a combination of 5-fold, 6-fold, and 7-fold geometries with a significant fraction, whereas the other nanoclusters primarily showed 5-fold and 6-fold geometries. Notably, the fraction of 7-fold geometry for the larger nanocluster was higher than that for the other nanoclusters on the surface, suggesting less distortion at the surface compared to the other nanoclusters. The various local environments populations is depicted in Table 3.2. Hence, this analysis leads to the conclusion that the overall coordination number of Zr-atoms within the core region close to the cubic phase, while the surface region tends towards the monoclinic phase.

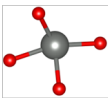
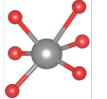
						
		ZrO ₄	ZrO ₅	ZrO ₆	ZrO ₇	ZrO ₈
[ZrO ₂] ₄₃	Core	0 %	0 %	14.45 %	83 %	2.5 %
	Surface	0.33 %	27.63 %	61.46 %	10.57 %	0 %
[ZrO ₂] ₈₀	Core	0 %	0 %	26.30 %	61.37 %	12.32 %
	Surface	2.58 %	40.92 %	50.98 %	5.5 %	0 %
[ZrO ₂] ₁₄₁	Core	0 %	4.16 %	28.37 %	58.71 %	8.74 %
	Surface	0.23 %	23.87 %	50.37 %	24.67 %	0.35 %

Table 3.2: Fraction of coordination number for Zr-atoms within the core and the surface for various size of nanoclusters.

3.5 Conclusions

In this chapter, we first build several nanoclusters models of [ZrO₂]_n, where n=14, 16, 43, 80, and 141, in order to study the size influence on the system properties. We were placed water molecules on top of Zr atoms at the surface of nanoclusters in order to passivate the dangling bonds. In this work, Quantum MD simulations at different temperatures were performed in order to study the structural and electronic properties of ZrO₂ nanoparticles. Second, we have computed the PDFs following the thermal treatments of TT1, TT2 and TT3 by considering the last 5 ps of the equilibrated trajectory of each model and compared them with experimental PDFs in order to validate our models. As a result, we found that [ZrO₂]₄₃ with maximum surface passivation and [ZrO₂]₄₃ with 16.7% surface passivation using thermal treatment (TT3) are in good agreement with the experimental PDFs, Exp1 and Exp2, respectively. Although, the calculated PDF for maximally passivated [ZrO₂]₁₄₁ nanocluster are in good agreement with the Exp1 PDF at larger range distances. However, the presence of water molecules at the surface of nanoclusters, as reported in this work, is just one of the plausible stabilizing mechanisms, it is nevertheless an effective and straightforward method to accomplish structural stability. Third, we calculate the evolution of the Zr-O bond length as a function of the position of the atoms in the NP. Surprisingly, we found that the Zr-O bond length decreases when goes from the core to the surface of the NP. Finally, we have disentangled the atoms in the core and the surface of nanoclusters to investigate the structural modifications. By looking to the histograms, we have noticed that the atoms in the core exhibit behavior similar to that of the cubic phase zirconia, while the atoms at the surface of the nanoclusters exhibit behavior similar to that of the monoclinic phase of zirconia. Finally, we compute the fraction of coordination numbers for Zr-atoms within the core and those within the surface of various size of nanoclusters. It has been

observed that the core exhibits a mixture of high fraction of 6 and 7-fold coordination numbers, while the surface predominantly displays coordination numbers of 4, 5, and 6, respectively.



4

Structure of SnO₂ Nanoparticle Models

Summary

4.1	Computational details	93
4.2	Generation of SnO ₂ nanocluster models	93
4.2.1	Methodology	93
4.2.2	Assessment of the nanocluster models	96
4.3	Results and Discussions	98
4.3.1	Partial PDFs as a function of size of the NPs	98
4.3.2	Disentangle the core and surface of nanoclusters	100
4.3.3	Structural properties of the core and surface atoms	101
4.3.4	Comparison of local environments of core and surface atoms for ZrO ₂ and SnO ₂ nanoclusters	106
4.4	Conclusions	107

This chapter focuses on the generation of several models of SnO₂ nanoclusters with varying sizes and the study of their structural properties. After presenting the computational details, we investigate the evolution of the nanocluster structure as a function of the size with a particular attention to the core-surface contributions.

4.1 Computational details

A computational setup similar to that used in the case of ZrO₂ systems is employed in the case of SnO₂. In particular, we use a TZVP basis set for all the atoms and resort to PBE exchange and correlation functional along with GTH type pseudopotentials. Cutoff energies of 500 Ry (cutoff) and 50 Ry (rel cutoff) were used and ensured a proper convergence of the total energy. In all the FPMD simulations, periodic boundary conditions were applied. Nanoclusters were placed in the middle of a cubic simulation box with box sides of 20 Å, 25 Å, 30 Å, 35 Å, 38 Å, and 40 Å employed for [SnO₂]₁₅, [SnO₂]₂₃, [SnO₂]₃₁, [SnO₂]₄₈, [SnO₂]₆₉, and [SnO₂]₁₀₃, respectively, in order to avoid any interaction between periodic replica. MD was performed in the canonical ensemble (NVT) with a timestep of 1 fs to solve the equations of motion and a Nosé-Hoover thermostat ensured an optimal thermal control.

4.2 Generation of SnO₂ nanocluster models

4.2.1 Methodology

We construct several initial nanocluster models by cutting a sphere of radius r in the tetragonal structure of SnO₂. We consider either Sn or O atoms as the center of the sphere. Most of the resulting nanocluster models show the correct stoichiometry ([SnO₂] _{n} , where n is an integer), and when needed, the stoichiometry of the models is achieved by removing a very few number of atoms from the nanocluster surface. To explore the size effects on the structure-properties relationship, we modeled six nanoclusters with varying sizes, namely [SnO₂] _{n} with $n = 15, 23, 31, 48, 69, \text{ and } 103$. The corresponding sizes are 0.98 nm, 1.18 nm, 1.27 nm, 1.54 nm, 1.7 nm, and 1.94 nm, respectively. By looking at our models, they exhibit Sn and O dangling bonds on their surfaces, resulting in a deficiency of fully coordinated atoms at the surface. Therefore, water molecules were strategically placed at a distance of 2.2 Å from the surface Sn atoms, which exhibited a coordination number of four or less. In the case of [SnO₂]₁₅, [SnO₂]₂₃, [SnO₂]₃₁, [SnO₂]₄₈, [SnO₂]₆₉ and [SnO₂]₁₀₃, 9, 15, 17, 22, 27, and 41 H₂O, were positioned at the surface Sn-atoms, respectively (see Figure 4.1).

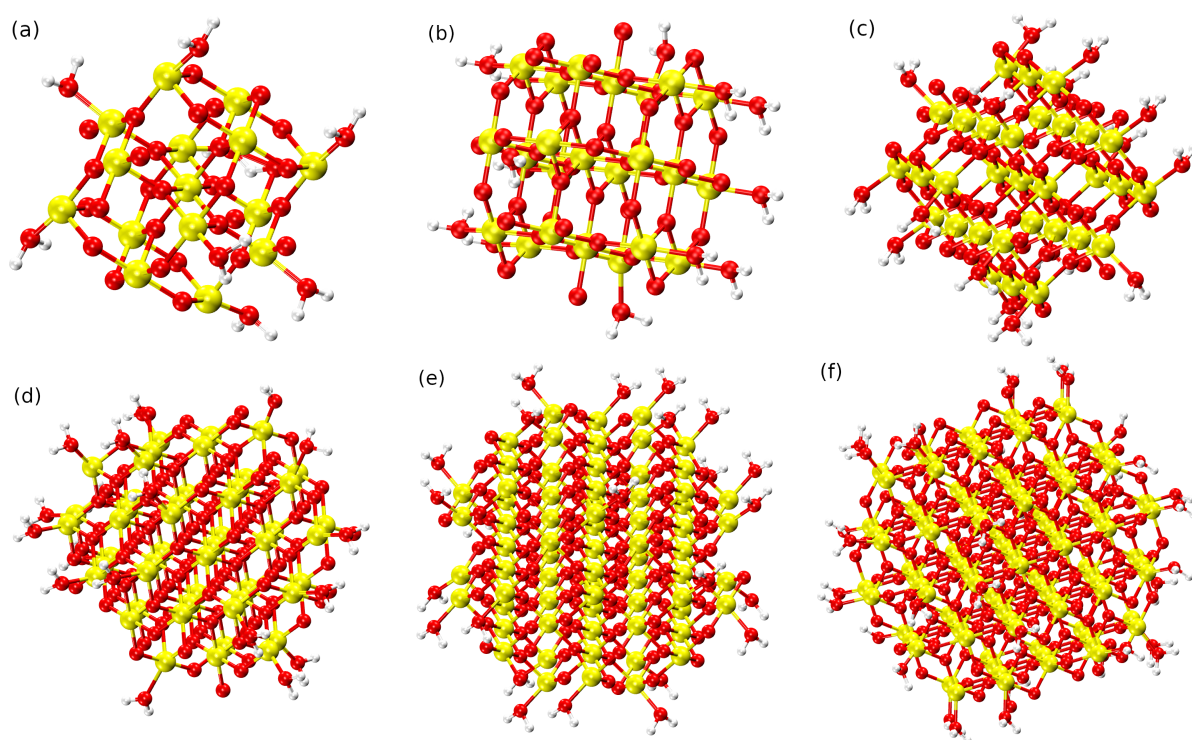


Figure 4.1: Initial structure with water molecules of modelled NPs (a) [SnO₂]₁₅, (b) [SnO₂]₂₃, (c) [SnO₂]₃₁, (d) [SnO₂]₄₈, (e) [SnO₂]₆₉, and (f) [SnO₂]₁₀₃.

Starting with the initially surface-covered nanocluster models, we conducted geometry optimization calculations, resulting in the dissociation of certain water molecules. This process led to a partial passivation of the surface, with H positioned on top of O and OH on top of Sn surface atoms. Despite this optimization, dangling bonds persisted at the nanocluster surface. Subsequently, molecular dynamics simulations were employed at different temperatures, as illustrated in the thermal cycle depicted in Figure 4.2, to facilitate water splitting and induce structural relaxation of the surface for the generation of stable structures. Following the simulation protocol established in the case of ZrO₂, a thermal scheme similar to TT3 was adopted in order to achieve a full dynamical relaxation of the NP models. In practice, the TT3 thermal treatment involved a heating phase at three consecutive temperature steps: T = 300 K for 5 ps, T = 550 K for 5 ps, and T = 750 K for 25 ps, followed by a quenching cycle.

During the heating step, the majority of water molecules split into H and OH, passivating the surface Sn-atoms with OH and O-atoms with H. Undissociated water molecules still contribute to stabilization of the surface through hydrogen bonds or adsorption onto Sn-atoms. Nevertheless, at T = 750 K some of these water molecules are observed to move away from the nanoparticle surface during MD simulations. Consequently, dimers or peroxides (Sn-O-O) are formed on the nanoparticle surface in all the NP models. These dimers arise due to oxygen singly bonded to a tin atom. In the case of [SnO₂]₄₈, trimmers (Sn-O-O-O-Sn) attached to the surface Sn-atoms

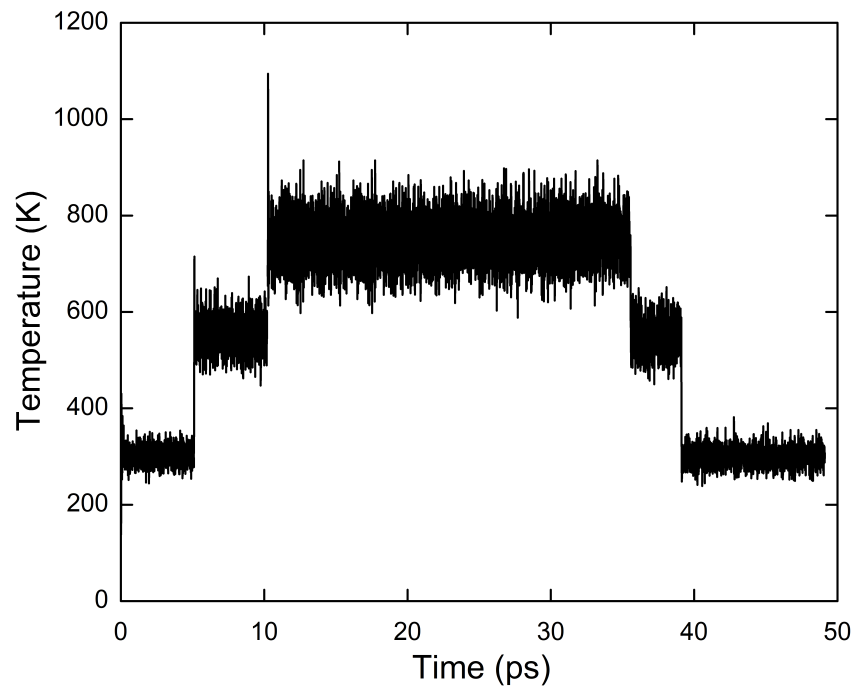


Figure 4.2: Temperature evolution during MD simulation of thermal treatment TT3.

of the nanoparticle are also observed (see Figure 4.3). These defects were reported in a previous study on modeling unpassivated SnO₂ nanoparticles, where it was demonstrated that they hamper the electronic properties of the material [79].

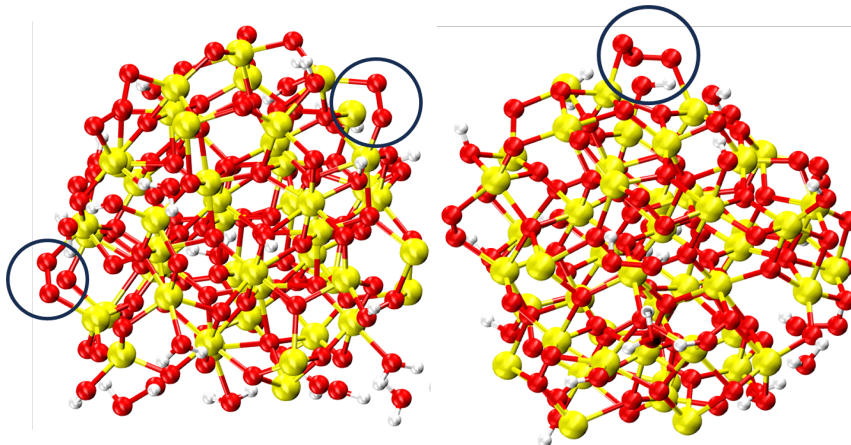


Figure 4.3: Representative snapshots on NP with O dimers and trimers at the surface.

Figure 4.3 shows some representative defective surface structures and Figure 4.4 illustrates the computed partial PDF for O-O distances across various sizes of SnO₂ nanoclusters. A small peak is observed at 1.4 Å in the O-O PDF reflecting the occurrence of oxygen dimers and trimers

regardless of the NP size.

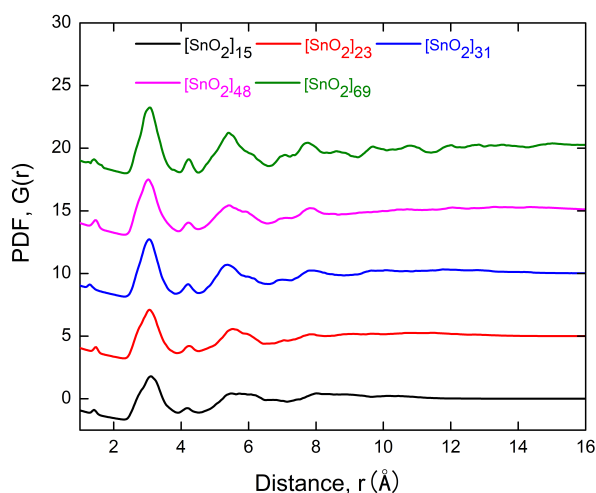


Figure 4.4: The calculated partial PDF of O-O distances as a function of NPs size.

In order to prevent the formation of such surface defects, we adopt a complementary passivation procedure in which we recover a system snapshot at $T = 750$ K where some water molecules start to move away from the surface and identify the neighboring under-coordinated O and Sn atoms. Subsequently, we manually split those flying water molecules into H and OH, and position them on the surface O of Sn atoms, respectively. This approach result in 100 % surface passivation of our models where all the O-O surface defects are removed. Then, the TT3 treatment is extended at $T = 750$ K for a 10 ps followed by a quenching phase at $T = 550$ K for 4 ps and $T = 300$ K for 10 ps (see Figure 4.2). Representative snapshots of the final structures are provided in Figure 4.5.

4.2.2 Assessment of the nanocluster models

In order to confront our models to experiment, we calculated the total neutron PDFs of the six models and compared them with an experimental neutron PDF taken from the literature [131]. This PDF was obtained on SnO₂ NPs of 5 nm in diameter and synthesised by solution-phase growth followed by a surface-capping treatment with water molecules. The results are shown in Figure 4.6. Before going into the comparison, let us first focus on the experimental PDF (plotted with black lines in Figure 4.6). The peaks can be assigned as follow: the first prominent peak corresponds to Sn-O bond length and occurs at a distance of 2.10 Å. The peak corresponding to the first O-O correlations manifests at distances ranging from 2.60 Å to 2.95 Å. In addition, a peak is found at a distance of 3.22 Å, correlating with both O-O and Sn-Sn distances, while two peaks associated with Sn-O, O-O and Sn-Sn correlation lengths are observed at distances of 3.75 Å and 4.23 Å, respectively. Due to the larger size of the real NPs compared with our models, several peaks are still visible in the experimental PDF at distances larger than 10 Å.

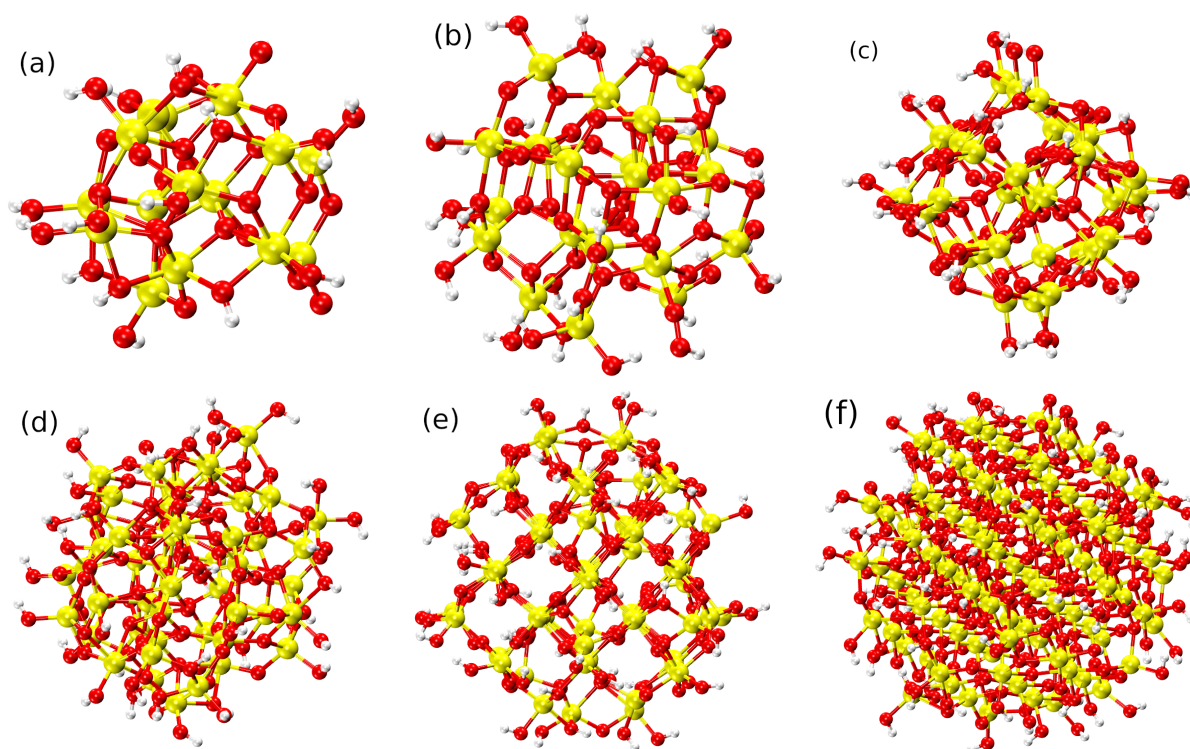


Figure 4.5: Final structure obtained after thermal treatment TT3 of modelled NPs (a) [SnO₂]₁₅, (b) [SnO₂]₂₃, (c) [SnO₂]₃₁, (d) [SnO₂]₄₈, (e) [SnO₂]₆₉, and (f) [SnO₂]₁₀₃, respectively.

Looking at the PDFs calculated on our NP models, we find that in the case of the smallest [SnO₂]₁₅ and [SnO₂]₂₃ nanoclusters, the first Sn-O peak is located at smaller distances (2.04 Å) compared to the experimental PDF (2.10 Å), indicating a shortening of the average Sn-O bond length in the smallest models. This peak is observed at 2.08 Å for [SnO₂]₃₁, approaching the position of the experimental peak. Interestingly, as the size of the NP increase the peak position aligns with the experimental one occurring at 2.10 Å in the case of [SnO₂]₄₈, [SnO₂]₆₉ and [SnO₂]₁₀₃. In the particular case of the largest [SnO₂]₁₀₃ nanocluster, the first peak shows an excellent agreement with the experimental reference, in terms of position, intensity and shape. At slightly larger distances, we observe that only two broad peaks can be identified around 3.85 Å and 4.2 Å and are shifted to larger distances compared to the experimental PDF. As the size of the NP increase, the positions of these peaks get closer to the experimental reference. In the particular case of [SnO₂]₆₉ model, these two peaks are found at distances of 3.0 Å and 3.3 Å, in good agreement with the experimental PDF, while in the case of [SnO₂]₁₀₃ model, they are found at distances of 2.96 Å and 3.27 Å, successfully reproducing the experimental peaks although with a slightly underestimated intensity. Furthermore, we observe that, in the case of the largest nanocluster several peaks arise within the distance range of 4.0 Å to 10.0 Å, exhibiting small shifts in positions compared to experiments but showing an overall good agreement to the experimental PDF.

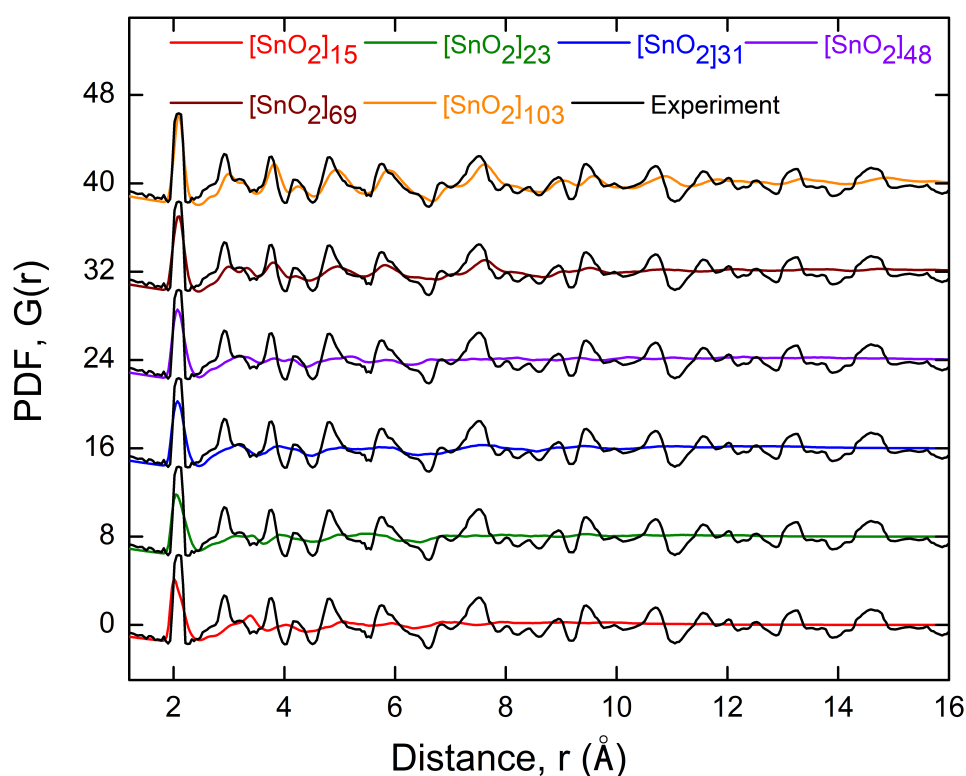


Figure 4.6: Total Neutron PDFs calculated from the 6 NP models obtained after TT3 heat treatment and compared with the experimental PDF obtained by total neutron scattering from Ref. [131].

In conclusion, the positions of the first PDF peaks in the calculated PDFs, closely resemble the experimental PDF, despite variations in intensity, as illustrated in Figure 4.6. Remarkably, the computed PDF for the larger system, [SnO₂]₁₀₃, closely aligns with the experimental PDF, replicating nearly all peaks within a 10 Å range. Nonetheless, slight deviations in the positions of the PDF peaks are observed throughout the r range.

4.3 Results and Discussions

4.3.1 Partial PDFs as a function of size of the NPs

In order to investigate the NP structure evolution as a function of their size, we calculated the partial PDFs on all our models and compared them to the partial PDFs of the bulk SnO₂ structure as illustrated in Figure 4.7. Focusing on the Sn-O correlation (Figure 4.7 (a)), we note that the first peak broadens, becomes asymmetric towards large r -values and its position shifts from 2.10 Å to 2.04 Å with decreasing nanocluster size. This shift, already observed on the total PDF, corresponds to a shortening of the average length of the Sn-O bond in the smallest models. Due to their too small size, no order in the Sn-O sub-lattice can be observed beyond 6 Å for the smallest

NPs. On the other hand, peaks are clearly visible for the [SnO₂]₁₀₃ and [SnO₂]₆₉ nanoclusters in the middle distance range. Interestingly, the [SnO₂]₁₀₃ PDF shows three consecutive peaks at distances of 3.87 Å, 4.36 Å and 5.0 Å, reproducing the same peaks appearing at slightly shorter distances in the bulk material. Other peaks are also observed at larger distances and mimic those found in the reference bulk material. Overall, the [SnO₂]₁₀₃ model exhibits a comparable Sn-O partial PDF to the bulk material at distances below 8.0 Å, despite slight variations in peak positions and intensities.

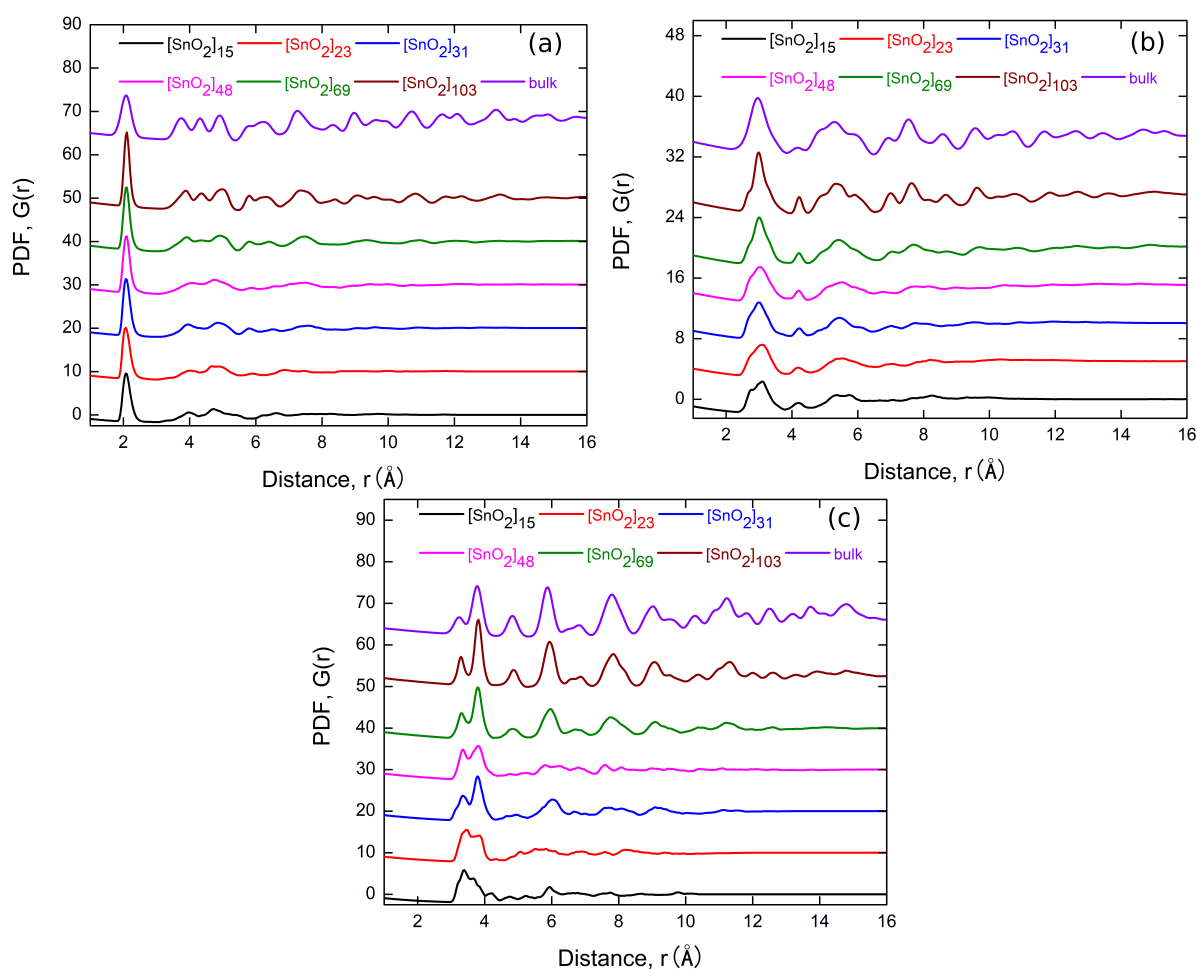


Figure 4.7: Calculated partial PDFs of (a) Sn-O, (b) O-O, and (c) Sn-Sn distances as a function of size compared with to bulk.

Looking at the O-O correlations (Figure 4.7 (b)), one notices that the first peak shows a wide broadening for small size nanoclusters ([SnO₂]₁₅ and [SnO₂]₂₃), indicative of disorder. However, as the nanocluster size increases, this peak sharpens leading to the formation of a single clear maximum. The peak observed around 4.2 Å for the smallest NP is similar to that of the SnO₂ bulk phase. In addition, we observe a broad peak in the range of around 5.36-5.72 Å in the case

of [SnO₂]₁₅ system, that when the size of the NP increases, get broader and more intense with a maxima around 5.36 Å. For the [SnO₂]₁₀₃ nanocluster, this particular peak reproduced the equivalent peak in the reference bulk phase.

Examination of the Sn-Sn partial PDF shows that the Sn sublattice undergoes the most significant changes as a function of NP size. For the largest [SnO₂]₁₀₃ model, the first two peaks located between 3 and 4 Å resemble those observed in the SnO₂ periodic structure. As the size of the NPs decreases, these two peaks undergo an inversion of the intensity ratio and a shift towards large values of r , finally resulting in a broad asymmetric peak for the smallest [SnO₂]₁₅ system. In addition, the third Sn-Sn peak at 4.7 Å, present in the periodic structure, is barely perceptible for the smallest NP models and only forms with the [SnO₂]₆₉ and [SnO₂]₁₀₃ models.

In summary, partial PDF analysis reveals that the largest nanocluster [SnO₂]₁₀₃ closely resembles the structural features of bulk SnO₂ at short and medium distances (distances less than 10 Å). However, as size decreases, distortions are clearly observed, particularly in the Sn sub-lattice. The structural origin of these changes is presented in the next sections.

4.3.2 Disentangle the core and surface of nanoclusters

In order to establish whether there is a boundary between the atoms belonging to the core and those belonging to the surface, we proceeded the same way as with the ZrO₂ system, using the Sn-O bond as a structural fingerprint. We computed the average Sn-O distance within a shell of 3 Å width. The position of this shell was shifted from the centre of the NP to the surface, thereby providing insights into the average variation of the Sn-O bond length as one approaches the NP surface. All the calculations were averaged over the last 5 ps of the considered trajectory. The results are presented in Figure 4.8.

For small [SnO₂] _{n} nanoclusters with $n=15$ and 23, the average Sn-O distances undergo a rapid decrease beyond the coordination shell of the central atom, reaching a value of approximately 2.08 Å at the NP surface, as depicted in Figure 4.8 (a). This behavior is a consequence of the small size of the NP, where the surface has a pronounced influence on the overall NP structure. Notably, in this specific scenario, both NP models undergo deformation during the thermal treatment. Consequently, a clear distinction between the core and surface atoms cannot be unambiguously devised.

In the case of models with $n=31$ and 48, Figure 4.8 shows that the Sn-O bond length shows an almost constant value around 2.15 Å up to a distance of 5 and 5.7 Å from the center of the NP, respectively, before decaying to values around 2.10 Å. Similarly, the model with $n=69$ the Sn-O bond length shows fluctuations between 2.12 Å and 2.15 Å up to a radial distance of

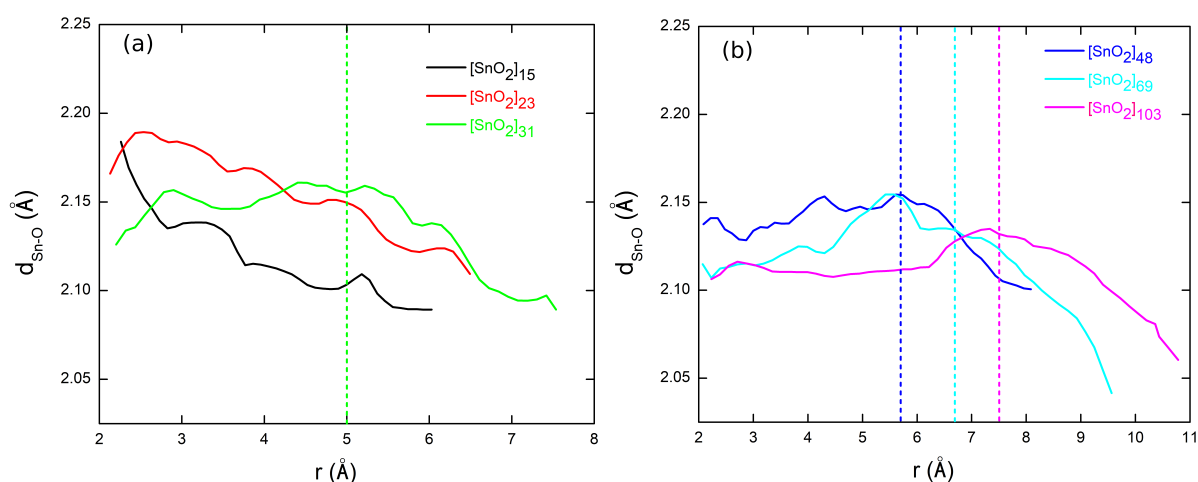


Figure 4.8: Average distances of Sn-O pairs of atoms as a function of the distance (r) from the nanoclusters center for (a) [SnO₂]₁₅, [SnO₂]₂₃, [SnO₂]₃₁ and (b) [SnO₂]₄₈, [SnO₂]₆₉, [SnO₂]₁₀₃ nanoclusters.

6.7 Å before decaying to values around 2.04 Å, whereas models with $n=103$ shows fluctuation around 2.12 Å up to 7.5 Å radial distance before decaying to values around 2.04 Å. These threshold values delimit the region starting from which the surface effects start to be important, thereby affecting the average Sn-O bond length. Interestingly, the fraction of atoms belonging to the surface is found to be 69.44 %, 70.47 %, 66.55 %, and 69.1 % for the models with $n=31$, 48, 69 and 103, respectively. As with ZrO₂, these results underline the importance of surface effects in the case of small NPs.

4.3.3 Structural properties of the core and surface atoms

Taking advantage of the defined core-surface boundary, we computed the histograms of the Sn-O, O-O and Sn-Sn distances by considering, separately, the atoms in the core and the atoms in the surface. This procedure only applies to the three largest nanoclusters. For the smallest [SnO₂]₁₅ and [SnO₂]₂₃ models, as no distinction between core and surface atoms is possible, we considered all the atoms in the NP to compute the distance histograms. The obtained histograms are compared with the partial PDFs calculated from the bulk SnO₂ structure and presented in Figure 4.9.

We can see that the histograms of Sn-O, O-O and Sn-Sn distances transform continuously from the largest to the smallest models and deviate most from those of the SnO₂ periodic structure for the smallest [SnO₂]₁₅ and [SnO₂]₂₃ nanoclusters. The most marked differences concern the Sn-Sn correlations. The two first Sn-Sn peaks located between 3 and 4 Å show both an inverted intensity ratio and a shift towards large values of r , compared with the bulk structure. As indicated in Chapter 1, the bulk structure PDF shows a first Sn-Sn peak at 3.19 Å, corresponding to Sn atoms linked by a double Sn^OSn bridge, and a second at 3.72 Å involving a single

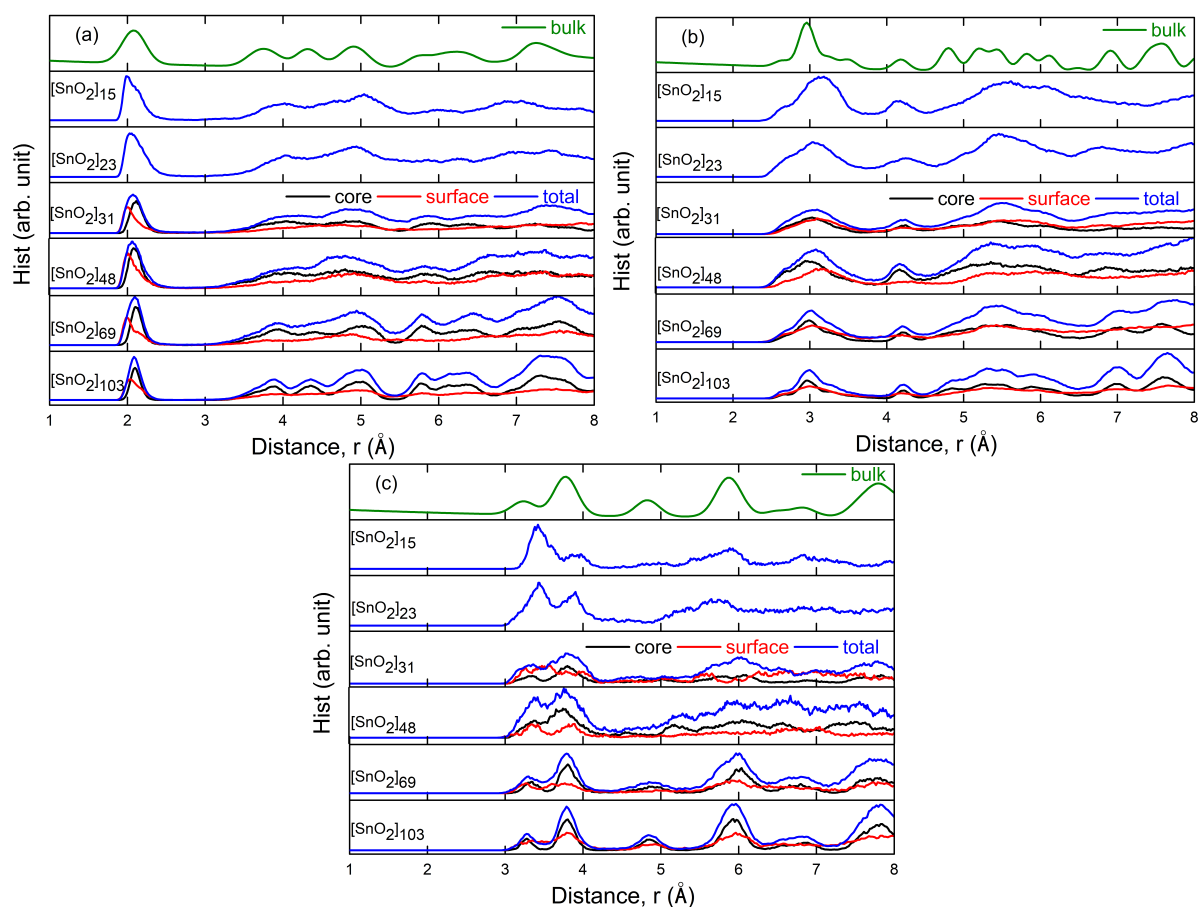


Figure 4.9: Histogram of (a) Sn-O, (b) O-O and (c) Sn-Sn distances for various sizes of nanoclusters compared with the calculated PDF of bulk SnO₂.

Sn-O-Sn bridge. The lower intensity of the first peak compared with the second can be explained by the difference in the number of double and single bridges, with a ratio of 1/4 double bridges to single bridges. Two information can therefore be deduced from the Sn-Sn histogram of the smallest models. Firstly, the ratio of double bridges to single bridges is reversed, i.e. small NPs contain far more double bridges and far fewer single bridges than the bulk structure. Secondly, the double bridges in the smallest nanoparticles are more elongated than in the periodic structure. This is illustrated in Figure 4.10 which shows a fragment of the smallest NP ([SnO₂]₁₅) with surface atoms. It can be seen that the number of double bridges is much greater than that of single bridges and that the shortest Sn-Sn distances correspond to tin atoms involved in double bridges. They have an average value close to 3.4 Å, i.e. greater than that in the bulk structure. The longest distances are observed with single bridges (with an average value of about 3.8 Å). Furthermore, it is interesting to note that as the size of the NP model increases, the intensity ratio tends to return to the ratio expected for the bulk phase. However, this evolution is clearly due to the contribution of the core atoms, whereas the contribution of the surface atoms always indicates an excess of double bridges. It is therefore the surface reconstruction of the NP that

induces the formation of an excess of elongated double bridges.

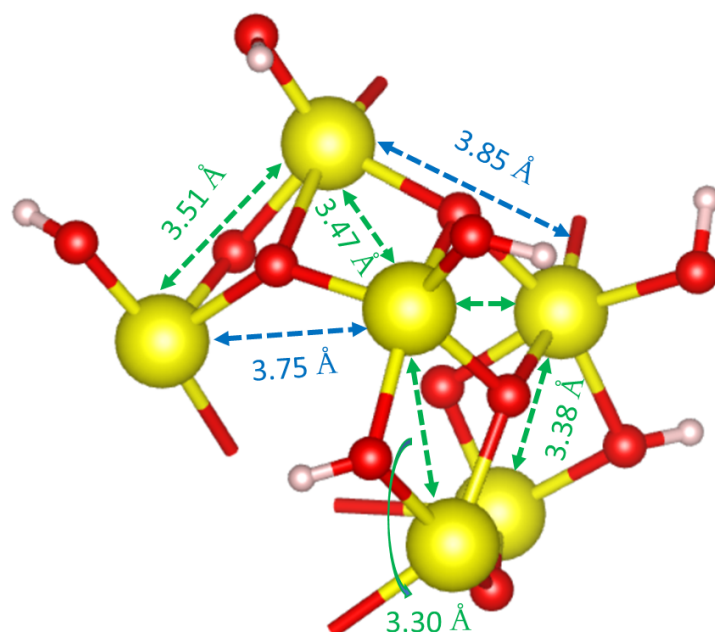


Figure 4.10: Fragment of the smallest model ([SnO₂]₁₅) with surface atoms. The length of the double bridges is indicated by green arrows and that of the single bridges by blue colors.

The Sn-Sn histogram also shows that the third Sn-Sn peak, at 4.7 Å, clearly present in the periodic structure, is barely perceptible for the smallest NP models and only forms with the [SnO₂]₆₉ and [SnO₂]₁₀₃ models. This peak corresponds to Sn-Sn distances involving three tin atoms in two consecutive single Sn-O-Sn-O-Sn bridges. We therefore expect the disorder induced by the surface reconstruction to induce much greater variability in these Sn-Sn distances, giving rise to an almost flat peak for the smallest NP models.

Looking now at the Sn-O histograms, we see that for the smallest model, the first peak is very asymmetric, with a shoulder on the right-hand side, and a maximum at 2.00 Å, i.e. a shorter distance than the 2.10 Å for the bulk structure. As the size of the NP increases, this peak turns into an almost symmetrical peak at the same time as it moves towards larger r values. This has already been noticed with the partial PDF analysis. However, we can now see that the surface atoms are responsible for this behaviour. Indeed, we can see that for the models [SnO₂]₃₁, [SnO₂]₄₈, [SnO₂]₆₉ and [SnO₂]₁₀₃, the atoms in the core region make a constant contribution to the first peak, with an almost symmetric peak located at around 2.10 Å, i.e. the distance found in the bulk structure. In contrast, the surface atoms give an asymmetric peak with a maximum at 2.00 Å, with a decreasing contribution as the size of the NP increases. The average length of the Sn-O bond is therefore shorter only for the surface atoms; the reconstruction of the surface

does not affect the length of the Sn-O bond in the core. It can also be noted that as the size of the nanocluster increases, the histogram of the core atoms shows the appearance of several peaks at greater distances, reminiscent of the bulk structure, whereas the histogram of the surface atoms shows a flat distribution with barely visible peaks, highlighting much greater positional disorder at the surface than at the core.

Looking finally at the O-O histograms, we can see that the correlation peaks from the core atoms become sharper with increasing nanocluster size. However, the atoms belonging to the surface show a substantial broadening of their peaks, whatever the size of the nanoclusters, which again emphasises that the surface atoms show more positional disorder.

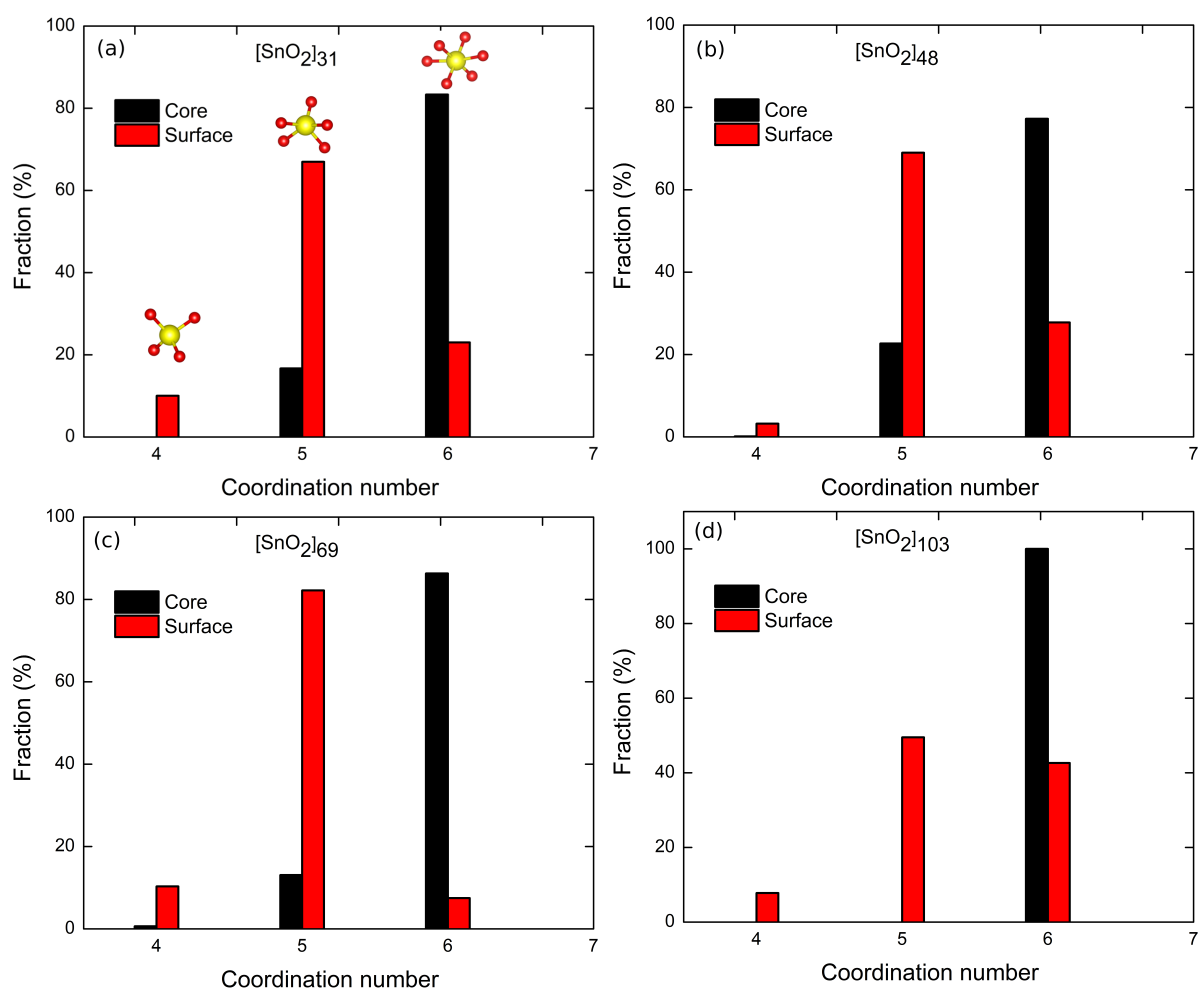


Figure 4.11: Fraction of coordination number of Sn-atoms within the core and the surface for (a) [SnO₂]₃₁, (b) [SnO₂]₄₈, (c) [SnO₂]₆₉ and (d) [SnO₂]₁₀₃ nanoclusters.

To complete the above analysis, we studied the environments of the Sn atoms in the core and on the surface of the nanoclusters. It is note that we use Sn-O bond length cutoff value is 2.5 Å.

Figure 4.11 displays the distribution of different local Sn environments found in the core and surface regions of SnO₂ nanoclusters of varying sizes. Specifically, the core Sn environment predominantly exhibits a high proportion of 6-fold environments similar to the bulk phase, whereas the Sn surface local environments predominantly exhibit a high proportion of 5-fold geometry, which is less than that of the bulk's 6-fold geometry. This trend is consistent across all nanocluster sizes. Notably, in the case of [SnO₂]₁₀₃ nanocluster, the Sn environment within the core comprises 100% 6-fold coordinated atoms, while the surface exhibits a mixture of 5-fold and 6-fold coordinated atoms, with a higher proportion of the former. These findings confirm that the core of larger nanoclusters is nearly crystallized and demonstrates a bulk-like structure, while the surface exhibits distortions indicative of disordered structure. The lower Sn coordination at the surface is in line with the shortest Sn-O bond lengths at the surface compared to the core region, as discussed in the preceding paragraphs.

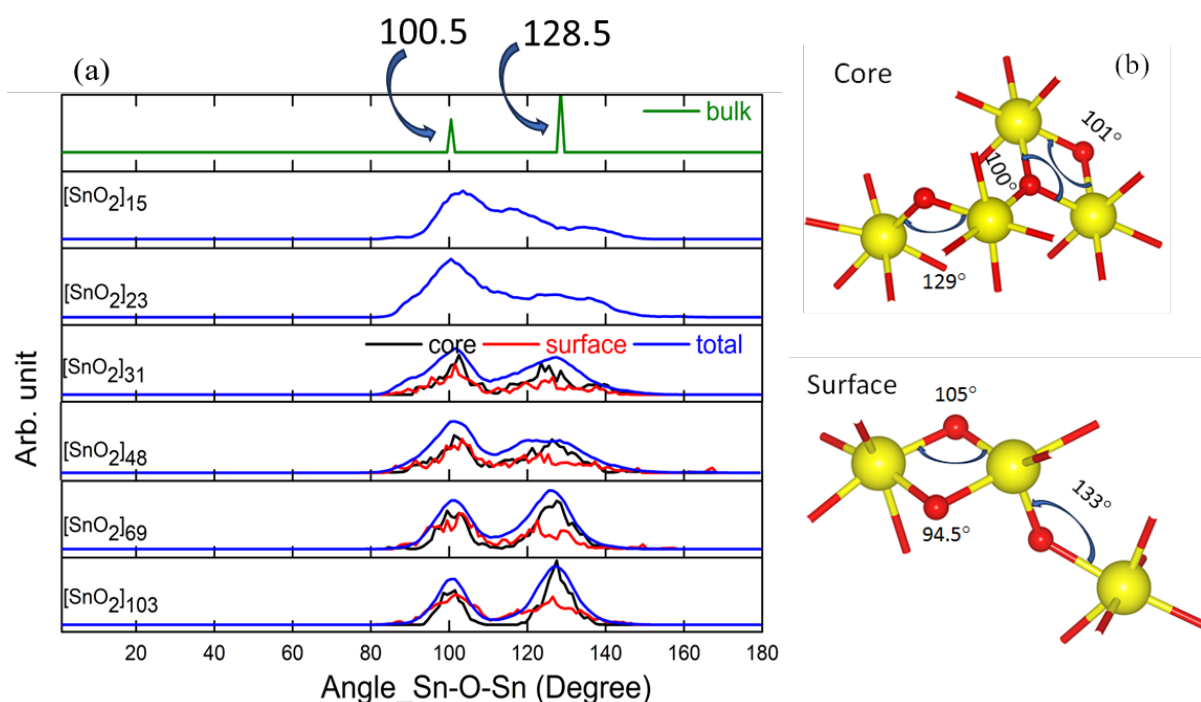


Figure 4.12: (a) Sn-O-Sn angle distribution from the core and surface of nanoclusters compared with the bulk. (b) An example of the angle distribution from a small fragment of the nanocluster core and surface.

Similarly, the Sn-O-Sn angle distributions are calculated for all sizes of nanoclusters and compared with bulk SnO₂, as shown in Figure 4.12. In the bulk, the two peaks at 100.5° and 128.5° correspond to two different bridges. The first peak, which is less intense, is due to Sn-O-Sn double bridges, while the second peak is associated with Sn-O-Sn single bridges. As previously discussed (in the distance histogram analysis), the intensity difference between the two peaks is due to the varying numbers of double and single bridges. For small nanoclusters, the angle

distribution is broader compared to the bulk, indicating structural distortion. As the nanocluster size increases, the two angles from the nanocluster core become clearly separated, resulting in two distinct peaks for the average Sn-O-Sn angle at 100° and 130°, respectively. These two peaks are evident in larger nanoclusters ([SnO₂]₁₀₃), with different intensities that closely match the bulk. However, angles due to surface atoms show a wide distribution and lower intensities, differing from the bulk characteristics. This is illustrated in the schematic diagram in Figure 4.12 (b), which highlights the differences between the nanocluster core and surface. Therefore, this analysis confirms that while the nanocluster core retains a crystallized, bulk-like structure, the surface shows distortions and deviates from the bulk-like structure.

4.3.4 Comparison of local environments of core and surface atoms for ZrO₂ and SnO₂ nanoclusters

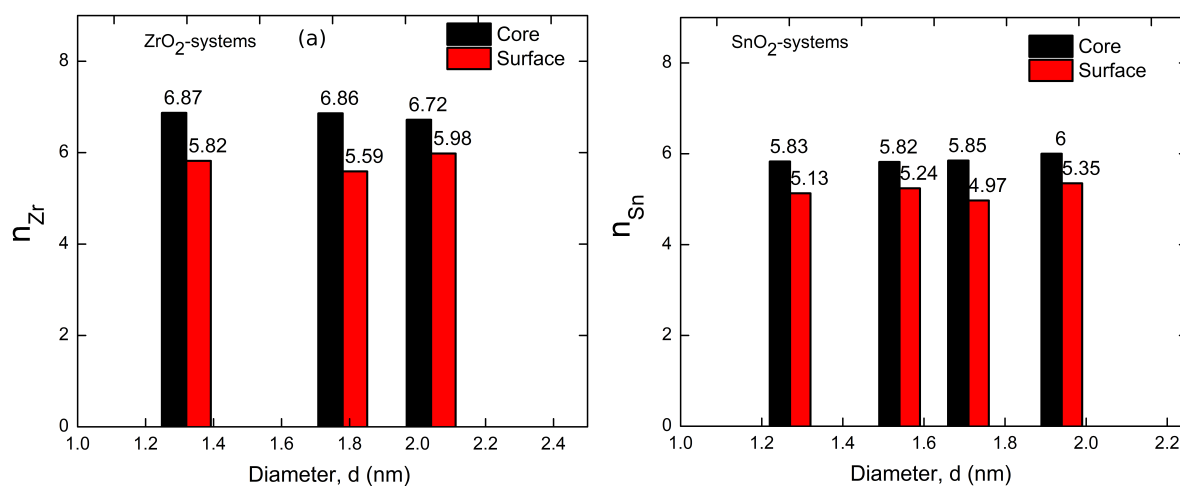


Figure 4.13: Average coordination number of Zr atoms in the core and those at the surface for (a) ZrO₂ and (b) SnO₂ systems.

Additionally, we compare the average coordination numbers for Zr and Sn in both the core and the surface regions and plot the results as a function of NP size as illustrated in Figures 4.13 (a) and (b). These calculations are performed by considering a distance cutoff of 2.5 Å. Specifically, in ZrO₂ systems, the Zr atoms within the core exhibit an average coordination number of approximately 7, whereas those on the surface predominantly demonstrate coordination number around 6. Conversely, in SnO₂ systems, the average coordination number within the core is 6, while the surface predominantly displays a 5-fold coordination number. The core in ZrO₂ systems exhibits an even lower coordination number compared to the cubic phase; however, in SnO₂ systems, the core maintains an average coordination number of around 6, equivalent to bulk SnO₂. Conversely, the surface atoms in both systems exhibit a lower coordination compared to the bulk configuration.

4.4 Conclusions

In this chapter, we initially construct several nanocluster models of varying sizes from 0.98 nm to 1.94 nm. It was observed that the surface of said nanoclusters exhibits Sn and O dangling bonds. In order to avoid these dangling bonds, we have placed water molecules on top of the surface Sn-atoms of nanoclusters. In this work, Quantum MD simulations at different temperatures were performed in order to study the structure and electronic properties of modelled SnO₂ nanoparticles. In particular, we found that the nanoclusters surface formed oxygen dimers and trimers. We adopt a complementary passivation procedure in which we recover a system snapshot at $T = 750$ K where some water molecules start to move away from the surface and identify the neighboring under-coordinated O and Sn atoms. Subsequently, we manually split those flying water molecules into H and OH, and position them on the surface O of Sn atoms, respectively. This approach result in 100 % surface passivation of our models where all the O-O surface defects are removed. Furthermore, we have calculated PDFs based on neutron total scattering using TT3 and subsequently compared them with the corresponding experimental PDF. In particular, the PDF calculated for the large system ([SnO₂]₁₀₃) closely resembles the experimental PDF, with nearly all peaks being reproduced. This agreement is particularly evident up to a distance of 8.0 Å, indicating a strong correspondence between the calculated and experimental PDFs. Notably, it is observed that the calculated PDF peaks shift their positions towards larger distance values as well as less in intensities in comparison with experiment throughout the nanoclusters. Additionally, we computed the partial PDFs for each size of the modeled nanoclusters and subsequently compared them with the PDFs of the corresponding bulk materials. The analysis of Sn-O, O-O, and Sn-Sn PDFs reveals that the [SnO₂]₁₀₃ nanocluster exhibits a structural configuration closely resembling bulk SnO₂ concerning short and medium-range distances, particularly those distances below 10 Å. Furthermore, we examined the Sn-O bond length as a function of distance (r) from the central atom to distinguish between the core and surface of the nanoclusters. Our findings indicate that the Sn-O bond length of atoms in the core maintains a constant value up to a certain distance and then rapidly decreases towards the surface of the nanoclusters. Subsequently, we calculated the histograms for Sn-O, O-O, and Sn-Sn distances for atoms in the core and the surface. In particular, Sn-Sn histograms indicating the presence of double and single bridges between Sn atoms. The lower intensity of the peak corresponding to double bridges is explained by their lower abundance compared to single bridges. Interestingly, the study of the smallest nanoparticles reveals a reversal in the ratio of double to single bridges, with nanoparticles containing more double bridges. Additionally, these double bridges exhibit greater elongation compared to those in the bulk structure. Overall, our observations reveal that atoms in the core closely resemble bulk SnO₂, while surface atoms exhibit a disordered structure compared to the bulk material. In the final analysis, we determine the fraction of coordination numbers of Sn-atoms within the core and on the surface of nanoclusters. It seems that there is a

high fraction of coordination number exhibited by Sn-atoms in the core, which is 6, mirroring that of the bulk, whereas the surface displays a lower coordination number.



5

Electronic properties of ZrO₂ and SnO₂ NPs with their comparison

Summary

5.1	Electronic properties of ZrO ₂ systems	110
5.1.1	Density of states of bulk ZrO ₂	110
5.1.2	DOS of whole nanoparticle models	112
5.1.3	Core and Surface atoms contribution to the total DOS	118
5.2	Electronic properties of SnO ₂ nanoparticles	122
5.2.1	Density of states of bulk SnO ₂	122
5.2.2	DOS evolution as a function of size of the nanoclusters	125
5.2.3	Core and surface atoms contribution to the total DOS	127
5.3	Comparison of electronic properties between ZrO ₂ and SnO ₂ NPs	130
5.4	Conclusions	131

This chapter focuses on the study of the electronic properties of ZrO_2 and SnO_2 NP models by examining the total and partial densities of states. The influence of NP size (quantum confinement), as well as that of core and surface atoms, on the electronic properties will be discussed. A comparison of the electronic properties of the ZrO_2 and SnO_2 systems will also be presented.

5.1 Electronic properties of ZrO_2 systems

5.1.1 Density of states of bulk ZrO_2

The previous chapters showed that achieving good NP models, consistent with experimental data, requires a proper surface passivation procedure together with an adequate thermal treatment. This allows the surface atoms to reorganize and relax, leading for larger NPs to the formation of a core-shell structure with different structural fingerprints. To study the effect of this particular structure on electronic properties, we calculated, at different levels of theory, the total (TDOS) and partial (PDOS) densities of states and band gap widths of NP models and compared them with those of cubic and monoclinic polymorphs of zirconia. For each NP model, TDOS and PDOS calculations were averaged over 10 snapshots taken from the last 5 ps of the MD trajectory.

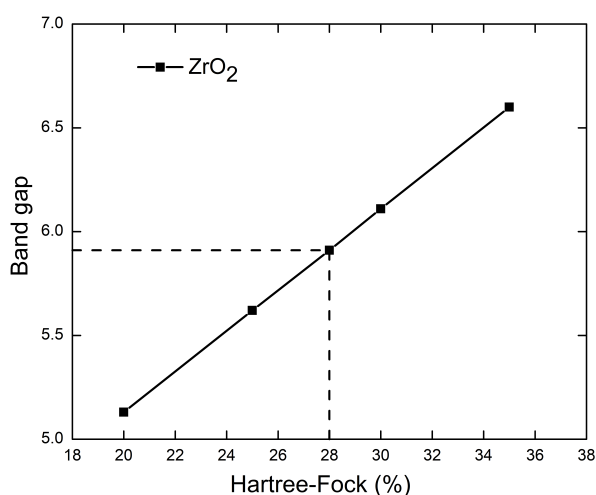


Figure 5.1: Evolution of band gap with the fraction of Hartree-Fock exchange.

Using the PBE exchange and correlation functional, the calculated band gap of the cubic polymorph is 3.26 eV. This value is well below the reported experimental values, which range from

5.7 to 6.0 eV [132]–[136]. This discrepancy is a well-known problem in DFT calculations, considering GGA exchange correlation functionals. This difference can be corrected by resorting to a hybrid functionals comprising a fraction α of the exact Hartree–Fock exchange are known to improve the description of the electronic structure of the material. The use of the PBE0 [108], [109] functional with an optimised α value of 0.28 (Figure 5.1) allowed us to calculate a band gap value of 5.91 eV, in close agreement with the experimental value. The same configuration used for monoclinic zirconia gave a band gap value of 6.09 eV (compared with 3.58 eV with PBE), in good agreement with the experimental values, which range from 5.8–7.09 eV [132]. Accordingly, the hybrid functional electronic structure calculations on the NP models were carried out with this optimized setup.

The TDOS and PDOS of monoclinic and cubic zirconia calculated using PBE and PBE0 are shown in Figure 5.2 and 5.3. We can see that the two functionals give very similar DOS profiles. In addition, the DOS profiles of the cubic and monoclinic polymorphs are relatively close. Slight shifts towards higher energies are observed for the monoclinic phase. In particular, the conduction band of the monoclinic phase shifts to higher energy values than that of the cubic phase, resulting in a larger energy band gap.

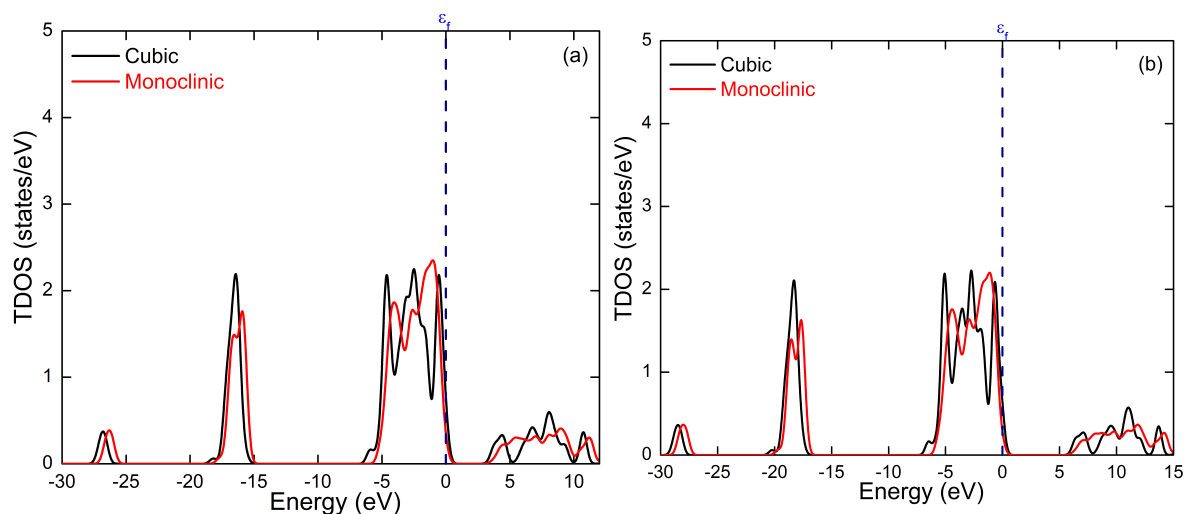


Figure 5.2: Total density of states (TDOS) obtained for the cubic and monoclinic polymorphs of zirconia using PBE (a) and PBE0 (b) approximations.

The PDOS plots show that for both phases the valence band is mainly made up of the p orbitals of O atoms and that the Zr-d orbitals are mainly responsible for the conduction band. These results are consistent with the computed HOMO (highest occupied molecular orbitals) and LUMO (lowest unoccupied molecular orbitals) orbitals of the cubic phase, shown in Figure 5.4. We find that the HOMO is mostly localized on the O sites, displaying p-state character, with a

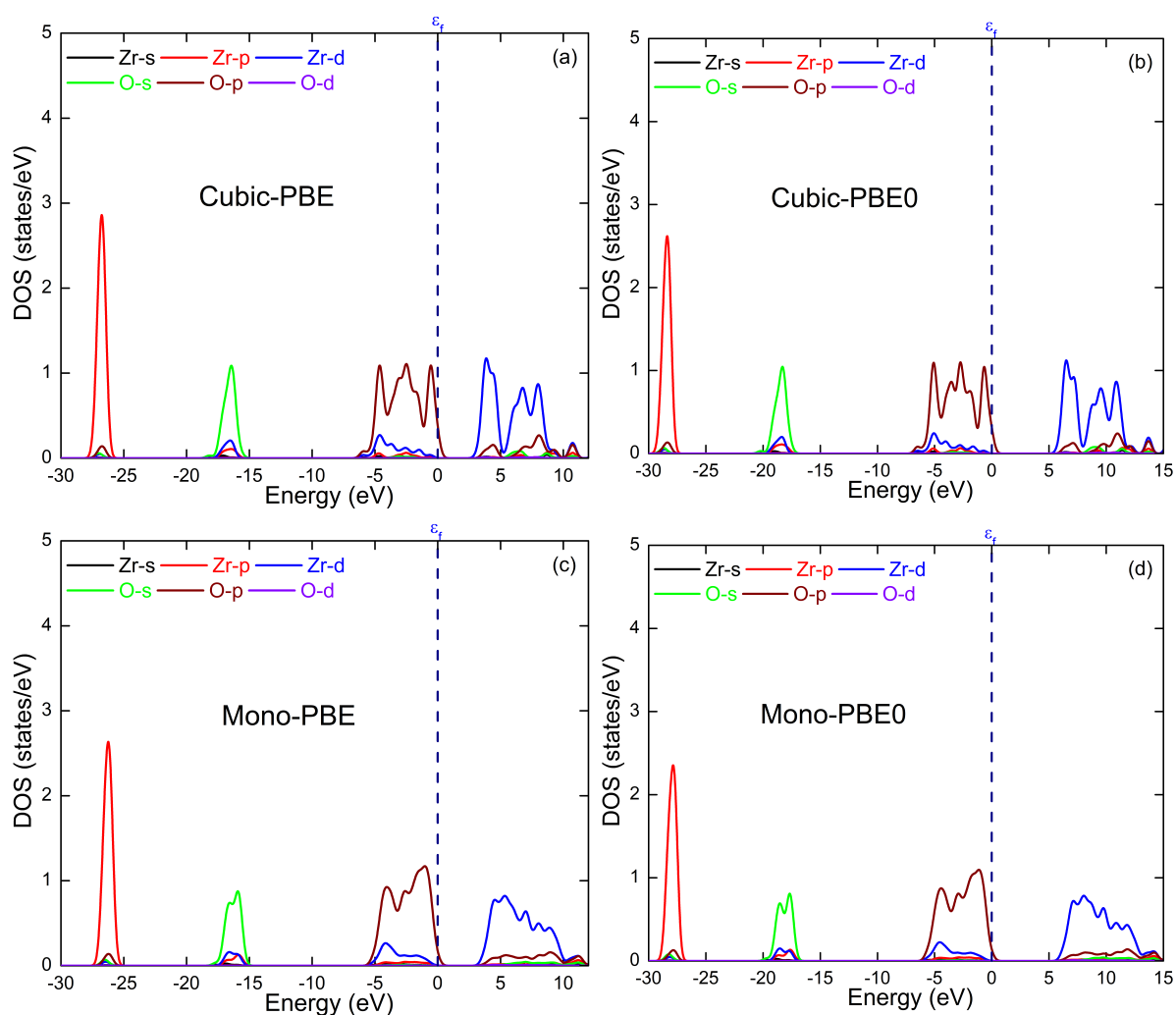


Figure 5.3: Partial density of states (PDOS) obtained for the cubic zirconia using PBE (a) and (b) PBE0 functional. Similarly, PDOS obtained for monoclinic polymorph using (c) PBE and (d) PBE0 approximations.

small portion of Zr sites, whereas the LUMO are mostly localized on Zr sites, displaying d-state character, and a small portion of O sites displaying p-state character.

5.1.2 DOS of whole nanoparticle models

We have calculated the PDOS and TDOS for the different NP models with maximum passivation rate. Results are presented in Figure 5.5, with each DOS in full scale and in Figure 5.6, with all DOS on the same scale. The very minor contributions from H atoms are not included.

We observe that the DOS of the NP reproduces the main bands of that calculated on the bulk

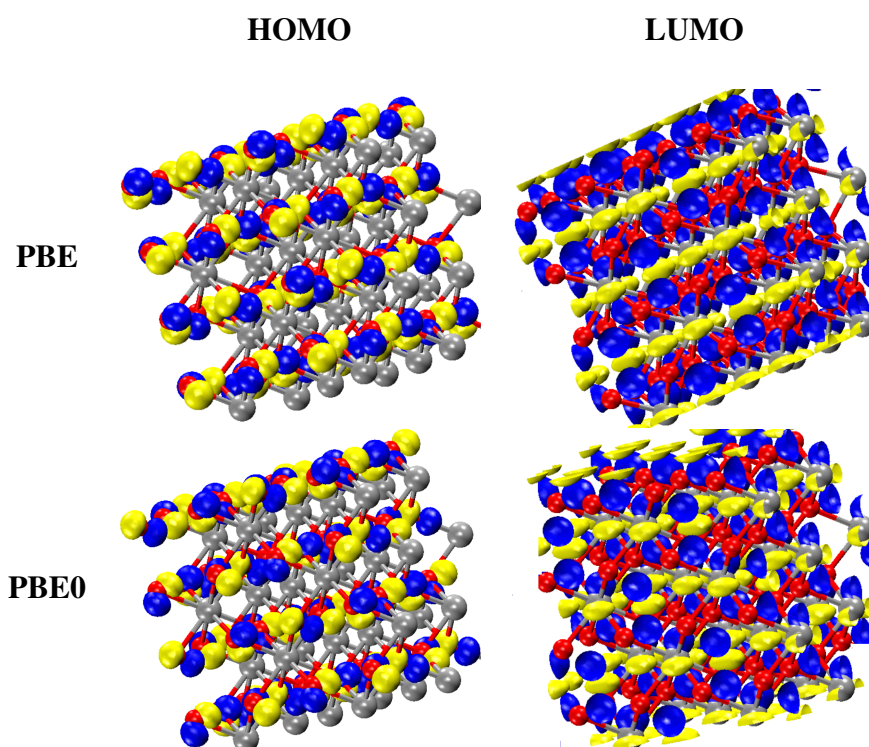


Figure 5.4: Molecular orbitals (MOs) plot for HOMO and LUMO of the cubic phase zirconia using PBE and PBE0 functionals by considering the isosurface value of 2 %. Zr atoms in grey balls and O atoms in red balls.

material. This is particularly true for the large NP ($[\text{ZrO}_2]_{141}$) where we see that the overall relative peak intensity is respected. The NP DOS bands show a slight broadening compared to that of ZrO₂ polymorphs reflecting the structural disorder of the NP structure. Interestingly, the shape of the valence bands of the NPs is clearly asymmetric, with a bump on the higher-energy side, which more closely resembles the envelope of the monoclinic polymorph. This is observed for all model sizes and can be related to the monoclinic distortions present in the structure and described in Chapter 3. Furthermore, the absence of defect levels in the band gap of the NPs reflects the effectiveness of our passivation procedure in eliminating surface defects. It can be noted that the same calculations performed with the lowest passivation rate (16.7%) led to a defect level in the band gaps and a narrowing of the band gaps, as shown in Figure 5.7.

The band gap widths of the NP models (E_g^{NP}) calculated with a maximum passivation rate are given in Table 1, together with their standard deviations. Their differences (ΔE_g) with respect to the band gap of the cubic polymorph (E_g^{bulk}) are plotted as a function of NP size in Figure 5.8. One clearly observes an increase in the band gap values when the diameter of the nanoclusters decreases, reflecting the occurrence of quantum confinement effects in ZrO₂ NPs. The figure also shows that for the models with a lower surface passivation rate down to 33%, the band gap values remain close to those achieved with maximum surface passivation. However, a considerably

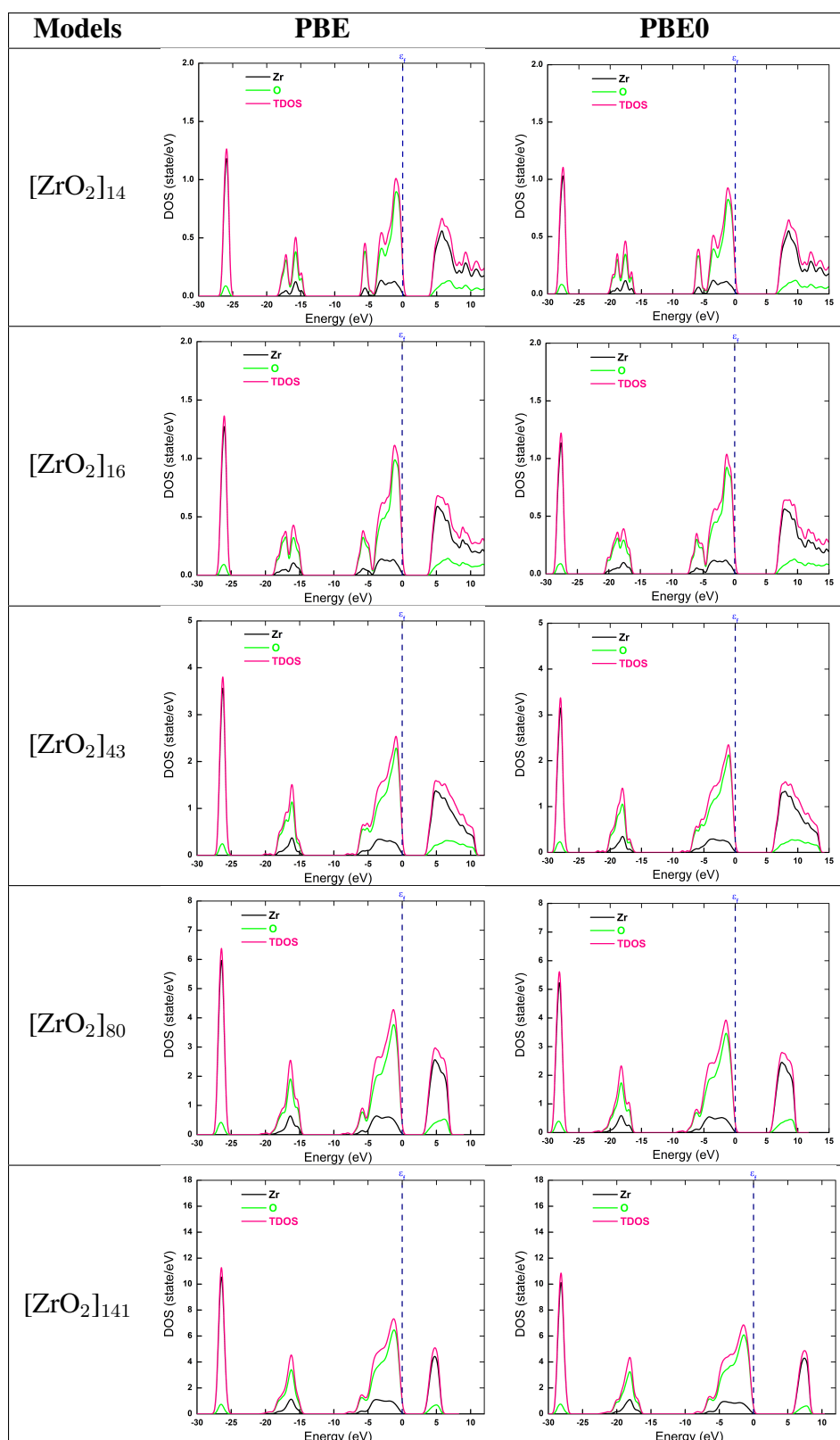
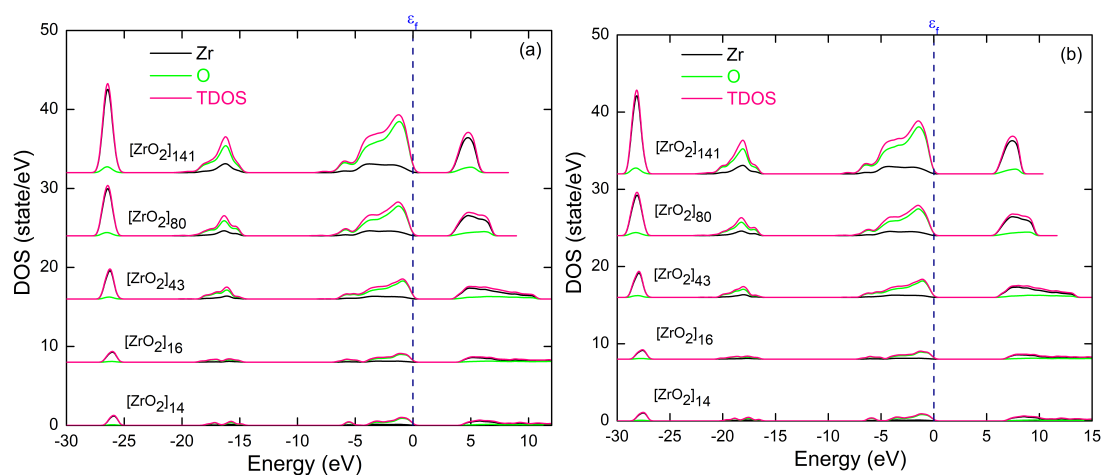


Figure 5.5: Partial and total density of states of ZrO₂ nanocluster models with maximum passivation rate using PBE and PBE0 approximations.

Table 5.1: Calculated band gap of zirconia models along with their standard deviation (\pm) using PBE and PBE0 functionals

Band Gap \pm standard deviation (eV)		
Models	PBE	PBE0
c-ZrO ₂ (bulk)	3.26	5.91
m-ZrO ₂ (bulk)	3.58	6.09
[ZrO ₂] ₁₄ .8H ₂ O	4.37 \pm 0.05	6.98 \pm 0.06
[ZrO ₂] ₁₆ .12H ₂ O	4.20 \pm 0.07	6.85 \pm 0.07
[ZrO ₂] ₄₃ .24H ₂ O	3.76 \pm 0.05	6.26 \pm 0.05
[ZrO ₂] ₄₃ .8H ₂ O	3.53 \pm 0.04	6.03 \pm 0.04
[ZrO ₂] ₄₃ .4H ₂ O	1.37 \pm 0.04	3.62 \pm 0.05
[ZrO ₂] ₈₀ .26H ₂ O	3.43 \pm 0.05	5.90 \pm 0.05
[ZrO ₂] ₁₄₁ .54H ₂ O	3.57 \pm 0.06	6.06 \pm 0.03
[ZrO ₂] ₁₄₁ .18H ₂ O	3.48 \pm 0.02	5.92 \pm 0.03
[ZrO ₂] ₁₄₁ .9H ₂ O	2.71 \pm 0.07	5.06 \pm 0.04

**Figure 5.6:** Partial and total density of states for NP models [ZrO₂]_n, n = 14, 16, 43, 80 and 141 with maximum passivation rate represented on the same scale: (a) PBE and (b) PBE0.

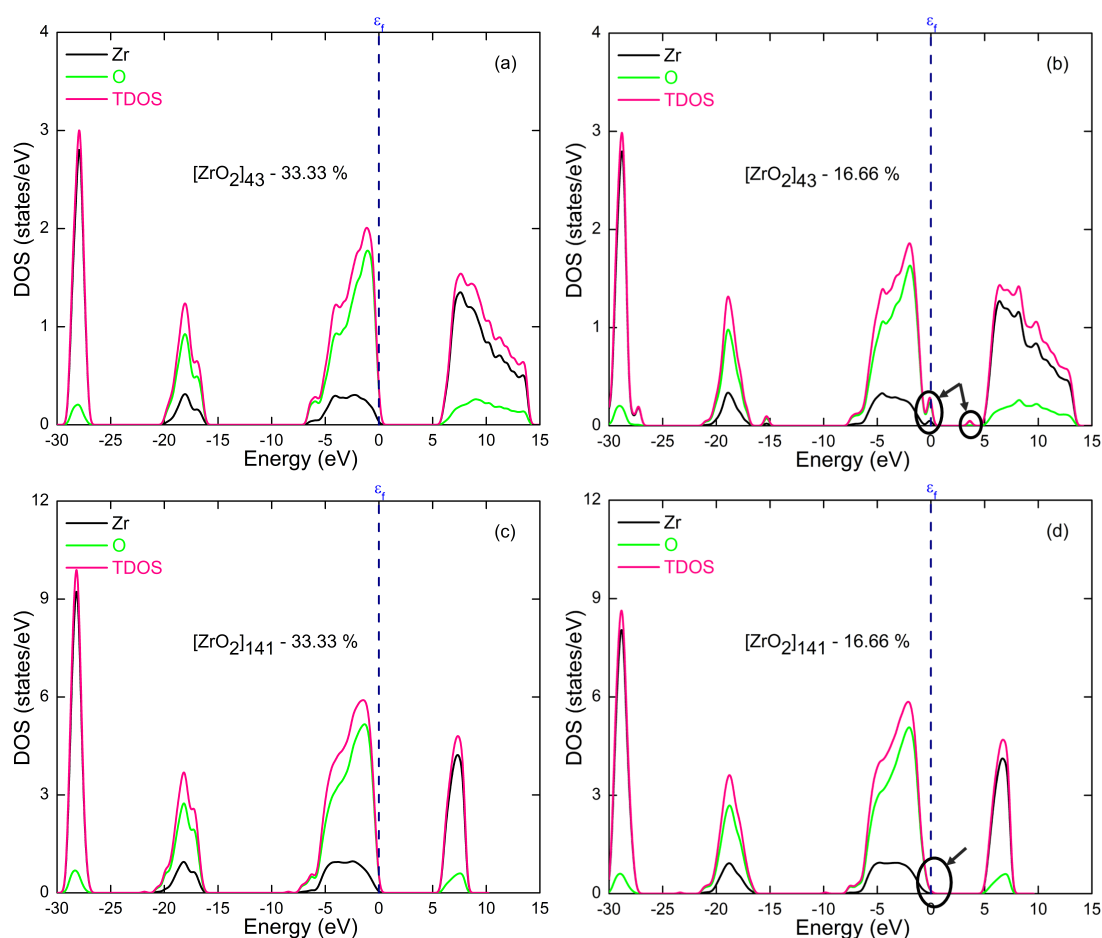


Figure 5.7: PDOS for partially passivated nanoparticles with 33.33 % and 16.66 % surface passivations (a), (b) for [ZrO₂]₄₃ and (c), (d) for [ZrO₂]₁₄₁ nanoclusters, respectively.

smaller band gap is obtained in the case of 16.66% surface passivation. This behaviour is related to the presence of surface defects that remain unpassivated when a low coverage of the NP surface is used. Two types of defects have been identified: the first type is band edge defects caused by oxygen atoms, while the second type is mid-gap states attributed to zirconium atoms. These defects can clearly be seen in the DOS for [ZrO₂]₄₃ and [ZrO₂]₁₄₁ nanocluster with 16.66 % surface passivation, as depicted in Figure 5.7.

In order to estimate more quantitatively the variation of band gap with NP size, the data were fitted with a well-known expression used for a wide variety of quantum dots [81], [82], [84], [87]: $\Delta E_g = E_g^{NP} - E_g^{bulk} = \beta/d^\alpha$, where d is the NP diameter and α and β are parameters that define the strength of the quantum confinement. The fit is also shown in Figure 5.8 and yields the following values: $\alpha = 1.738$, $\beta = 0.917$ for PBE and $\alpha = 2.782$, $\beta = 0.860$ for PBE0. The effect of the functionals seems relatively weak on β but more significant on α , with a clearly higher value using PBE0.

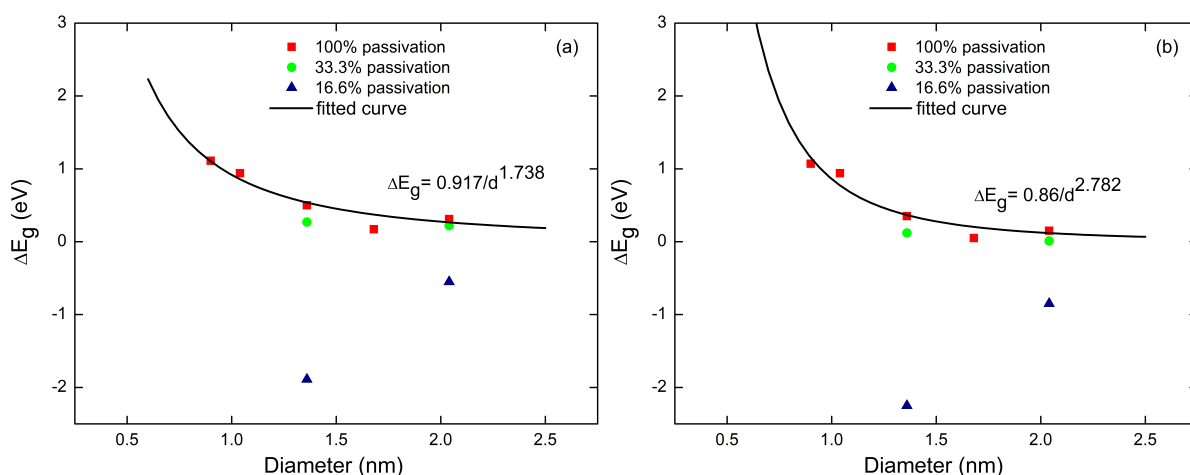


Figure 5.8: Computed energy band gap difference of NPs relative to that of the bulk material $\Delta E_g = E_g^{NP} - E_g^{bulk} = \beta/d^\alpha$ as a function of the NPs size. The solid lines are the fitted curves: $\Delta E_g = 0.917/d^{1.783}$ and $\Delta E_g = 0.86/d^{2.782}$ for (a) PBE and (b) PBE0 approximations.

By looking at literature on quantum dots (CdSe, CdS, CdTe, InP, InAs, ZnSe, ZnO, GaN, InN, SnO₂, etc.) [7], [81], [82], [84], [87], [89], these parameters, were found to range between 1 and 2.3 for α , and from 1.7 to 4.5 for β . The value of alpha is around that expected from the effective mass approximation model, which predicts that the energy band gap decreasing scale is proportional to d^{-2} with effective diameter increases [8]. Overall, these values reflect a relatively low quantum confinement effects in ZrO₂, which might be explained by the large effective mass of electrons resulting from the material's large band gap [81].

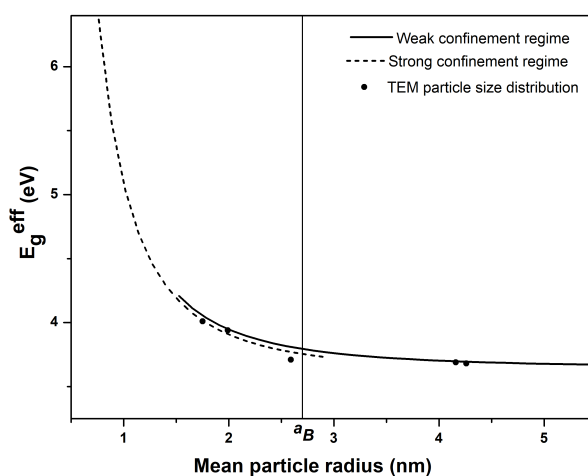


Figure 5.9: Evolution of experimental band gap as a function of SnO₂ particle size. Extracted data from Ref. [7]

For comparison, we extracted the band gap data from the earlier experimental findings on

SnO₂ systems in Ref. [7] and found α and β to be 2.27 and 1.48, respectively, exhibiting a trend closely resembling to our own results. The evolution of extracted experimental band gap as a function of SnO₂ particles size is shown in Figure 5.9, where a_B is the exciton Bohr radius, found to be 2.7 nm.

5.1.3 Core and Surface atoms contribution to the total DOS

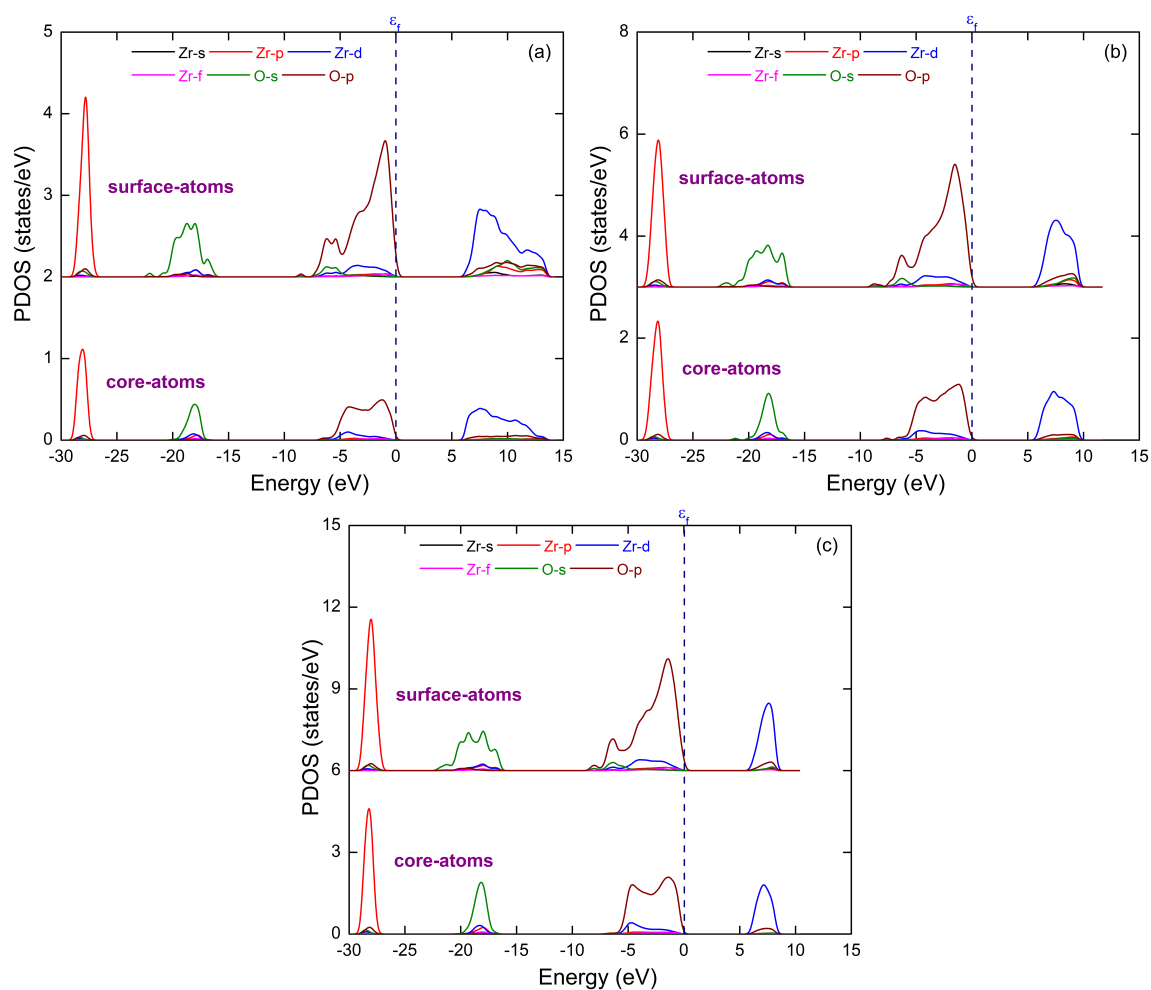


Figure 5.10: Partial density of states (PDOS) for the atoms in core and surface of (a) [ZrO₂]₄₃, (b) [ZrO₂]₈₀ and (c) [ZrO₂]₁₄₁ nanoclusters with maximum surface passivation. PDOS of surface atoms are shifted vertically for clarity.

Given the core-shell structure of NP, we here project the DOS into the atoms belonging to the core and the surface regions of [ZrO₂]₄₃, [ZrO₂]₈₀, and [ZrO₂]₁₄₁ nanoclusters with maximum surface passivation, as shown in Figure 5.10. Overall, we observe that the surface atoms lead to broader peaks and higher intensities of all the PDOS bands compared to the core atoms. This behaviour is particularly pronounced at the vicinity of the Fermi level where we see a higher

contribution of the p orbitals in the surface atoms compared to the core ones which can be correlated with the higher number of surface atoms compared to the core.

It is interesting to note that the core atoms lead to a relatively flat valence band DOS profile that is more similar to that of the cubic polymorph of ZrO₂. In contrast, the valence band DOS profile from the surface atoms is highly asymmetric, more reminiscent of the monoclinic polymorph. However, despite these major differences in shape, the electronic band gap due to the core and surface atoms leads to the same value.

The HOMO and LUMO orbitals calculated with PBE0 functionals for [ZrO₂]₄₃, [ZrO₂]₈₀ and [ZrO₂]₁₄₁ models are shown in Figure 5.11. We find that, the HOMO is mostly localized on the O sites, displaying p-state character whereas the LUMO are mostly localized on Zr sites, displaying d-state character.

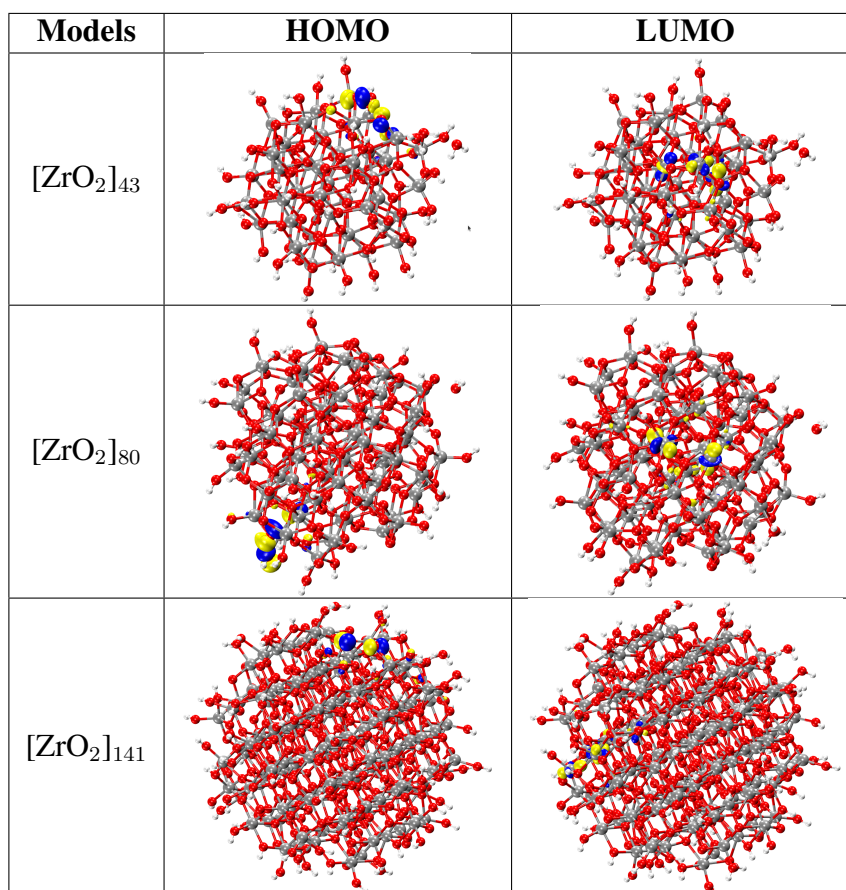


Figure 5.11: Molecular orbitals (MOs) plot for HOMO and LUMO of the [ZrO₂]_n, n=43, 80 and 141 with 100 % surface passivation using PBE0 functionals. The isosurfaces are shown in yellow and blue, representing values of +0.06 and -0.06, respectively.

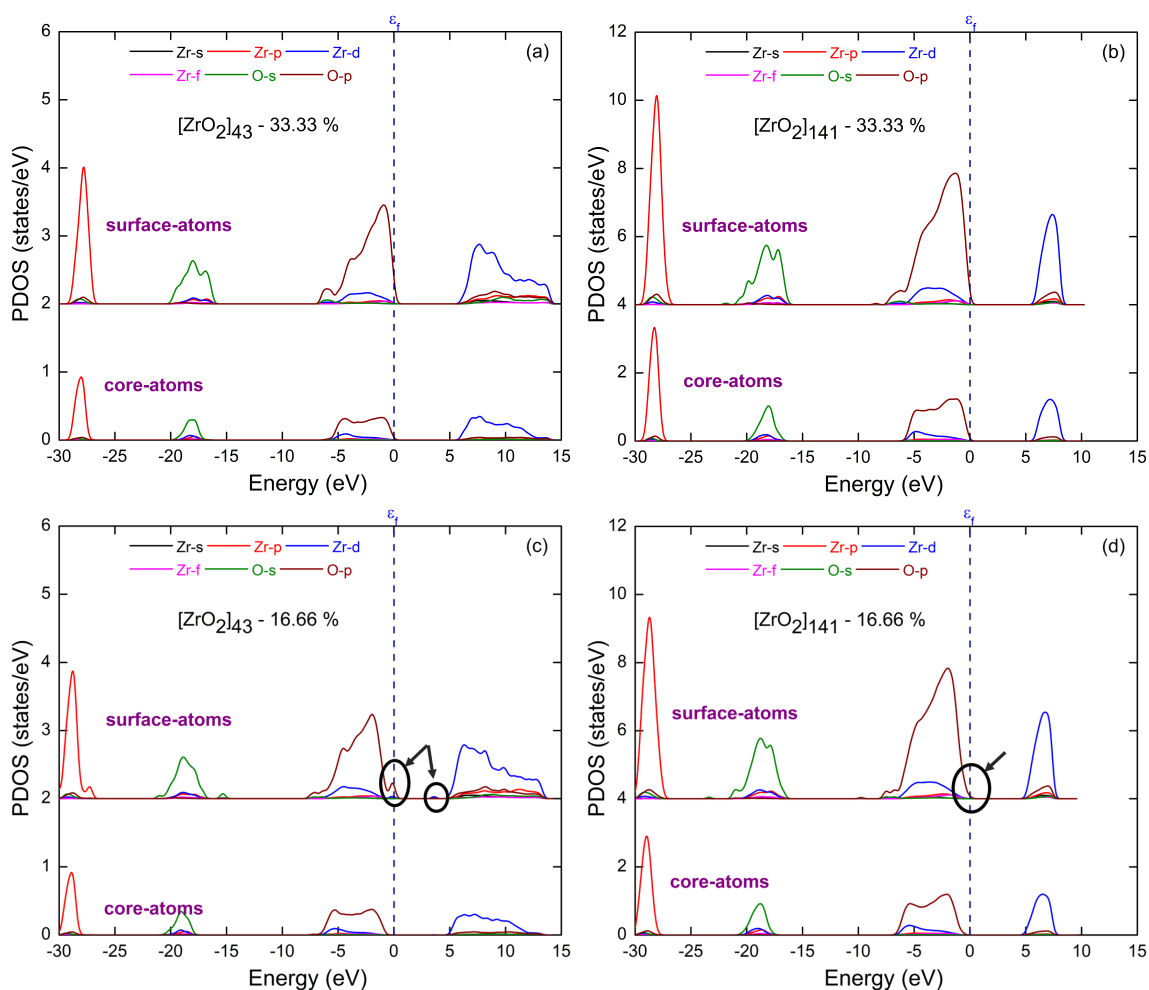


Figure 5.12: Partial density of states (PDOS) for the atoms in core and surface of [ZrO₂]₄₃ and [ZrO₂]₁₄₁ nanoclusters with 33.33 % (a, b) and 16.66 % (c, d) surface passivation. PDOS of surface atoms are shifted vertically for clarity.

For comparison, the PDOS of atoms belonging to the core and surface regions for [ZrO₂]₄₃ and [ZrO₂]₁₄₁ models with lower (33.3 % and 16.7 %) passivation rate are depicted in Figure 5.12. With 33.3 % surface passivation, the DOS profile remains consistent with those obtained with maximum passivation. However, with 16.7 % surface passivation for [ZrO₂]₄₃ (see Figure 5.12 (c)), the surface atoms shows a displacement of the valence band maxima (VBM) towards the higher energies compared to the VBM of the atoms in the core, and the appearance of a mid-gap state. This is due to the localized defects at the surface, results in the reduction of the band gap. For [ZrO₂]₁₄₁ with 16.7 % passivation, a displacement of O-2p band at the valence band for atoms at the surface compared to the core atoms, leading to slight closure of the band gap.

The HOMO and LUMO for NPs [ZrO₂]₄₃ and [ZrO₂]₁₄₁ with 33.33 % and 16.66 % surface

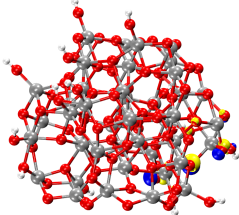
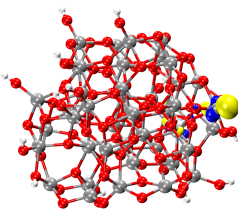
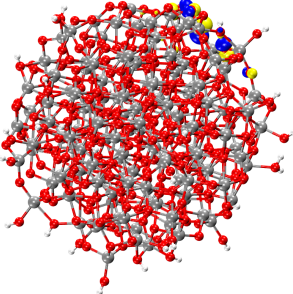
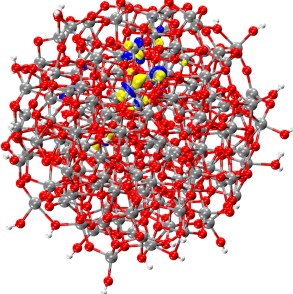
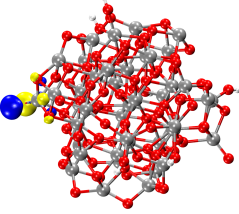
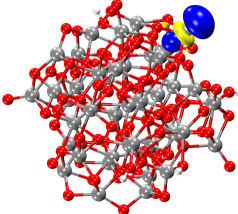
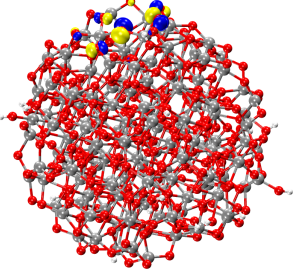
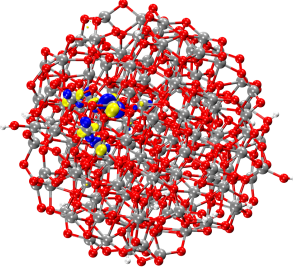
Models	HOMO	LUMO
[ZrO ₂] ₄₃ -33.33 %		
[ZrO ₂] ₁₄₁ -33.33 %		
[ZrO ₂] ₄₃ -16.66 %		
[ZrO ₂] ₁₄₁ -16.66 %		

Figure 5.13: Molecular orbitals (MOs) plot for HOMO and LUMO for [ZrO₂]₄₃ and [ZrO₂]₁₄₁ nanocluster models with 33.33 % and 16.66 % surface passivation, using PBE0 functionals. The isosurfaces are shown in yellow and blue, representing values of +0.06 and -0.06, respectively.

passivation are plotted in Figure 5.13. We observe, in the case of 33.33 % passivation rate, that the O-atoms shows p-state envelop in HOMO and Zr-atoms shows d-state envelop in LUMO. For [ZrO₂]₄₃ with 16.66 % surface passivation, defects are generated in the HOMO by surface Zr and O atoms possessing dangling bonds. Similarly, a localized defect can also be observed at Zr atoms in the LUMO state, as indicated in Table 5.13. Consequently, this effect causes the Fermi level to shift towards higher energy levels, aligning with our discussion in the PDOS section. In the case of [ZrO₂]₁₄₁ with 16.66 % passivation, slightly delocalized defects are observed in HOMO and LUMO states and cause a slight displacement of Fermi level towards higher energy levels.

In conclusion, the overall DOS profile in VBM for all nanocluster models with maximum surface passivation are similar to those observed in monoclinic phase. In particular, the DOS profile observed due to core atoms is close to the cubic phase whereas the surface atoms resemble to the monoclinic phase. However, it is observed that these effect does not change the band gap width due to core and surface atoms. Therefore, the band gap in our systems depends on the size not on the surface distortions. In addition, we find that for the models with surface passivation down to 33.3%, the band gap values closely resemble those achieved maximum surface passivation. However, a significantly smaller band gap is evident in the case of 16.7% surface passivation. This phenomenon is attributed to the existence of dangling bonds at the NP surface, which remain unpassivated when the NP surface coverage is low. Consequently, the surface atoms exhibit a lower band gap compared to the core atoms, resulting in the overall closure of the system's band gap.

5.2 Electronic properties of SnO₂ nanoparticles

5.2.1 Density of states of bulk SnO₂

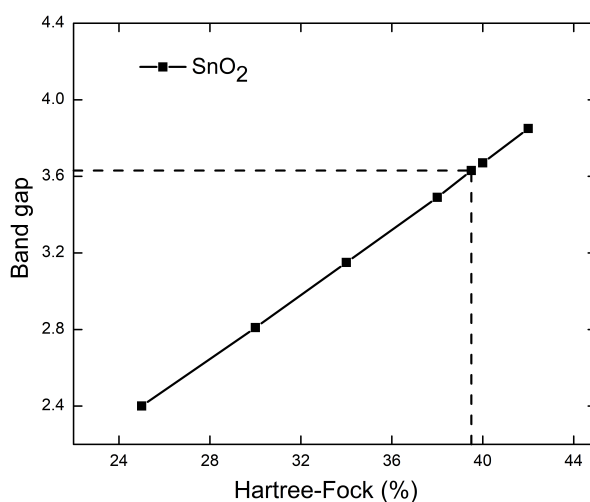


Figure 5.14: Evolution of band gap with the fraction of HF correlation.

In this section, we consider the calculated total and partial density of states for tetragonal SnO₂. The calculated band gap using PBE approximation is found to be 0.43 eV, significantly smaller than the experimentally observed band gap of 3.6 eV [60], [82], [137]. Similarly to the case of ZrO₂, we here resort to the PBE0 exchange and correlation functional and use an optimized α fraction of 39.5% as depicted in Figure 5.14, allowing to reproduce the experimental band gap of

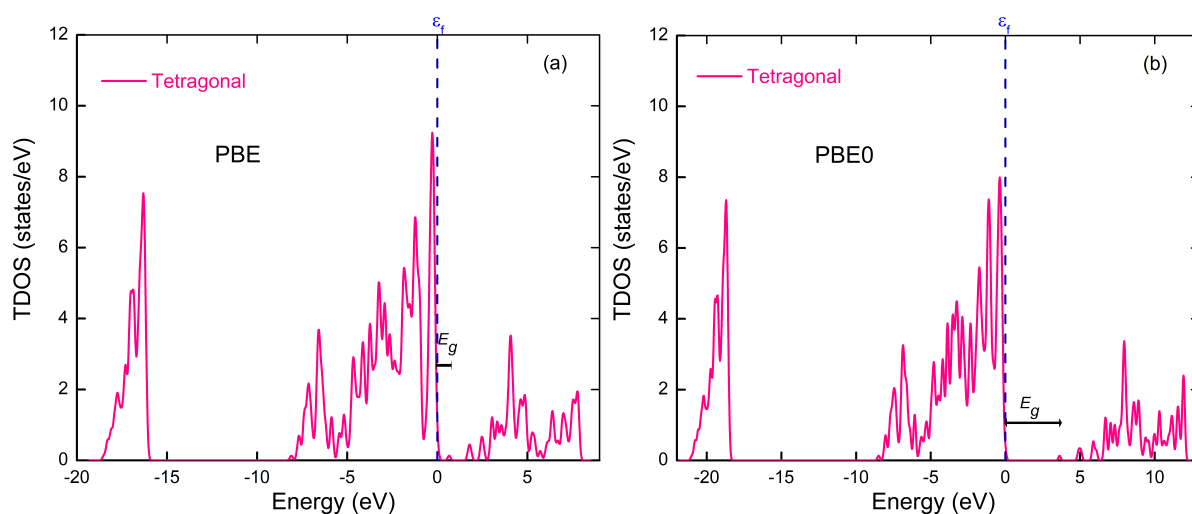


Figure 5.15: Total density of states of tetragonal phase of SnO₂ using (a) PBE and (b) PBE0 approximation.

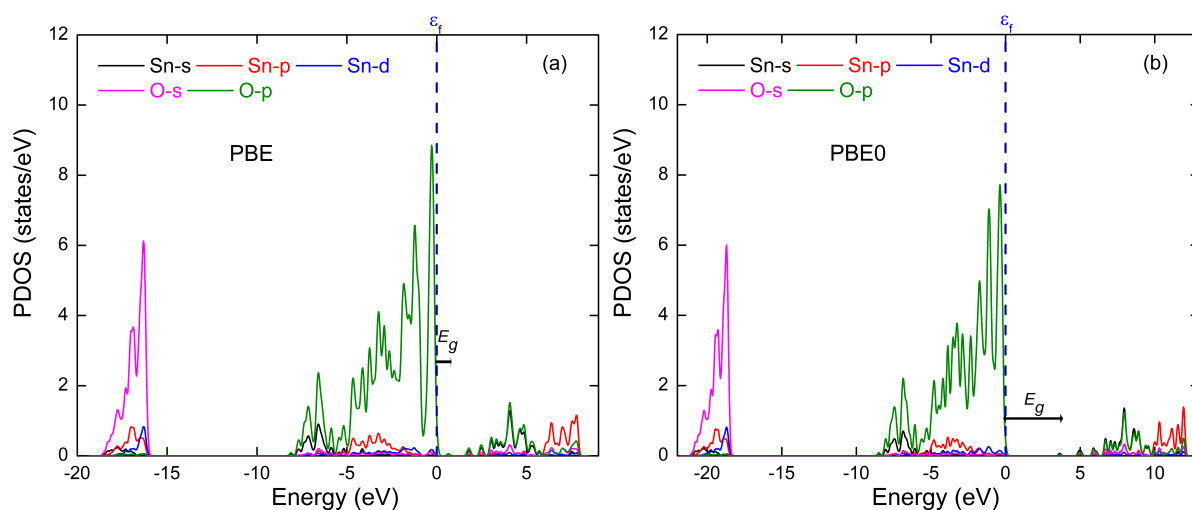


Figure 5.16: Partial density of states of tetragonal phase of SnO₂ using (a) PBE and (b) PBE0 approximation.

SnO₂ with a value of 3.63 eV.

From the Figure 5.15, we can easily note that PBE and PBE0 produce very similar DOS profiles, regardless of the energy scale. The projection of the DOS onto the orbitals of each chemical species shows that the valence band is made up of contributions from Sn s-, p- and d-orbitals and O s- and p-orbitals while mostly s-orbitals of Sn and s- and p-orbitals of O, leads to the conduction band (see Figure 5.16).

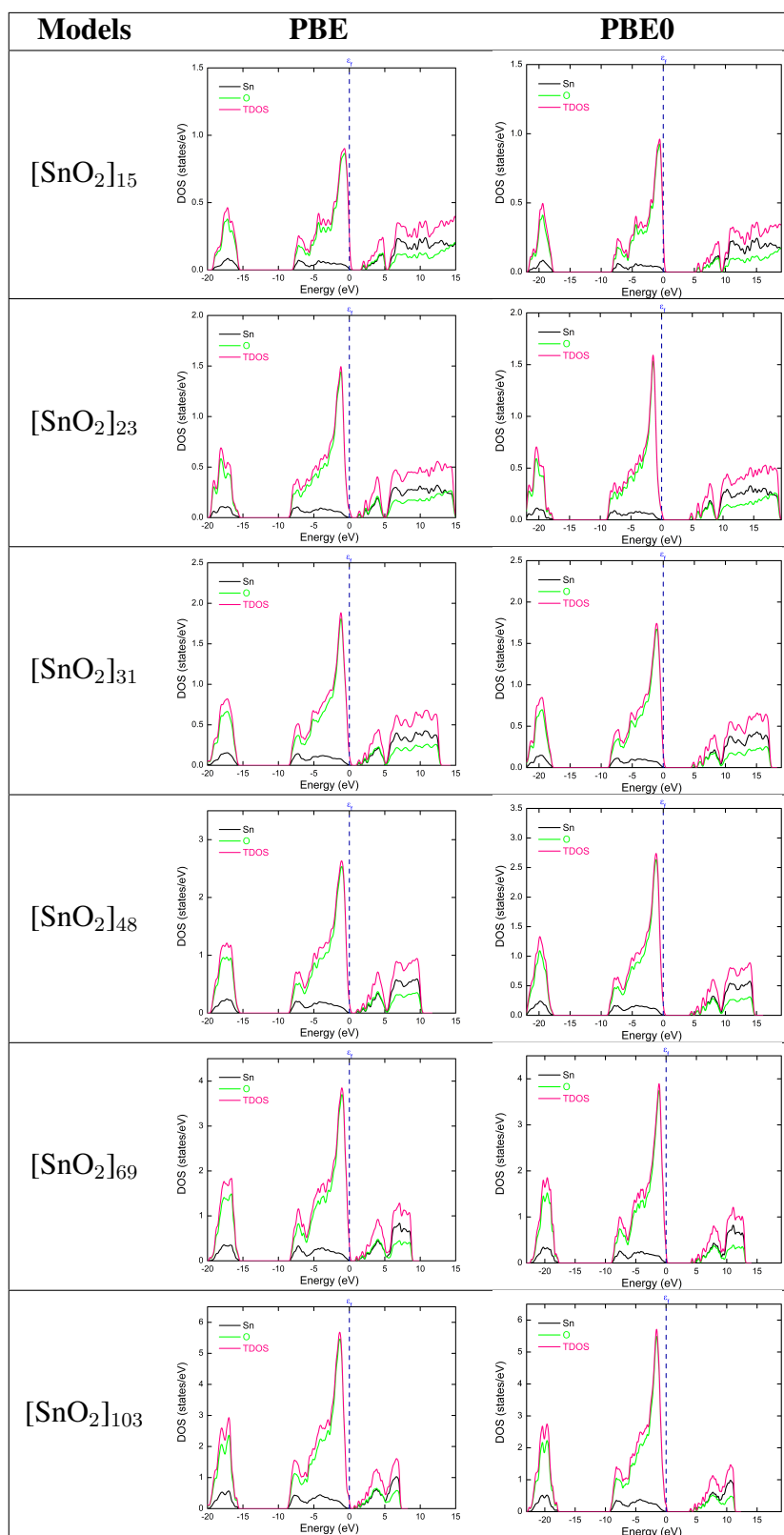


Figure 5.17: Partial and total density of states of [SnO₂] nanoclusters using (a) PBE and (b) PBE0 approximation.

5.2.2 DOS evolution as a function of size of the nanoclusters

Figure 5.17 presents the partial and total density of states for nanocluster models of [SnO₂]_n, using the PBE and PBE0 functionals. Due to their minor effect, we neglect contributions from H atoms to the DOS. The computed partial and total density of states for all studied nanoclusters with full passivation utilizing PBE (Figure 5.19a) and PBE0 (Figure 5.19b) functionals, are shown in Figure 5.19. The DOS bands of the NP show broadening compared to those of bulk SnO₂, reflecting the structural disorder within the NPs. Nevertheless, the overall intensity of relative peaks is maintained, particularly for larger NPs. Overall, the shape of the DOS of nanocluster models are very similar to the bulk system. Table 5.18 represents the band gaps and their corresponding standard deviations from mean value obtained from calculations performed on nanoclusters of different sizes.

Figure 5.18: Calculated band gap of tetragonal phase of tin (IV) oxide and their modeled nanoclusters with LDA, PBE and PBE0 functional, respectively.

Models	Band Gap (eV)		
	LDA	PBE	PBE0
SnO ₂ (bulk)	0.26	0.43	3.63
[SnO ₂] ₁₅ .9H ₂ O	1.94 ± 0.04	2.02 ± 0.04	5.66 ± 0.06
[SnO ₂] ₂₃ .15H ₂ O	1.35 ± 0.07	1.47 ± 0.02	4.91 ± 0.03
[SnO ₂] ₃₁ .17H ₂ O	1.26 ± 0.06	1.35 ± 0.06	4.84 ± 0.04
[SnO ₂] ₄₈ .22H ₂ O	1.13 ± 0.01	1.184 ± 0.013	4.55 ± 0.02
[SnO ₂] ₆₉ .27H ₂ O	0.98 ± 0.05	1.046 ± 0.05	4.30 ± 0.06
[SnO ₂] ₁₀₃ .41H ₂ O	0.68 ± 0.01	0.737 ± 0.05	4.06 ± 0.02

To facilitate comparison with literature, we calculated the band gap for our NP models using the local density approximation (LDA) . Additionally, we also provide the band gap values obtained through the utilization of PBE and PBE0 functionals for all nanocluster models. Table 5.18 presents the band gap values obtained through the utilization of LDA, PBE and PBE0 functionals for nanoclusters of various sizes. Observing the trend in the bandgap evolution of the NP, one

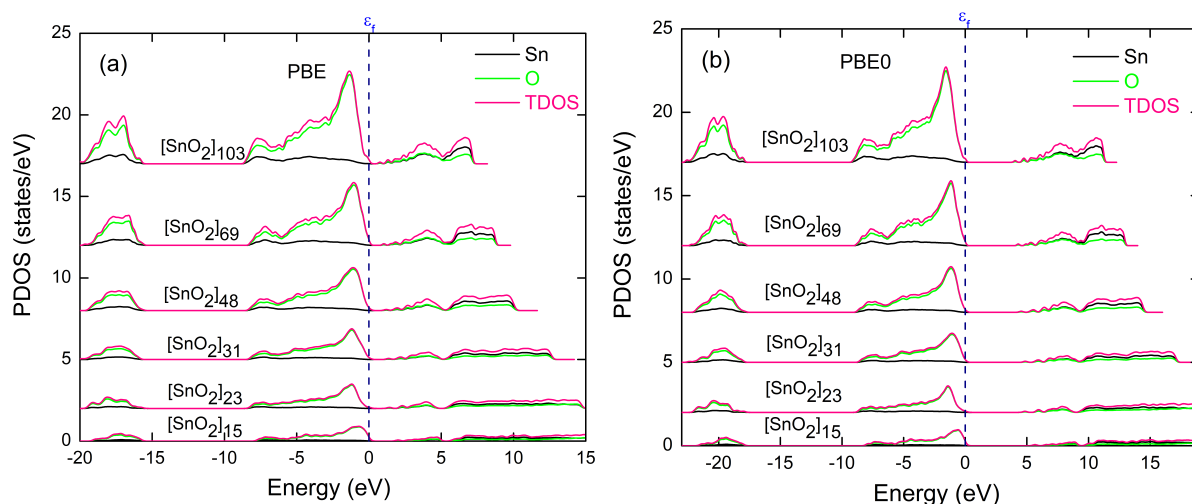


Figure 5.19: Partial and total density of states for various models [SnO₂]_n, n = 15, 23, 31, 48, 69 and 103, using (a) PBE and (b) PBE0 approximations.

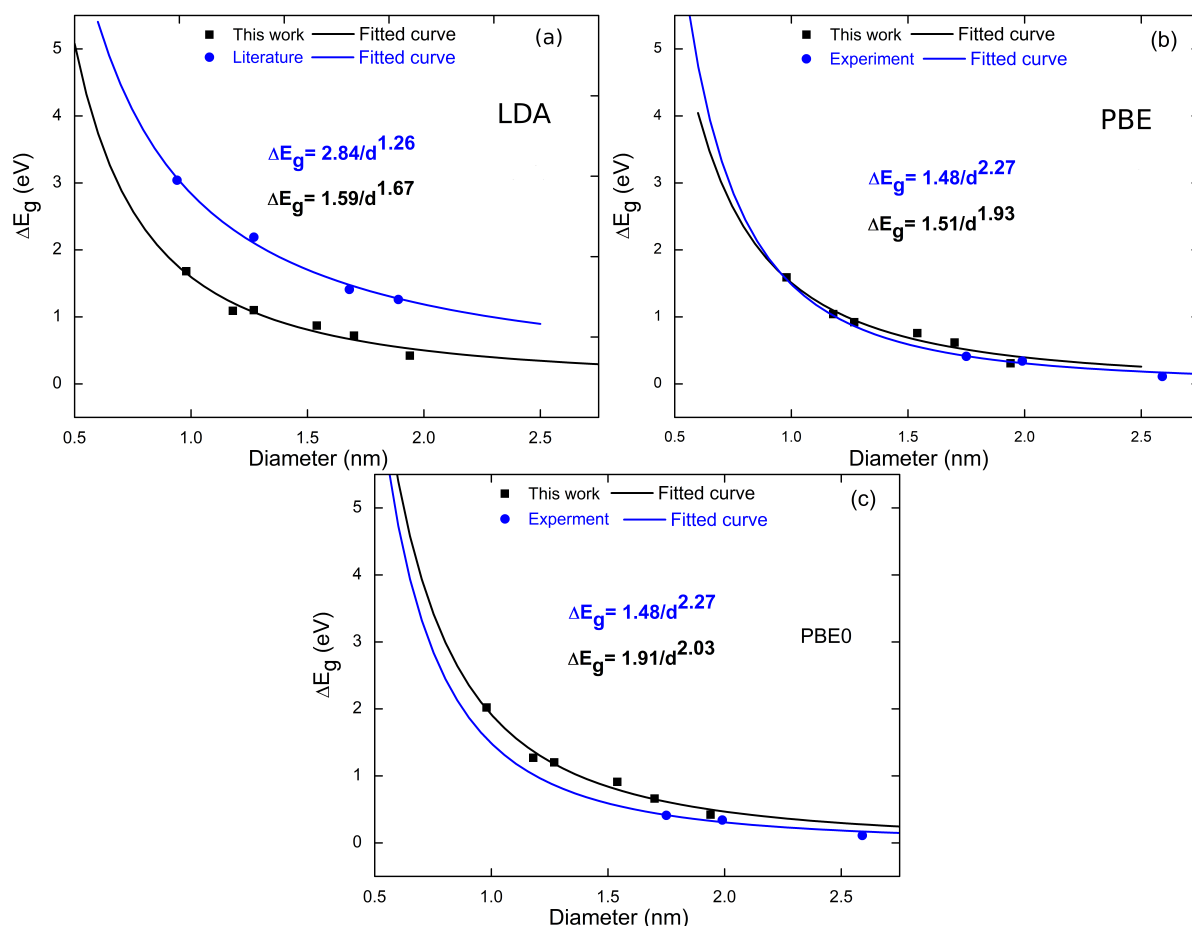


Figure 5.20: Calculated band gaps of different size of SnO₂ nanoclusters. The solid lines are the fitted curves: $\Delta E_g = 1.572/d^{1.70}$, $\Delta E_g = 1.51/d^{1.93}$ and $\Delta E_g = 1.91/d^{2.03}$ for (a) LDA compared with literature [82], (b) PBE and (c) PBE0 compared with experiment [7].

can note a decrease in the bandgap as the diameter of the nanoclusters increases, indicating the presence of quantum confinement effects in SnO₂ NPs. As discussed in the previous section for ZrO₂ systems, we employed an empirical formula to fit the curve. Similar to the ZrO₂ systems, we resort to the same formula in order to quantify the evolution of the band gap difference between SnO₂ models and bulk.

Figure 5.20 illustrates the results of the evolution of ΔE_g as a function of the NP diameter with various exchange-correlation functionals. The fitting procedure yields the following values: $\alpha = 1.70$ and $\beta = 1.57$ for LDA, $\alpha = 1.93$ and $\beta = 1.51$ for PBE, and $\alpha = 2.03$ and $\beta = 1.91$ for PBE0 approaches. Moreover, when the nanoparticle size is smaller than exciton bohr radius (a_B), it exhibits a strong confinement regime, whereas sizes larger than a_B demonstrate a weak confinement regime. The reported value of a_B is 2.7 nm in the case of SnO₂ [7]. Our nanocluster models are very small in size (less than 2 nm) and are consistent within the strong confinement regime. Consequently, our models exhibit high sensitivity to parameters such as α and β due to this strong confinement regime. Despite a shift in the curve towards lower ΔE_g for LDA, the trend of ΔE_g evolution as a function of diameter closely resembles that of the previous modeling study [82]. In this work, the overall obtained function ΔE_g is smaller than the reported function in the literature, as shown in Figure 5.20 (c). This difference is due the stabilization technique that the authors used in Ref. [82], as already discussed in Chapter 1.

For comparison with experiments, the band gap data were extracted from earlier experimental findings on SnO₂ systems in Ref. [7], revealing α and β values of 2.27 and 1.48, respectively. The trend of ΔE_g evolution as a function of diameter closely aligns with experimental observation [7] using the PBE approach, as depicted in Figure 5.20 (b). A slight deviation is observed in our models compared to experimental results using the PBE0 approach, as shown in Figure 5.20. Notably, there is a small variation in the value of β_{NP} when comparing the LDA and PBE functionals but significant change in PBE0 functional, while the value of α exhibits a significant increase with the PBE0 functional compared to LDA and PBE functionals. The value of α using LDA, PBE and PBE0 approximations are approximately consistent with expectations from the effective mass approximation (EMA) model, which predicts that the energy band gap decreasing scale is proportional to d^{-2} as the effective diameter increases [8].

5.2.3 Core and surface atoms contribution to the total DOS

By leveraging the analysis of core-surface atoms, we project the DOS onto atoms within the core and surface regions of [SnO₂]₃₁, [SnO₂]₄₈, [SnO₂]₆₉ and [SnO₂]₁₀₃ nanoclusters, as depicted in Figures 5.21. Overall, our observations indicate that surface atoms exhibit higher intensity peaks across all PDOS bands compared to core atoms. This trend is particularly evident near the Fermi level, where the contribution of O-p orbitals in surface atoms is notably higher compared to core

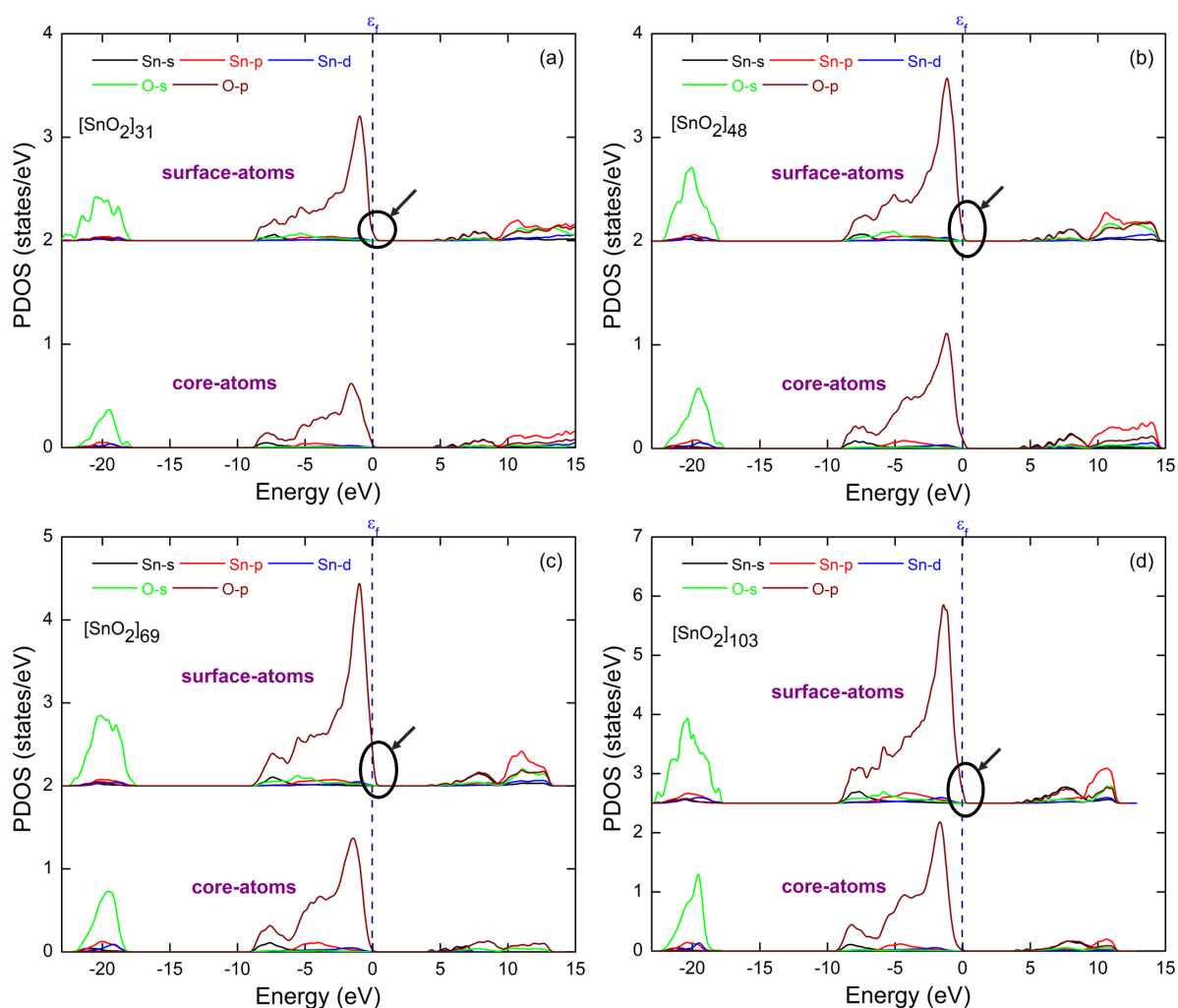


Figure 5.21: Partial density of states for the atoms in core and surface of (a) [SnO₂]₃₁, (b) [SnO₂]₄₈, (c) [SnO₂]₆₉ and (d) [SnO₂]₁₀₃ nanoclusters. PDOS of surface atoms are shifted vertically for clarity.

atoms, a phenomenon likely attributed to the greater number of surface atoms. Notably, a very small defects in the valence band due to surface atoms can be observed near to the fermi level and that slightly reduce the band gap width. Interestingly, it is observed that the DOS profile due to the core and the surface atoms show very similar features, despite of the intensity.

Figure 5.2 illustrate the HOMO and LUMO orbitals for [SnO₂]₃₁, [SnO₂]₄₈, [SnO₂]₆₉ and [SnO₂]₁₀₃ nanoclusters. It is observed that the HOMO is predominantly localized on the oxygen sites, with a minor contribution from the Sn sites, exhibiting p-state characteristics. Conversely, the LUMO is primarily localized on both Sn sites, demonstrating s-state characteristics, while a minor portion of the O sites exhibit p-state characteristics.

In conclusions, we have effectively fit the evolution of band gaps as a function of nanocluster

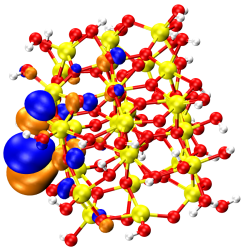
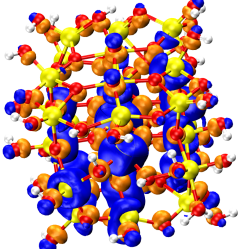
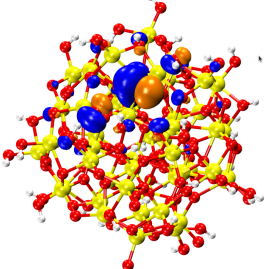
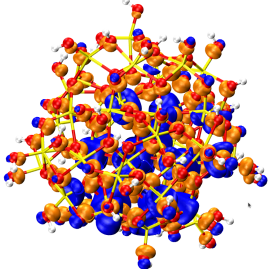
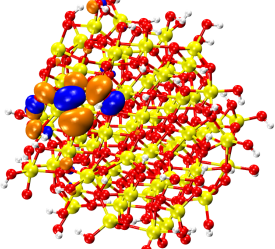
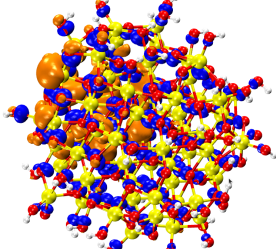
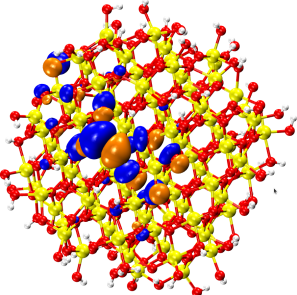
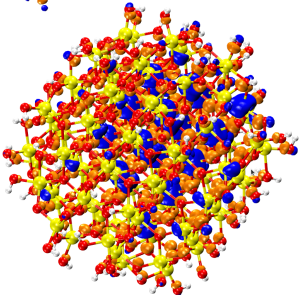
Models	HOMO	LUMO
[SnO ₂] ₃₁		
[SnO ₂] ₄₈		
[SnO ₂] ₆₉		
[SnO ₂] ₁₀₃		

Table 5.2: Molecular orbitals plot for HOMO and LUMO of the [SnO₂]_n nanocluster models using PBE0 functionals. The isosurfaces are shown in orange and blue, representing values of +0.02 and -0.02, respectively.

size and determined the quantum confinement parameters. The observed trend of quantum confinement effects in our models closely aligns with experimental finding. Analysis of the PDOS profiles for atoms within the core and surface reveals similar features, albeit with varying intensities. Overall, the distortions at the nanocluster surface does not affect in the DOS profile.

5.3 Comparison of electronic properties between ZrO₂ and SnO₂ NPs

Figure 5.22 presents a comparison of the quantum confinement effects in ZrO₂ and SnO₂ systems using PBE and PBE0 functionals in panels (a) and (b). When employing the PBE functional, we determined the values of α_{NP} as 1.738 and β_{NP} as 0.917 for ZrO₂ systems, while for SnO₂ systems, the values were $\alpha_{NP} = 1.93$ and $\beta_{NP} = 1.51$. Similarly, using the PBE0 functional, we found $\alpha_{NP} = 2.782$ and $\beta_{NP} = 0.86$ for ZrO₂ systems and $\alpha_{NP} = 2.03$ and $\beta_{NP} = 1.91$ for SnO₂ systems. Because of the higher value of β in SnO₂ systems, ΔE_g curve is shifted towards higher energy values compared to the ZrO₂ systems, as shown in Figure 5.22. Similarly, the value of α in SnO₂ systems is higher than ZrO₂ systems, led to the sharpens of ΔE_g curve. Therefore, these values confirm that the SnO₂ systems shows higher strength in QC as compared with the ZrO₂ systems.

Notably, the energy scale obtained in this study varies with $d^{-1.738}$ for ZrO₂ systems and $d^{-1.93}$ for SnO₂ systems using the PBE functional, which is remarkably close to the d^{-2} of the EMA model. Similarly, the energy scale in the PBE0 functional for ZrO₂ and SnO₂ systems varies with $d^{-2.782}$ and $d^{-2.03}$, respectively, indicating a significant deviation from the d^{-2} of the EMA model.

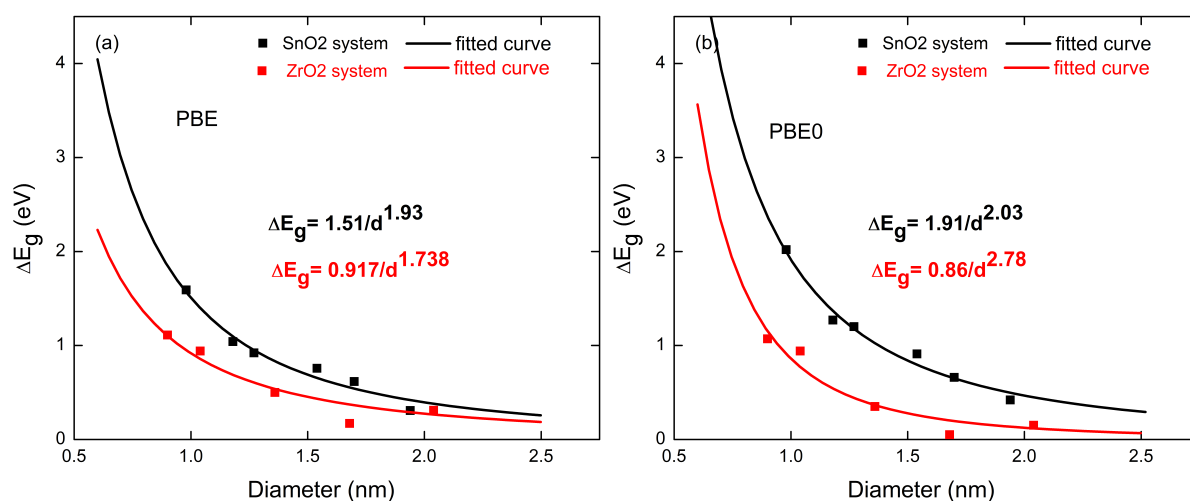


Figure 5.22: Comparison of computed energy band gap difference of ZrO₂ and SnO₂ NPs relative to that of the bulk material $\Delta E_g = E_g^{NP} - E_g^{bulk} = \beta_{NP}/d^{\alpha_{NP}}$ as a function of the NP size using (a) PBE and (b) PBE0 functional.

5.4 Conclusions

In summary, we first showed the electronic properties of bulk ZrO₂ and its nanoclusters, using PBE and PBE0 functional. Notably, incorporating 28% HF of PBE exchange yielded a band gap closely aligning with experimental values. The comparison between PBE and PBE0 demonstrated similar DOS profiles, irrespective of deep energy states. We proceeded to calculate the band gap and visualize both PDOS and TDOS as functions of nanocluster size. The observed trend revealed an increase in the band gap as the nanocluster size decreased, a phenomenon identified as the quantum confinement effect. Quantum confinement parameters, denoted as α and β , were also determined using PBE and PBE0 functional, respectively. Subsequently, we have calculated the band gap for the partially passivated nanoclusters, revealing that at least 33.3% surface passivation is required in order to ensure good electronic properties in the case of (ZrO₂) NPs. Below 33.3% surface passivation showed defects near to the Fermi level and mid-gap states, leading to the closure of band gap. Later, we computed the PDOS for core and surface atoms in [ZrO₂]₄₃, [ZrO₂]₈₀, and [ZrO₂]₁₄₁ nanoclusters with full passivation, offering a detailed insight into the distribution of electronic states within these structures. The band gap remains consistent between core and surface atoms, indicating that structural distortions do not significantly influence it. However, an analysis of the PDOS reveals distinct characteristics: the PDOS profile for core atoms resembles the cubic phase, whereas that for surface atoms reflects features of the monoclinic phase. Furthermore, we also presented the DOS for the atoms in the core and surface with 33.3% and 16.7% surface passivation, respectively, revealing that the DOS profile for the core closely resembles that of the bulk, while surface atoms exhibit defects. Furthermore, we showed the wave function characteristics of HOMO and LUMO, highlighting that the HOMO is mostly localized on the O sites, displayed p-state character whereas the LUMO are mostly localized on Zr sites, displaying d-state character.

Similarly, our exploration extended to the electronic properties of bulk SnO₂ and the corresponding nanoclusters, employing the PBE and PBE0 functional methods. To align the calculated band gap with experimental values, we incorporated 39.5% of HF of PBE exchange for both bulk and nanoclusters. The DOS and TDOS profiles were plotted for each nanocluster size, revealing remarkably similar patterns between PBE and PBE0 regardless of deep energy states. The calculated band gap was then plotted as a function of nanocluster sizes, demonstrating a consistent trend of increasing electronic band gap with decreasing the nanocluster size. Quantum confinement parameters, α and β , were computed for SnO₂ systems, using a similar approach adopted for ZrO₂. Similarly, we plotted the core atoms and surface atoms contribution to the DOS profile. Interestingly, it is found that the DOS profile due to core and surface exhibit identical features. However, in the case of ZrO₂ systems, it is different. Furthermore, we showed the wave function characteristics of HOMO and LUMO for the nanocluster sizes in the SnO₂ systems.

Furthermore, we conducted a comparative analysis of the electronic properties of ZrO_2 and SnO_2 nanoclusters with similar sizes. In particular, we compared the band gap evolution as a function of size of these nanocluster models. Notably, the band gap of ZrO_2 nanoclusters was found to be greater compared to that of SnO_2 nanoclusters. This observation underscores a significant distinction in the electronic properties between these two system nanocluster models.



6

General conclusions

The growing interest in nanocrystalline materials, driven by their diverse technical applications in various fields, has led to increased attention from the scientific community and researchers. Specifically, nanoparticles NPs exhibit a distinctive form of structural disorder, resulting from their small in size and inherent characteristics that can substantially modify their properties. In order to comprehend the structure-properties relationship, we conducted a study where we simulated ZrO_2 and SnO_2 nanoclusters with different sizes, while ensuring that the stoichiometry was maintained. A modeling protocol is developed in order to replicate the experimentally obtained PDFs and distinguish between the structural characteristics of the core and surface. Furthermore, we investigate the impact of the structural and electronic characteristics in relation to the size of the nanoparticles.

Structure of ZrO_2 nanoparticles

To scrutinize the relationship between structural features and properties, first-principle molecular dynamics and density functional theory calculations were conducted using CP2K software. The investigation into the size-dependent properties of zirconia nanoparticles involved constructing five nanocluster models with varying sizes ($[\text{ZrO}_2]_n$, $n=14, 16, 43, 80, \text{ and } 141$) corresponding to sizes of 0.9 nm, 1.04 nm, 1.32 nm, 1.78 nm, and 2.04 nm, respectively. All models exhibit Zr and O dangling bonds on the nanocluster surface, resulting in under-coordinated atoms at the surface. Water molecules were positioned at a distance of 2.2 Å from the Zr atoms on the surface, intending to passivate both Zr and O dangling bonds following spontaneous water splitting at the surface. Quantum MD simulations at various temperatures were conducted to facilitate water splitting and induce structural relaxation on the surface, aiming to produce stable configurations. Subsequently, we computed PDFs following thermal treatment schemes labeled as TT1, TT2, and TT3. The computed PDFs were then compared with experimental PDFs to validate our nanocluster models. The analysis revealed that the nanocluster $[\text{ZrO}_2]_{43}$ exhibited excellent agreement with experimental PDF Exp1 at short-range distances (less than 6 Å), while $[\text{ZrO}_2]_{141}$ demonstrated strong agreement at larger-range distances (greater than 6 Å) with maximum surface passivation (84%). Furthermore, $[\text{ZrO}_2]_{43}$, with 33.33% surface passivation (4 H_2O) achieved through a thermal treatment (TT3), exhibited good agreement with experimental PDFs

Exp2.

Finally, we focus to separate the atoms within the core and those at the surface of nanoclusters in order to examine the structural distinction. Specifically, we focus on to calculate the average Zr-O bond length inside a 3 Å wide shell, extending from center to the surface of NP. The average distances of Zr-O for $[\text{ZrO}_2]_{43}$, $[\text{ZrO}_2]_{80}$ and $[\text{ZrO}_2]_{141}$ nanoclusters maintain a constant value within a specific range of distances from the center. We can infer from the obtained results that the structure of the atoms in the nanocluster core and on the surface exhibits differently. Our findings indicate that the average Zr-O distances remain constant up to a certain range of r , after which they begin to decrease as the surface of the nanocluster is approached. This allows us to establish a boundary between atoms within the core and those on the relaxed surface of the nanoclusters. Additionally, we generated histograms for the atoms within the core and those on the surface, comparing them with the partial PDF of cubic and monoclinic phases of zirconia. It is observed that the core of the nanocluster closely resembles the cubic phase, while the surface exhibits characteristics resembling the monoclinic phase. Following the investigation of the environment surrounding Zr-atoms within the core and on the surface of nanoclusters, it is evident that the core predominantly exhibits a high fraction of 7-fold geometry. Conversely, the surface predominantly displays 5 and 6-fold geometry.

Structure of SnO_2 nanoparticles

In this study, we begin by constructing multiple models of nanoclusters consisting of $[\text{SnO}_2]_n$, where, $n = 15, 23, 31, 48, 69,$ and 103 . The objective is to examine how the properties of the system are influenced by the size of the clusters. In order to mitigate the presence of dangling bonds at the surface, water molecules have been positioned atop the surface Sn-atoms of nanoclusters. This study involved conducting Quantum MD simulations at various temperatures to stabilize the structural and calculate the electronic properties of simulated SnO_2 nanoparticles. Notably, it was observed that the structure exhibited the formation of dimers and trimers at the surface. We presented the partial PDFs relative to the size of the nanoparticles. Importantly, minor peaks were detected at a distance of 1.4 Å, providing evidence supporting the presence of dimers and trimers on the surface of the nanoparticles.

To avoid the formation of these structures, we select those oxygen that cause such formation than we passivated those O-atoms by positioning H-atoms, and same number of OH placed at the surface of Sn-atoms. These procedured lead to the full surface passivation. Additionally, we conducted quantum MD simulations on the modeled nanoclusters at various temperatures

in order to achieve optimal structure. Furthermore, we computed PDFs based on neutron total scattering, considering the last 5 ps of equilibrated trajectories following thermal treatments TT3. Subsequently, we compared these PDFs with the corresponding experimental PDFs. It is observed that the initial peak in the calculated PDF of all size nanoclusters closely resembles the experimental PDF, despite of the intensity. Specifically, the calculated PDF for the large system $[\text{SnO}_2]_{103}$ closely resembles the experimental PDF. The majority of peaks are reproduced, although there are minor deviations in peak positions. The agreement between the calculated and experimental PDFs are notably pronounced within a range of 8.0 \AA , underscoring a robust correspondence in this region. In addition, it is evident that the calculated PDF peaks exhibit a displacement towards larger distance values, accompanied by a decrease in peak intensities across the nanoclusters. Ultimately, the partial PDFs were computed for each size of the simulated nanoclusters. These PDFs were then compared to the PDFs of the corresponding bulk materials. The examination of the Sn-O, O-O, and Sn-Sn PDFs reveals that the $[\text{SnO}_2]_{103}$ nanocluster exhibits a structural arrangement that closely resembles the bulk SnO_2 material in terms of short and medium range distances, particularly those distances that are smaller than 10 \AA . Additionally, we calculated the Sn-O bond length by considering shell of width 3 \AA as a function of distance (r) from the central atom to differentiate between the core and surface of the nanoclusters. Our results indicate that the Sn-O bond length of core atoms fluctuate little bit up to a certain distance, then sharply decreases towards the surface of the nanoclusters. Subsequently, utilizing the boundary condition, histograms for Sn-O, O-O, and Sn-Sn distances were calculated for core and surface atoms. Specifically, the Sn-Sn histograms illustrate the occurrence of both double and single bridges connecting Sn atoms. The reduced intensity of the peak associated with double bridges is attributed to their lesser prevalence compared to single bridges. Notably, examination of the smallest nanoparticles unveils a reversal in the ratio of double to single bridges, with nanoparticles exhibiting a higher proportion of double bridges. Moreover, the double bridges demonstrate increased elongation in comparison to those present in the bulk structure. With this analysis, our observations suggest that core atoms closely resemble bulk SnO_2 , while surface atoms exhibit a distinct structure compared to the bulk material. Finally, we determined the fraction of coordination numbers of Sn-atoms within the core and on the surface of nanoclusters. It appears that there is a high fraction of coordination number exhibited by Sn-atoms in the core, which is 6, resembling that of the bulk, whereas the surface displays a lower coordination number.

Electronic properties of ZrO_2 and SnO_2 nanoparticles

In summary, the electronic properties of bulk ZrO_2 and its nanoclusters were initially demon-

strated through using of PBE and PBE0 functional methods. It was determined that employing 28 % of HF in the PBE exchange method resulted in a band gap that closely approximated the experimental band gap. Furthermore, it is worth mentioning that both PBE and PBE0 exhibit remarkably similar density of states profiles, irrespective of the presence of deep energy states. Nevertheless, we have conducted calculations to determine the band gap and have subsequently generated plots illustrating the density of states and total density of states in relation to the nanocluster size. It has been observed that the reduction in band gap, known as the quantum confinement effect, occurs as the size of the nanocluster increases. Furthermore, we have computed the quantum confinement parameters α and β utilizing the PBE and PBE0 functionals, respectively. Subsequently, the band gap of the partially passivated nanoclusters was computed, revealing that a minimum of 33.33 % surface passivation is necessary to guarantee favorable electronic properties in the context of (ZrO₂) nanoparticles. Finally, we have calculated and showed the PDOS for the atoms in the core and the surface of the [ZrO₂]₄₃, [ZrO₂]₈₀ and [ZrO₂]₁₄₁, nanoclusters, with various surface passivation rate. It is observed that the band gap for core and surface atoms are the same. However, the DOS profile for the atoms in the core shows similar features with the cubic phase whereas the surface atoms shows monoclinic features. In addition, up to 33.3 % surface passivation, no defects have been observed in the valence and conduction bands. However, with a 16.7 % surface passivation, defects near the Fermi level and mid-gap state were observed due to surface atoms carrying dangling bonds. Nonetheless, the core remains consistent regardless of the passivation rate. Additionally, we have demonstrated the distinctive properties of the HOMO and the LUMO. Our findings indicate that the HOMO is primarily located on the oxygen sites, exhibiting characteristics of the p-state. Conversely, the LUMO is predominantly localized on the Zr sites, displaying characteristics of the d-state. By examining the HOMO and LUMO for 16.66 % surface passivation, we can clearly observe the localized defect at the surface, correlating with the defects observed in the PDOS.

In a similar vein, we have demonstrated the electronic properties of bulk SnO₂ and its associated nanoclusters through using both of the PBE and PBE0 functional methods. To achieve a more accurate estimation of the band gap, we employed a 39.5 % proportion of HF of PBE exchange in our calculations for both bulk and nanocluster systems. Furthermore, we have generated plots depicting the DOS and TDOS for various nanocluster sizes. Additionally, we have graphed the computed band gap as a function of nanocluster sizes, and it has been observed that the electronic band gap decreases with an increase in the size of the nanoclusters. Similar to ZrO₂ systems, we have also computed the quantum confinement parameters α and β for SnO₂ systems. However, we found that the quantum confinement parameters are larger in SnO₂ systems in comparison with the ZrO₂ systems. In addition, we calculated the PDOS for the atoms within

the core and for the surface and it is notable that the DOS profile for both core and the surface atoms exhibits similar features. However, in the case of ZrO_2 systems, the features is different foe core and surface atoms. Finally, we demonstrated the wave function properties of the HOMO and the LUMO for nanoclusters of varying sizes.

Final remarks

Understanding the overall structure of ultrasmall nanoparticles is challenging due to their complex structural organization and high surface disorder. However, by dissecting the core and surface of nanoparticles and studying them separately, we gain insight into their structure. We observe that the atoms within the core tend to exhibit a more crystalline structure, especially in larger nanoparticles, whereas the surface undergoes structural modifications. Specifically, in the case of ZrO_2 , the core of the nanoparticle exhibits a structure resembling bulk cubic, while the surface adopts a bulk monoclinic-like structure. Similarly, in the case of SnO_2 , the core remains crystalline and displays a bulk tetragonal phase, whereas the surface exhibits structural disorder resembling an amorphous-like structure. Moreover, our investigation uncovers that achieving favorable electronic properties requires passivating the nanocluster surface up to a certain minimum proportion. Below this threshold, defects may arise from surface atoms carrying dangling bonds, consequently narrowing the overall electronic band gap.

Perspectives

- Employ the DFT MD trajectories obtained as a training database to create machine learning potentials capable of simulating systems comprising a hundred thousand atoms.
- Use the final MD trajectory files and calculate several properties like photoluminescence, catalytic properties, adsorption, etc.



7

Bibliography

Summary

References	140
List of Works	150

References

- [1] S. Sarkar, E. Guibal, F. Quignard, and A. SenGupta, “Polymer-supported metals and metal oxide nanoparticles: synthesis, characterization, and applications,” *Journal of Nanoparticle Research*, vol. 14, no. 2, pp. 1–24, 2012.
- [2] A. B. Sengul and E. Asmatulu, “Toxicity of metal and metal oxide nanoparticles: a review,” *Environmental Chemistry Letters*, vol. 18, no. 5, pp. 1659–1683, 2020.
- [3] M. S. Chavali and M. P. Nikolova, “Metal oxide nanoparticles and their applications in nanotechnology,” *SN applied sciences*, vol. 1, no. 6, pp. 1–30, 2019.
- [4] A. Rastogi, M. Zivcak, O. Sytar, *et al.*, “Impact of metal and metal oxide nanoparticles on plant: a critical review,” *Frontiers in chemistry*, vol. 5, p. 78, 2017.
- [5] B. Gilbert, F. Huang, H. Zhang, G. A. Waychunas, and J. F. Banfield, “Nanoparticles: strained and stiff,” *Science*, vol. 305, no. 5684, pp. 651–654, 2004.
- [6] H. Dosch, “Some general aspects of confinement in nanomaterials,” *Applied Surface Science*, vol. 182, no. 3-4, pp. 192–195, 2001.
- [7] E. J. Lee, C. Ribeiro, T. Giraldi, E. Longo, E. Leite, and J. A. Varela, “Photoluminescence in quantum-confined ZnO nanocrystals: evidence of free exciton decay,” *Applied Physics Letters*, vol. 84, no. 10, pp. 1745–1747, 2004.
- [8] A. Onyia, H. Ikeri, and A. Nwobodo, “Theoretical study of the quantum confinement effects on quantum dots using particle in a box model,” *Journal of Ovonic Research*, vol. 14, no. 1, pp. 49–54, 2018.
- [9] S. J. Billinge and I. Levin, “The problem with determining atomic structure at the nanoscale,” *science*, vol. 316, no. 5824, pp. 561–565, 2007.
- [10] H. Zhang, B. Gilbert, F. Huang, and J. F. Banfield, “Water-driven structure transformation in nanoparticles at room temperature,” *Nature*, vol. 424, no. 6952, pp. 1025–1029, 2003.
- [11] A. Henglein, “Small-particle research: physicochemical properties of extremely small colloidal metal and semiconductor particles,” *Chemical reviews*, vol. 89, no. 8, pp. 1861–1873, 1989.

- [12] H. Weller, "Colloidal semiconductor q-particles: chemistry in the transition region between solid state and molecules," *Angewandte Chemie International Edition in English*, vol. 32, no. 1, pp. 41–53, 1993.
- [13] A. Hagfeldt and M. Graetzel, "Light-induced redox reactions in nanocrystalline systems," *Chemical reviews*, vol. 95, no. 1, pp. 49–68, 1995.
- [14] P. V. N. Santos, M. M. Ferrer, R. S. Nunes, E. Longo, Y. V. Santana, and J. A. Varela, "Cadmium sulfide nanoparticles obtained by a new liquid-liquid route,"
- [15] *History blog*, August 28, 2013. [Online]. Available: <http://www.thehistoryblog.com/archives/26724>.
- [16] U. Leonhardt, "Invisibility cup," *Nature photonics*, vol. 1, no. 4, pp. 207–208, 2007.
- [17] C. Toumey, "Plenty of room, plenty of history," *Nature nanotechnology*, vol. 4, no. 12, pp. 783–784, 2009.
- [18] N. Taniguchi, "On the basic concept of nanotechnology," *Proceeding of the ICPE*, 1974.
- [19] G. Binnig and H. Rohrer, "Scanning tunneling microscopy," *Surface science*, vol. 126, no. 1-3, pp. 236–244, 1983.
- [20] NBIC+, *Statnano*, April 12, 2023. [Online]. Available: <https://statnano.com/news/68317/Nanotechnology-Publications-Number-and-Annual-Growth-Rate-of-Nano-articles-in-the-Past-20-Years>.
- [21] *Nanoparticles*, April 12, 2023. [Online]. Available: <https://prochimia.com/nanoparticles>.
- [22] K. P. Steckiewicz and I. Inkielewicz-Stepniak, "Modified nanoparticles as potential agents in bone diseases: cancer and implant-related complications," *Nanomaterials*, vol. 10, no. 4, p. 658, 2020.
- [23] J. Gambe, "Non-hydrolytic synthesis and structure of zro2 nanoparticles," Ph.D. dissertation, Université de Limoges, 2017.
- [24] L. Bányai and S. W. Koch, *Semiconductor quantum dots*. World Scientific, 1993.
- [25] C. Murray, D. J. Norris, and M. G. Bawendi, "Synthesis and characterization of nearly monodisperse cde (e= sulfur, selenium, tellurium) semiconductor nanocrystallites," *Journal of the American Chemical Society*, vol. 115, no. 19, pp. 8706–8715, 1993.
- [26] L. E. Brus, "Electron–electron and electron-hole interactions in small semiconductor crystallites: the size dependence of the lowest excited electronic state," *The Journal of chemical physics*, vol. 80, no. 9, pp. 4403–4409, 1984.
- [27] M. Kapilashrami, Y. Zhang, Y.-S. Liu, A. Hagfeldt, and J. Guo, "Probing the optical property and electronic structure of tio2 nanomaterials for renewable energy applications," *Chemical reviews*, vol. 114, no. 19, pp. 9662–9707, 2014.

- [28] A. M. Smith, A. M. Mohs, and S. Nie, "Tuning the optical and electronic properties of colloidal nanocrystals by lattice strain," *Nature nanotechnology*, vol. 4, no. 1, pp. 56–63, 2009.
- [29] D. P. Pham, D. Oh, V.-A. Dao, Y. Kim, and J. Yi, "Enhanced energy conversion performance of silicon solar cells by quantum-confinement effect of polysilicon oxide," *Applied Materials Today*, vol. 29, p. 101 604, 2022.
- [30] P. Gupta and M. Ramrakhiani, "Influence of the particle size on the optical properties of cdse nanoparticles," *The Open Nanoscience Journal*, vol. 3, no. 1, 2009.
- [31] A. K. Tripathi, M. K. Singh, M. C. Mathpal, S. K. Mishra, and A. Agarwal, "Study of structural transformation in tio2 nanoparticles and its optical properties," *Journal of Alloys and Compounds*, vol. 549, pp. 114–120, 2013.
- [32] M. K. Choi, J. Yang, T. Hyeon, and D.-H. Kim, "Flexible quantum dot light-emitting diodes for next-generation displays," *npj Flexible Electronics*, vol. 2, no. 1, p. 10, 2018.
- [33] R. C. Castro, D. S. Ribeiro, and J. L. Santos, "Visual detection using quantum dots sensing platforms," *Coordination Chemistry Reviews*, vol. 429, p. 213 637, 2021.
- [34] P. D. H. Weller, *Physical chemistry: universität hamburg*, April 12, 2023. [Online]. Available: <http://www.nanodeck.de/english/nano2.html>.
- [35] M. Hampden-Smith, T. Kodas, and A. Ludviksson, "Chemical vapor deposition, chemistry of advanced materials. an overview, interrante, lv; hampden-smith, mj ed," *Wiley-VCH: New York, capitol*, vol. 5, pp. 143–206, 1998.
- [36] A. P. Alivisatos, "Perspectives on the physical chemistry of semiconductor nanocrystals," *The Journal of Physical Chemistry*, vol. 100, no. 31, pp. 13 226–13 239, 1996.
- [37] S. Mørup, "Studies of superparamagnetism in samples of ultrafine particles," *Nanomagnetism*, pp. 93–99, 1993.
- [38] J. Dormann and D. Fiorani, *Magnetic properties of fine particles*. Elsevier, 2012.
- [39] H. Gleiter, "Nanostructured materials: basic concepts and microstructure," *Acta materialia*, vol. 48, no. 1, pp. 1–29, 2000.
- [40] M. Grätzel, "Photoelectrochemical cells," *nature*, vol. 414, no. 6861, pp. 338–344, 2001.
- [41] M. Fernandez-Garcia, A. Martinez-Arias, J. Hanson, and J. Rodriguez, "Nanostructured oxides in chemistry: characterization and properties," *Chemical reviews*, vol. 104, no. 9, pp. 4063–4104, 2004.
- [42] S. J. Billinge, "Nanoscale structural order from the atomic pair distribution function (pdf): there's plenty of room in the middle," *Journal of Solid State Chemistry*, vol. 181, no. 7, pp. 1695–1700, 2008.
- [43] H. Zheng *et al.*, "Observation of single colloidal platinum nanocrystal growth trajectories," *Science*, vol. 324, no. 5930, pp. 1309–1312, 2009.

- [44] T. Egami and S. J. Billinge, *Underneath the Bragg peaks: structural analysis of complex materials*. Elsevier, 2003.
- [45] M. Gateshki, V. Petkov, G. Williams, S. Pradhan, and Y. Ren, “Atomic-scale structure of nanocrystalline zro 2 prepared by high-energy ball milling,” *Physical Review B*, vol. 71, no. 22, p. 224 107, 2005.
- [46] M. Gateshki, V. Petkov, T. Hyeon, J. Joo, M. Niederberger, and Y. Ren, “Interplay between the local structural disorder and the length of structural coherence in stabilizing the cubic phase in nanocrystalline zro2,” *Solid state communications*, vol. 138, no. 6, pp. 279–284, 2006.
- [47] C. Tyrsted, N. Lock, K. Jensen, *et al.*, “Evolution of atomic structure during nanoparticle formation,” *IUCrJ*, vol. 1, no. 3, pp. 165–171, 2014.
- [48] G. D. Wilk, R. M. Wallace, and J. Anthony, “High-k gate dielectrics: current status and materials properties considerations,” *Journal of applied physics*, vol. 89, no. 10, pp. 5243–5275, 2001.
- [49] S. Sayan, M. Croft, N. Nguyen, *et al.*, “The relation between crystalline phase, electronic structure, and dielectric properties in high-k gate stacks,” in *AIP Conference Proceedings*, American Institute of Physics, vol. 788, 2005, pp. 92–101.
- [50] M. Bocanegra-Bernal and S. D. De La Torre, “Phase transitions in zirconium dioxide and related materials for high performance engineering ceramics,” *Journal of materials science*, vol. 37, pp. 4947–4971, 2002.
- [51] Y. Tian, C. Chen, D. Wang, and Q. Ji, “Recent developments in zirconia thermal barrier coatings,” *Surface Review and Letters*, vol. 12, no. 03, pp. 369–378, 2005.
- [52] S. J. Skinner and J. A. Kilner, “Oxygen ion conductors,” *Materials Today*, vol. 6, no. 3, pp. 30–37, 2003.
- [53] S. Das, C.-Y. Yang, and C.-H. Lu, “Structural and optical properties of tunable warm-white light-emitting zro 2: dy³⁺–eu³⁺ nanocrystals,” *Journal of the American Ceramic Society*, vol. 96, no. 5, pp. 1602–1609, 2013.
- [54] T. Yamaguchi, “Application of zro2 as a catalyst and a catalyst support,” *Catalysis today*, vol. 20, no. 2, pp. 199–217, 1994.
- [55] C. Howard, R. Hill, and B. Reichert, “Structures of zro2 polymorphs at room temperature by high-resolution neutron powder diffraction,” *Acta Crystallographica Section B: Structural Science*, vol. 44, no. 2, pp. 116–120, 1988.
- [56] G. Teufer, “The crystal structure of tetragonal zro2,” *Acta Crystallographica*, vol. 15, no. 11, pp. 1187–1187, 1962.
- [57] J. GKatz, “X-ray diffraction powder pattern of metastable cubic zro_2,” *Am. Ceram. Soc.*, vol. 54, p. 531, 1971.

- [58] O. Ohtaka, T. Yamanaka, S. Kume, N. Hara, H. Asano, and F. Izumi, "Structural analysis of orthorhombic zro2 by high resolution neutron powder diffraction," *Proceedings of the Japan Academy, Series B*, vol. 66, no. 10, pp. 193–196, 1990.
- [59] J. Haines, J. M. Léger, and A. Atouf, "Crystal structure and equation of state of cotunnite-type zirconia," *Journal of the American Ceramic Society*, vol. 78, no. 2, pp. 445–448, 1995.
- [60] M. Batzill and U. Diebold, "The surface and materials science of tin oxide," *Progress in surface science*, vol. 79, no. 2-4, pp. 47–154, 2005.
- [61] Z. Zhang, X. Zou, L. Xu, *et al.*, "Hydrogen gas sensor based on metal oxide nanoparticles decorated graphene transistor," *Nanoscale*, vol. 7, no. 22, pp. 10 078–10 084, 2015.
- [62] S. Wang, J. Huang, Y. Zhao, *et al.*, "Preparation, characterization and catalytic behavior of sno2 supported au catalysts for low-temperature co oxidation," *Journal of Molecular Catalysis A: Chemical*, vol. 259, no. 1-2, pp. 245–252, 2006.
- [63] P. Rajaram, Y. Goswami, S. Rajagopalan, and V. Gupta, "Optical and structural properties of sno2 films grown by a low-cost cvd technique," *Materials Letters*, vol. 54, no. 2-3, pp. 158–163, 2002.
- [64] J. Haines and J. Léger, "X-ray diffraction study of the phase transitions and structural evolution of tin dioxide at high pressure: ffrelationships between structure types and implications for other rutile-type dioxides," *Physical Review B*, vol. 55, no. 17, p. 11 144, 1997.
- [65] L. Gracia, A. Beltrán, and J. Andrés, "Characterization of the high-pressure structures and phase transformations in sno2. a density functional theory study," *The Journal of Physical Chemistry B*, vol. 111, no. 23, pp. 6479–6485, 2007.
- [66] S. Ono, K. Funakoshi, A. Nozawa, and T. Kikegawa, "High-pressure phase transitions in sno2," *Journal of Applied Physics*, vol. 97, no. 7, 2005.
- [67] H. Zhang and J. F. Banfield, "Structural characteristics and mechanical and thermodynamic properties of nanocrystalline tio2," *Chemical reviews*, vol. 114, no. 19, pp. 9613–9644, 2014.
- [68] A. Auxéméry, G. Philippot, M. R. Suchomel, D. Testemale, and C. Aymonier, "Stabilization of tetragonal zirconia nanocrystallites using an original supercritical-based synthesis route," *Chemistry of Materials*, vol. 32, no. 19, pp. 8169–8181, 2020.
- [69] M. Kløve, G. Philippot, A. Auxéméry, C. Aymonier, and B. B. Iversen, "Stabilizing tetragonal zro 2 nanocrystallites in solvothermal synthesis," *Nanoscale*, 2024.
- [70] R. S. Christensen, M. Kløve, M. Roelsgaard, S. Sommer, and B. B. Iversen, "Unravelling the complex formation mechanism of hfo 2 nanocrystals using in situ pair distribution function analysis," *Nanoscale*, vol. 13, no. 29, pp. 12 711–12 719, 2021.

- [71] A. S. Keiteb, E. Saion, A. Zakaria, N. Soltani, *et al.*, “Structural and optical properties of zirconia nanoparticles by thermal treatment synthesis,” *Journal of nanomaterials*, vol. 2016, 2016.
- [72] W. Piskorz, J. Grybos, F. Zasada, *et al.*, “Periodic dft and atomistic thermodynamic modeling of the surface hydration equilibria and morphology of monoclinic zro₂ nanocrystals,” *The Journal of Physical Chemistry C*, vol. 115, no. 49, pp. 24 274–24 286, 2011.
- [73] W. Piskorz, J. Grybos, F. Zasada, *et al.*, “Periodic dft study of the tetragonal zro₂ nanocrystals: equilibrium morphology modeling and atomistic surface hydration thermodynamics,” *The Journal of Physical Chemistry C*, vol. 116, no. 36, pp. 19 307–19 320, 2012.
- [74] J. F. Banfield and H. Zhang, “Nanoparticles in the environment,” *Reviews in mineralogy and geochemistry*, vol. 44, no. 1, pp. 1–58, 2001.
- [75] I. G. Nielsen, M. Kløve, M. Roelsgaard, A.-C. Dippel, and B. B. Iversen, “In situ x-ray diffraction study of the solvothermal formation mechanism of gallium oxide nanoparticles,” *Nanoscale*, vol. 15, no. 11, pp. 5284–5292, 2023.
- [76] H. Zhang, B. Chen, J. F. Banfield, and G. A. Waychunas, “Atomic structure of nanometer-sized amorphous tio₂,” *Physical Review B*, vol. 78, no. 21, p. 214 106, 2008.
- [77] M. Gateshki, M. Niederberger, A. S. Deshpande, Y. Ren, and V. Petkov, “Atomic-scale structure of nanocrystalline ceo₂–zro₂ oxides by total x-ray diffraction and pair distribution function analysis,” *Journal of Physics: Condensed Matter*, vol. 19, no. 15, p. 156 205, 2007.
- [78] C. R. A. Catlow, *Computer modeling in inorganic crystallography*. Elsevier, 1997.
- [79] C. Ponce, M. Caravaca, and R. Casali, “Ab initio studies of structure, electronic properties, and relative stability of sno₂ nanoparticles as a function of stoichiometry, temperature, and oxygen partial pressure,” *The Journal of Physical Chemistry C*, vol. 119, no. 27, pp. 15 604–15 617, 2015.
- [80] A. R. Puigdollers, F. Illas, and G. Pacchioni, “Structure and properties of zirconia nanoparticles from density functional theory calculations,” *The Journal of Physical Chemistry C*, vol. 120, no. 8, pp. 4392–4402, 2016.
- [81] J. Li and L.-W. Wang, “Band-structure-corrected local density approximation study of semiconductor quantum dots and wires,” *Physical Review B*, vol. 72, no. 12, p. 125 325, 2005.
- [82] H.-X. Deng, S.-S. Li, and J. Li, “Quantum confinement effects and electronic properties of sno₂ quantum wires and dots,” *The Journal of Physical Chemistry C*, vol. 114, no. 11, pp. 4841–4845, 2010.

- [83] R. Grena, O. Masson, L. Portal, *et al.*, “Stabilization effect of surface impurities on the structure of ultrasmall ZnO nanoparticles: an ab-initio study,” *The Journal of Physical Chemistry C*, vol. 119, no. 27, pp. 15 618–15 626, 2015.
- [84] R. Viswanatha, S. Sapra, B. Satpati, P. Satyam, B. Dev, and D. Sarma, “Understanding the quantum size effects in ZnO nanocrystals,” *Journal of Materials Chemistry*, vol. 14, no. 4, pp. 661–668, 2004.
- [85] J. Jortner, “Cluster size effects,” *Zeitschrift für Physik D Atoms, Molecules and Clusters*, vol. 24, pp. 247–275, 1992.
- [86] E. A. Meulenkamp, “Synthesis and growth of ZnO nanoparticles,” *The journal of physical chemistry B*, vol. 102, no. 29, pp. 5566–5572, 1998.
- [87] T. J. Jacobsson and T. Edvinsson, “Absorption and fluorescence spectroscopy of growing ZnO quantum dots: size and band gap correlation and evidence of mobile trap states,” *Inorganic chemistry*, vol. 50, no. 19, pp. 9578–9586, 2011.
- [88] X. Xu, J. Zhuang, and X. Wang, “ SnO_2 quantum dots and quantum wires: controllable synthesis, self-assembled 2d architectures, and gas-sensing properties,” *Journal of the American Chemical Society*, vol. 130, no. 37, pp. 12 527–12 535, 2008.
- [89] C. L. Dos Santos and P. Piquini, “Diameter dependence of mechanical, electronic, and structural properties of InAs and InP nanowires: a first-principles study,” *Physical Review B*, vol. 81, no. 7, p. 075 408, 2010.
- [90] M. Born, “Born-oppenheimer approximation,” *Ann. Phys*, vol. 84, pp. 457–484, 1927.
- [91] P. Hohenberg and W. Kohn, “Inhomogeneous electron gas,” *Physical review*, vol. 136, no. 3B, B864, 1964.
- [92] L. H. Thomas, “The calculation of atomic fields,” in *Mathematical proceedings of the Cambridge philosophical society*, Cambridge University Press, vol. 23, 1927, pp. 542–548.
- [93] E. Fermi, “Statistical method to determine some properties of atoms,” *Rend. Accad. Naz. Lincei*, vol. 6, no. 602-607, p. 5, 1927.
- [94] R. P. Feynman, “Forces in molecules,” *Physical review*, vol. 56, no. 4, p. 340, 1939.
- [95] A. Becke, “Completely numerical calculations on diatomic molecules in the local-density approximation,” *Physical Review A*, vol. 33, no. 4, p. 2786, 1986.
- [96] A. D. Becke, “Density functional theories in quantum chemistry: beyond the local density approximation,” in ACS Publications, 1989.
- [97] R. O. Jones and O. Gunnarsson, “The density functional formalism, its applications and prospects,” *Reviews of Modern Physics*, vol. 61, no. 3, p. 689, 1989.

- [98] J. P. Perdew, J. Chevary, S. Vosko, *et al.*, “Erratum: atoms, molecules, solids, and surfaces: applications of the generalized gradient approximation for exchange and correlation,” *Physical Review B*, vol. 48, no. 7, p. 4978, 1993.
- [99] T. J. Giese and D. M. York, “Density-functional expansion methods: evaluation of lda, gga, and meta-gga functionals and different integral approximations,” *The Journal of chemical physics*, vol. 133, no. 24, p. 244 107, 2010.
- [100] P. M. Gill, B. G. Johnson, J. A. Pople, and M. J. Frisch, “The performance of the becke—lee—yang—parr (b—lyp) density functional theory with various basis sets,” *Chemical Physics Letters*, vol. 197, no. 4-5, pp. 499–505, 1992.
- [101] P. M. Gill, “A new gradient-corrected exchange functional,” *Molecular Physics*, vol. 89, no. 2, pp. 433–445, 1996.
- [102] K. Burke, J. P. Perdew, and Y. Wang, “Derivation of a generalized gradient approximation: the pw91 density functional,” in *Electronic Density Functional Theory: recent progress and new directions*, Springer, 1998, pp. 81–111.
- [103] J. P. Perdew, K. Burke, and M. Ernzerhof, “Generalized gradient approximation made simple,” *Physical review letters*, vol. 77, no. 18, p. 3865, 1996.
- [104] A. Janotti and C. G. Van de Walle, “Lda+ u and hybrid functional calculations for defects in zno, sno2, and tio2,” *physica status solidi (b)*, vol. 248, no. 4, pp. 799–804, 2011.
- [105] A. D. Beeke, “Density-functional thermochemistry. iii. the role of exact exchange,” *J. Chem. Phys.*, vol. 98, no. 7, pp. 5648–6, 1993.
- [106] C. Lee, W. Yang, and R. G. Parr, “Effective homogeneity of the exchange-correlation energy functional,” *Phys. Rev. B*, vol. 37, p. 785, 1998.
- [107] J. Heyd, G. E. Scuseria, and M. Ernzerhof, “Hybrid functionals based on a screened coulomb potential,” *The Journal of chemical physics*, vol. 118, no. 18, pp. 8207–8215, 2003.
- [108] J. P. Perdew, M. Ernzerhof, and K. Burke, “Rationale for mixing exact exchange with density functional approximations,” *The Journal of chemical physics*, vol. 105, no. 22, pp. 9982–9985, 1996.
- [109] C. Adamo and V. Barone, “Toward reliable density functional methods without adjustable parameters: the pbe0 model,” *The Journal of chemical physics*, vol. 110, no. 13, pp. 6158–6170, 1999.
- [110] *Pseudopotential*, May 11, 2023. [Online]. Available: <https://en.wikipedia.org/wiki/Pseudopotential>.
- [111] S. Nosé, “A unified formulation of the constant temperature molecular dynamics methods,” *The Journal of chemical physics*, vol. 81, no. 1, pp. 511–519, 1984.

- [112] S. Nosé, “A molecular dynamics method for simulations in the canonical ensemble,” *Molecular physics*, vol. 52, no. 2, pp. 255–268, 1984.
- [113] W. G. Hoover, “Canonical dynamics: equilibrium phase-space distributions,” *Physical review A*, vol. 31, no. 3, p. 1695, 1985.
- [114] V. Rühle, “Berendsen and nose-hoover thermostats,” *Am. J. Phys*, vol. 575, 2007.
- [115] N. Ashcroft and N. Mermin, “Solid state physics (saunders college, philadelphia),” *Google Scholar*, vol. 404, 1976.
- [116] J. H. Davies, *The physics of low-dimensional semiconductors: an introduction*. Cambridge university press, 1998.
- [117] T. D. Kühne, M. Iannuzzi, M. Del Ben, *et al.*, “Cp2k: an electronic structure and molecular dynamics software package-quickstep: efficient and accurate electronic structure calculations,” *The Journal of Chemical Physics*, vol. 152, no. 19, p. 194 103, 2020.
- [118] J. VandeVondele, M. Krack, F. Mohamed, M. Parrinello, T. Chassaing, and J. Hutter, “Quickstep: fast and accurate density functional calculations using a mixed gaussian and plane waves approach,” *Computer Physics Communications*, vol. 167, no. 2, pp. 103–128, 2005.
- [119] J. VandeVondele and J. Hutter, “An efficient orbital transformation method for electronic structure calculations,” *The Journal of chemical physics*, vol. 118, no. 10, pp. 4365–4369, 2003.
- [120] I. Bethune, “Improving the scalability of cp2k on multi-core systems,” Tech. Rep., 2010.
- [121] W. Kohn and L. J. Sham, “Self-consistent equations including exchange and correlation effects,” *Physical review*, vol. 140, no. 4A, A1133, 1965.
- [122] Y. Wang and J. P. Perdew, “Correlation hole of the spin-polarized electron gas, with exact small-wave-vector and high-density scaling,” *Physical Review B*, vol. 44, no. 24, p. 13 298, 1991.
- [123] S. Goedecker, M. Teter, and J. Hutter, “Separable dual-space gaussian pseudopotentials,” *Phys. Rev. B*, vol. 54, pp. 1703–1710, 3 Jul. 1996. [Online]. Available: <https://link.aps.org/doi/10.1103/PhysRevB.54.1703>.
- [124] M. F. Peintinger, D. V. Oliveira, and T. Bredow, “Consistent gaussian basis sets of triple-zeta valence with polarization quality for solid-state calculations,” *Journal of Computational Chemistry*, vol. 34, no. 6, pp. 451–459, 2013.
- [125] D. J. Evans and B. L. Holian, “The nose–hoover thermostat,” *The Journal of chemical physics*, vol. 83, no. 8, pp. 4069–4074, 1985.
- [126] O. Masson and P. Thomas, “Exact and explicit expression of the atomic pair distribution function as obtained from x-ray total scattering experiments,” *Journal of Applied Crystallography*, vol. 46, no. 2, pp. 461–465, 2013.

- [127] N. Igawa, Y. Ishii, T. Nagasaki, Y. Morii, S. Funahashi, and H. Ohno, “Crystal structure of metastable tetragonal zirconia by neutron powder diffraction study,” *Journal of the American Ceramic Society*, vol. 76, no. 10, pp. 2673–2676, 1993.
- [128] C. Howard and R. Hill, “The polymorphs of zirconia: phase abundance and crystal structure by rietveld analysis of neutron and x-ray diffraction data,” *Journal of materials science*, vol. 26, pp. 127–134, 1991.
- [129] S. Le Roux and P. Jund, “Ring statistics analysis of topological networks: new approach and application to amorphous ges_2 and σιο_2 systems,” *Computational Materials Science*, vol. 49, no. 1, pp. 70–83, 2010.
- [130] S. L. Roux and P. Jund, “Erratum: ring statistics analysis of topological networks: new approach and application to amorphous ges_2 and σιο_2 systems. [comput. mater. sci. 49 (2010) 70–83],” *Computational Materials Science*, vol. 50, no. 3, p. 1217, 2011. [Online]. Available: <https://www.sciencedirect.com/science/article/pii/S0927025610005719>.
- [131] H.-W. Wang, D. J. Wesolowski, T. E. Proffen, *et al.*, “Structure and stability of sno_2 nanocrystals and surface-bound water species,” *Journal of the American Chemical Society*, vol. 135, no. 18, pp. 6885–6895, 2013.
- [132] R. French, S. Glass, F. Ohuchi, Y.-N. Xu, and W. Ching, “Experimental and theoretical determination of the electronic structure and optical properties of three phases of zro_2 ,” *Physical Review B*, vol. 49, no. 8, p. 5133, 1994.
- [133] S. Sayan, R. A. Bartynski, X. Zhao, *et al.*, “Valence and conduction band offsets of a $\text{zro}_2/\text{σιο}_x\text{ny}/\text{n-si}$ cmos gate stack: a combined photoemission and inverse photoemission study,” *physica status solidi (b)*, vol. 241, no. 10, pp. 2246–2252, 2004.
- [134] C. Morant, A. Fernandez, A. Gonzalez-Elipse, *et al.*, “Electronic structure of stoichiometric and ar^+ -bombarded zro_2 determined by resonant photoemission,” *Physical Review B*, vol. 52, no. 16, p. 11 711, 1995.
- [135] A. Emeline, G. V. Kataeva, A. S. Litke, A. V. Rudakova, V. K. Ryabchuk, and N. Serpone, “Spectroscopic and photoluminescence studies of a wide band gap insulating material: powdered and colloidal zro_2 sols,” *Langmuir*, vol. 14, no. 18, pp. 5011–5022, 1998.
- [136] C.-K. Kwok and C. R. Aita, “Near-band gap optical behavior of sputter deposited α - and $\alpha + \beta$ - zro_2 films,” *Journal of applied physics*, vol. 66, no. 6, pp. 2756–2758, 1989.
- [137] W. Zhou, Y. Liu, Y. Yang, and P. Wu, “Band gap engineering of sno_2 by epitaxial strain: experimental and theoretical investigations,” *The Journal of Physical Chemistry C*, vol. 118, no. 12, pp. 6448–6453, 2014.

List of Works

ÉTUDE AB-INITIO DES PROPRIÉTÉS STRUCTURALES ET ÉLECTRONIQUES DE NANOPARTICULES DE ZIRCON ET DE DIOXYDE D'ÉTAIN

Résumé: L'objectif principal de cette thèse est d'améliorer notre compréhension de la relation structure-propriétés des nanoparticules de zircon et de dioxyde d'étain, en se concentrant sur les modifications structurales induites par la faible taille des nanoparticules et leurs effets sur les propriétés, en particulier les propriétés électroniques. Cette étude est abordée principalement du point de vue de la simulation numérique ab initio. Afin de réaliser cette étude, nous avons construit plusieurs modèles de nanoclusters de ZrO_2 avec une taille allant de 0,9 nm à 2,0 nm. Pour passer les liaisons pendantes, des molécules d'eau ont été placées près des atomes de zirconium à la surface des nanoclusters. Des simulations de dynamique moléculaire ab initio (AIMD) ont donc été réalisées pour étudier les propriétés structurales et électroniques des nanoclusters. Nous avons ainsi obtenu des modèles structuraux pertinents en bon accord avec les données issues de la caractérisation structurale. Il est à noter que ces modèles présentent une structure atypique avec des différences notables entre la région du cœur et la surface du nanocluster. Les calculs de la structure électronique basés sur la théorie de la fonctionnelle de la densité (DFT) ont montré que la différence entre la valeur du gap électronique calculée pour le système périodique et celle des nanoclusters de ZrO_2 , augmente à mesure que la taille des nanoclusters diminue, ce qui obéit à la loi du confinement quantique. Dans le cas du système SnO_2 , nous avons construit une série de modèles de nanoclusters avec des tailles allant de 0,98 nm à 1,94 nm. Nous avons appliqué le même type d'approche utilisé pour les nanoclusters de ZrO_2 , pour examiner les propriétés structurales et électroniques des nanoparticules de SnO_2 . De la même manière, les propriétés structurales des nanoclusters obtenues sont en bon accord avec les données expérimentales. Un comportement similaire, montrant l'effet du confinement quantique sur la largeur de la bande interdite des nanoclusters de SnO_2 , a également été mis en évidence. Enfin, nous avons réalisé une étude comparative entre les résultats obtenus pour les deux nanoparticules d'oxydes métalliques, en mettant l'accent sur leurs propriétés électroniques.

Mots clés : oxyde de zircon et d'étain(IV), nanoparticules, ab initio, théorie de la fonctionnelle de la densité, dynamique moléculaire, fonction de distribution des paires, structure, propriétés électroniques, effet de confinement quantique, bande interdite, densité d'état

AB-INITIO STUDY OF THE STRUCTURAL AND ELECTRONIC PROPERTIES OF ZIRCONIA AND TIN(IV) OXIDE NANOPARTICLES

Abstract: The primary objective of this thesis research is to improve our understanding of the structure-properties relationships of zirconia and tin(IV) oxide nanoparticles by focusing on the structural modifications induced by the small size of the nanoparticles and their effects on properties, in particular electronic properties. This study is mainly based on the use of first principles numerical simulations methods. To this end, we have built several ZrO_2 nanocluster models with sizes ranging from 0.9 nm to 2.04 nm. To passivate the dangling bonds, water molecules were placed on top of Zr atoms at nanocluster surfaces. Subsequently, ab initio molecular dynamics (AIMD) simulations were performed to investigate the structural and electronic properties of nanoclusters. We have found that, our models are in good agreement with the experimental characterization, which grant them a high level of validity. In addition, these models have an atypical structure with remarkable differences between the nanocluster core and surface. Electronic structure calculations based on density functional theory have shown that the band gap difference between ZrO_2 bulk and nanoclusters increases as the size of nanoclusters decreases obeying the quantum confinement law. Focusing on SnO_2 , we have built a range of nanocluster models with sizes ranging from 0.98 nm to 1.94 nm. Using the same approach employed in the case of ZrO_2 nanoclusters, we have examined the structural and electronic properties of SnO_2 nanoparticles. In the same way, the structures of the obtained nanoclusters are in good agreement with experimental data. A similar behavior, showing the quantum confinement effect on the band gap of SnO_2 nanoclusters, has also been observed. Finally, we carried out a comparative study between the obtained results for both metal oxide nanoparticles, with a specific focus on their electronic properties.

Keywords: zirconia and tin (IV) oxide, nanoparticles, ab initio, density functional theory, molecular dynamics, pair distribution function, structure, electronic properties, quantum confinement effect, band gap, density of state